Non-equilibrium dynamics and quantum computing

From Floquet topological qubits to quantum state preparation

Inaugural-Dissertation
zur
Erlangung des Doktorgrades
der Mathematisch-Naturwissenschaftlichen Fakultät
der Universität zu Köln

vorgelegt von

Anne Maria Irene MATTHIES

aus

Soltau

Berichterstatter:	Prof. Dr. Achim Rosch
	Prof. Dr. Simon Trebst
Tag der mündlichen Prüfung:	16.06.2023

Die vorliegende Dissertation wurde von der Mathematisch-Naturwissenschaftlichen Fakultät der Universität zu Köln angenommen.

Abstract

Quantum computing and non-equilibrium dynamics are two very rapidly developing and entangled fields. With the constant application of gates and measurements, quantum computers are always out of equilibrium. Furthermore, the current noisy quantum chips are prone to errors and dissipation, and are effectively described as an open system. At the same time, the simulation of the long-time dynamics of quantum systems is one of the most promising applications of a quantum computer.

This thesis spans a range of topics, from qubit design to quantum algorithms. The key feature of our proposed qubit is imprinted by non-equilibrium dynamics. Namely, we address how to enhance the basic building block of a Majorana-based quantum computer by periodic driving. The so-called Floquet Majorana box qubits can host not only Majorana zero modes with quasi-energy zero but also Floquet Majoranas with an energy $\hbar\omega/2$, where ω is the driving frequency. This allows us to encode three topological logical qubits in one box. However, a standard adiabatic state preparation protocol fails, and we argue that this instability is a generic and fundamental feature of a Floquet superconductor. Instead, we show that it can be successfully operated using a frequency-sweep protocol, even in the presence of interactions.

On the topic of quantum algorithms, we propose a scalable and robust protocol that prepares low-energy states of arbitrary gapped Hamiltonians, without prior knowledge about the target state. By using a fraction of the qubits to mimic a low-entropy bath, the protocol effectively cools the system to its low-energy state. The cyclic operation of the protocol is a key advantage since it leads to a robust *"coolability"* in the presence of noise. We investigate the performance of the protocol for systems with trivial and topological excitations. Because topological excitations are notoriously difficult to remove, the coolability can help to detect topological order.

Finally, we discuss how this cooling protocol can be implemented on a gate-based quantum computer. While we experimentally tested the protocol on only very few qubits, the promising results suggest that the cooling protocol will be valuable for the preparation of more complex many-body states on future quantum computers.

Kurz und einfach

Für Freunde, Familie und alle Wissenschaftsbegeisterte

Quantencomputer und Nichtgleichgewichtsdynamik sind zwei sich sehr schnell entwickelnde und miteinander "verschränkte" Bereiche. Ein Quantencomputer ist ein Rechner, der anstatt mit Bits, also Nullen und Einsen, mit Quantenbits (Qubits) rechnet. Ein Qubit kann durch die Nutzung quantenmechanischer Eigenschaften auch gleichzeitig Null und Eins kodieren, weshalb von einem verschränkten Zustand gesprochen wird.

Um mit dem Quantencomputer zu rechnen, werden Qubit-Operationen und Messungen durchgeführt, was ein sehr dynamischer Prozess ist. Darüber hinaus passieren auf den derzeit verfügbaren Quantenchips häufig Fehler, wodurch Informationen verloren gehen. Dennoch ist die Simulation der Langzeitdynamik von Quantensystemen eine der vielversprechendsten Anwendungen eines Quantencomputers.

Diese Arbeit spannt den Bogen vom Design eines Qubits bis hin zu einem Quantenalgorithmus. Das Hauptmerkmal des von uns vorgeschlagenen Qubits ist, dass es sich periodisch mit der Zeit verhält. Durch die Periodizität wird ein Nichtgleichgewicht erreicht, in dem zwei verschiedene Arten von Quantenzuständen gut vor Fehlern geschützt werden. Im Gleichgewicht erhält man dagegen nur eine Art geschützten Quantenzustand. Es ist allerdings sehr wichtig, wie das „Nichtgleichgewicht“ eingeschaltet wird. Ein Standardprotokoll funktioniert nicht, aber mit unserem neuen Protokoll können wir stabile Zustände herstellen.

Außerdem haben wir einen Quantenalgorithmus entwickelt, der den Zustand mit der niedrigsten Energie eines beliebigen Quantensystem herstellt. Viele Eigenschaften des Systems hängen von diesem sogenannten Grundzustand ab, weshalb er sehr interessant für die Bereiche Chemie und Materialwissenschaften ist. Gleichzeitig ist es sehr schwierig, den Zustand zu berechnen oder den Zustand herzustellen, wenn er unbekannt ist. In unserem Protokoll nutzen wir einen Teil der Qubits als eine Art Kühlschrank. Dieser "programmierte Kühlschrank" nimmt die überschüssige Energie des Systems auf, wodurch ein Systemzustand mit niedrigerer Energie erreicht wird. Ein Vorteil des Protokolls liegt in der Wiederholung dieses Kühlprozesses, weil es robuster gegen Fehler ist. Somit ist der Algorithmus auch für derzeitig verfügbare Quantencomputer relevant.

Am Ende diskutieren wir, wie dieses Kühlungsprotokoll ganz praktisch in Quantencomputern implementiert werden kann. Da kleine Quantumchips, wie z.B. von

IBM, öffentlich über eine Cloud zugänglich sind, konnten wir das Protokoll experimentell an sehr wenigen Qubits testen. Die Ergebnisse sind vielversprechend und deuten darauf hin, dass das Kühlprotokoll für die Herstellung komplexerer Vielteilchenzustände auf zukünftigen Quantencomputern sehr nützlich sein wird.

Contents

List of Figures

Chapter 1

Quantum Computing Out of Equilibrium

Non-equilibrium dynamics open the door to a fascinating and broad range of phenomena – from the fundamental question *What is Life?*, already addressed by Erwin Schrödinger in 1944 [1], to active matter, many-body thermalization, and new states of matter [2, 3]. Recent experimental progress has brought us ever closer to exploring these phenomena on the quantum level, with analog quantum simulators and quantum computers allowing for the simulation and controlled manipulation of quantum systems [3–7]. While current noisy intermediate-scale quantum (NISQ) devices provide only a few tens to a few hundred qubits and are challenged by noise, they already give a glimpse of what is possible [5]. Furthermore, leveraging these platforms might provide valuable insight into the investigation of non-equilibrium dynamics, since classical computers reach their limitations to predict the long-time behavior of dynamical systems [5, 8].

Two exciting areas at the forefront of this field are the topics of Floquet dynamics and quantum state preparation with the aid of controlled dissipation. Floquet systems are periodically driven systems that are, thus, described by a time-periodic Hamiltonian $H(t+T) = H(T)$. The periodic drive breaks the continuous time translation symmetry while preserving the discrete symmetry, which can lead to exotic long-lived steady states without any equilibrium counterpart [9–11]. On the other hand, the addition of dissipation leads to an open system, in contrast to a closed system which is isolated and whose full unitary dynamics are known. Any system coupled to the environment is an open system. This description is unavoidable if we wish to neglect, or do not know, the evolution of the environment itself.

A large part of the excitement in these topics is highly driven by experimental achievements. It is now possible to control unitary dynamics in different setups. For example, in analog quantum simulators, one can implement adiabatic and Floquet drives using electromagnetic fields, and in a digital quantum computer with either one- or two-qubit gates. Furthermore, one can engineer dissipation by designing the interactions and couplings to the environment [12, 13]. Measurements and outcome-dependent feedback yield a further tuning knob, not available in traditional solid-state experiments.

Beautiful examples of the new opportunities offered by the quantum computing platforms are the preparation and observation of topologically-ordered and time-crystalline phases [6, 14–16]. In general, the simulation of quantum many-body systems is one of the most promising applications of quantum computers. For example, ground state preparation has the potential to impact quantum chemistry and materials science enormously. New proposals utilize engineered dissipation to prepare ground states by digital cooling simulation, which this thesis investigates. As a last example, the 240-year-old Floquet theory [17] shines in new splendor since the discovery of new topological phases without static counterparts [11]. These phases can bring with them long-lived Floquet topological modes that can be utilized for quantum memory, as this thesis explores.

After reviewing some of the exciting advances in the field, we want to discuss the ingredients of a quantum computer. A quantum computer needs a good representation of quantum information and the possibility of universal unitary evolution, state preparation, and measurements [18]. In analogy to the representation of classical information in bits, quantum information can be stored in quantum bits (qubits). Qubits describe quantum mechanical two-level systems that allow the preparation of two states $|0\rangle$ and $|1\rangle$ and their superposition $\alpha |0\rangle + \beta |1\rangle$. A good qubit must have a long coherence time so that many quantum operations can be performed without the loss of quantum information. Furthermore, this small hardware unit must be scalable. One of the most advanced qubit platforms is the superconducting chip with current chip sizes of tens to a few hundred qubits. However, current quantum chips' coherence times are insufficient to outperform classical computers and tackle complex tasks beyond specific problems like in the "quantum supremacy" experiment [5, 19].

Quantum algorithms with more general applications and proven speed-up usually require fault-tolerant quantum computing. Fault tolerance requires excellent quantum memory and quantum operations or error correction. Error correction codes encode the quantum information in logical qubits that consists of multiple physical qubits [20]. A promising route to quantum error correction is to design logical qubits that are topologically protected [21]. However, the large number of physical qubits required for this *"topological quantum software"* is currently unreachable.

Another route is to build topological quantum hardware instead of software.

Topological quantum computing promises better-protected qubits. Here, the quantum information is stored non-locally using quasi-particles with exotic braiding statistics [21, 22]. In Chap. 4, we investigate how to implement a versatile topological qubit platform by Floquet driving. This *"Floquet Majorana box qubit"* can host three topological qubits and allows single- and two-qubit operations using a single device. Furthermore, we discuss the stability of such a qubit that shows generic features of Floquet states in superconductors. For background information, we recommend the reader the introduction to Floquet theory Sec. 3.1 and topology in (Sec. 2.2) and out (Sec. 3.2) of equilibrium.

In the absence of topological software or hardware, one can nevertheless take advantage of the current generation of noisy devices. In Chap. 5, we investigate a *noise-resilient* quantum algorithm inspired by adiabatic demagnetization. This condensed-matter technique cools samples to very low temperatures in experiments. Programmed on a quantum computer, this cyclic protocol partially self-corrects errors and, thus, can provide noise resilience. The algorithm aims to prepare ground states of gapped quantum many-body Hamiltonians using engineered dissipation and simulated cooling. We investigate the cooling protocol in the presence of noise for systems with local and topological (non-local) excitations. The self-correcting property of the proposed algorithm makes it feasible for implementation on current devices. In Chap. 6, we outline how this protocol can be implemented on a gate-based noisy quantum computer. The promising results indeed show a cooling effect. Sec. 2.3 covers the basics of quantum state preparation. We also recommend Sec. 3.4 for an introduction to open quantum systems.

This thesis has three common themes: Quantum computing, non-equilibrium dynamics, and topology. In Chap. 1, we explore the field of quantum computing from quantum hardware, particularly the design of qubits, to quantum software focusing on state preparation. Investigating the Floquet topological qubit and the cooling algorithm requires a non-equilibrium description. Therefore, the basics of Floquet theory and open quantum systems are discussed in Chap. 3. Finally, we discuss the role of topology in the context of quantum computing and non-equilibrium dynamics. On the one hand, topology protects the quantum information encoded in the Floquet Majorana box qubit, see Chap. 4. On the other hand, we find that topological excitations are much harder to eliminate using our cooling protocol than trivial excitations, see Chap.5.

Chapter 2

Quantum Computation

"I think there is a world market for maybe five computers. " — Thomas Watson, chairman of IBM, 1943

Quantum computing is one of the most promising, unpredictable, and challenging technologies of our time. It is promising because calculations can be run more efficiently on a quantum computer than on a classical computer by leveraging the effects of quantum mechanics [23–25]. An exponential speedup, but even a sub-exponential speedup could revolutionize the fields of security, material science, and more. A *prime* example is the most efficient prime factorization with Shor's algorithm [26] which has already been experimentally executed for very small qubit numbers on different quantum computing platforms [27–30]. However, for most classically unsolvable (meaning not in polynomial time) problems, a problem-solving strategy on a quantum computer is not yet known. Most-likely quantum computing will be only useful in very specific cases, where cryptography, optimization, and Hamiltonian simulation are the most prominent [8, 31, 32].

Suppose one compares the evolution, over eight decades, from living-room sized classical computers to more powerful and smaller smartphones with the development of potential future quantum computers. In that case, quantum technology is still in its baby shoes. Even though the current quantum devices are already a giant playground for physicists, they lack the quality and quantity to outplay the classical computer [32].

A quantum processor contains a collection of two-level systems called quantum bits (qubits), which, compared to their classical counterpart, cannot only be in state $|0\rangle$ or $|1\rangle$, but also in a superposition of the two $\alpha |0\rangle + \beta |1\rangle$. However, there are also proposals to take more levels into account. One of the most advanced experimental platforms are currently trapped ions, cold atoms, and superconducting qubits. Ions and atoms can intrinsically form qubits at low enough temperatures. Their quantum nature gives rise to well defined energy levels. Within this, it can be possible to isolate a two level system, well separated from the other energy levels, that then defines the $|0\rangle$ state and the $|1\rangle$ state. Furthermore, the excitation energies to transition to other excited states should be distinct, to avoid cross talk. Ions can be trapped using electromagnetic fields, whereas atoms can be trapped using optical fields. The interactions between the qubits can be controlled using lasers in both cases. Often, these platforms are referred to as quantum simulators since the interaction between particles of the Hamiltonian can be directly implemented. However, it is also possible to implement quantum gates, the *digital* operations of a quantum computer, on the qubits. A quantum gate is an operation on a small number of qubits and the building block for larger quantum circuits that implement a quantum algorithm.

Gate-based quantum computing is very natural for superconducting qubits. A superconducting qubit is a mesoscopic system where the lowest energy levels of an electric circuit form the computational basis states. The central element of this circuit is a Josephson junction. We discuss why such a macroscopic object is a good qubit in the next section. We restrict ourselves to superconducting qubits because they form the basis of the topological qubit investigated in this thesis.

Then, the notion of topological quantum computing is introduced, and with that, one of the potential designs of a topological qubit – the Majorana box qubit. Finally, at the end of this chapter, we turn from the hardware of the quantum computer to potential applications – quantum state preparation.

2.1 Superconducting qubits

Recommended additional literature for this section

1. A. Cottet's Ph.D. thesis on *"Implementation of a quantum bit in a superconducting circuit"* [33],
2. Review on superconducting qubits by M. Devoret, A. Wallraff and J.M. Martinis [34]
3. Introduction to quantum electromagnetic circuits by U. Vool and M. Devoret [35]

It is not apparent why a macroscopic electrical circuit is a good quantum coherent and, thus, a good quantum computing platform. It turns out, however, that superconducting qubits are one of the most advanced qubits. Superconducting qubits have the advantage that they are scalable, reasonably easy to fabricate using lithography techniques, and easy to manipulate using electrical signals through

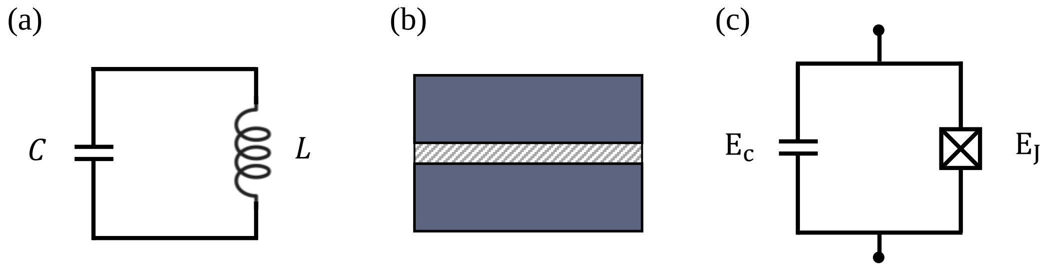

FIGURE 2.1: From an LC circuit to a superconducting qubit: (a) Lumped element circuit for the LC oscillator, an electromagnetic resonator. (b) A thin tunnel barrier separates two superconductors. (c) In parallel with a capacitor, a Josephson tunneling element models a superconducting qubit.

coupled wires. At the same time, quantum chips have already almost reached the maximum number of physical qubits. Furthermore, unlike atoms, superconducting qubits have an extensive size and need to be connected by wires. Especially the connection of wires leads to heating effects and space issues in the refrigerator that holds the quantum chip. [36–38]

A macroscopic system that shows quantum effects is called mesoscopic. Why an electric circuit can be mesoscopic, will be addressed in the following. Let us start with a simple circuit consisting of an inductor and a capacitor with flux Φ and charge Q, respectively. Such a circuit can be described as a harmonic oscillator where Φ and Q are conjugate variables and are analogue to the position and momentum of mass in a mechanical harmonic oscillator. There are two conditions for quantum effects to show up. First, the temperature T must be low enough such that thermal fluctuations don't excite the system,

$$k_B T \ll \hbar\omega_0 \,, \tag{2.1}$$

where ω_0 is the harmonic oscillator frequency [35]. Secondly, the broadening of the energy levels must be smaller than their separation. The small broadening of energy levels requires, e.g., low dissipation and damping of the harmonic oscillator [35]. The circuit becomes dissipationless for superconducting wires. Even though measurement devices are a source of dissipation, high enough quality factors can be achieved in a superconducting circuit to observe quantum effects in experiments. However, quantum fluctuations become only visible in the variance or higher moments of the observables for the harmonic oscillator since $\langle p \rangle$ and $\langle x \rangle$ are zero due to the $x \to -x$ and $p \to -p$ symmetry. These higher moments are not so easy to detect in experiments. The simplest circuit element that is non-dissipative and non-linear is the Josephson junction. It is also the building block of the superconducting qubit. The non-linearity helps to observe quantum effects in experiments. For a qubits, it has a more practical advantage. The energy levels are no longer equally spaced. Thus, one can address the transition from the ground state to the first excited state without the risk of occupying higher energy states.

A Josephson junction - two bulk superconductors separated by a thin insulating layer - can be modeled by a Josephson tunneling element and a capacitor in parallel. The Hamiltonian, therefore, consists of two parts. The first term is the electrostatic Hamiltonian

$$\hat{H}_c = E_c \sum_N (\hat{N} - N_g)^2, \tag{2.2}$$

where $\hat{N}$ counts the number of Cooper pairs and $N_g = \frac{C_g V_g}{2e}$ is the offset charge. The charging energy $E_c = (2e)^2/(2C_\Sigma)$ quantifies how much energy is need to transfer a single electron through the Josephson junction. The capacitance C_Σ includes the intrinsic capacitance of the junction C_J. But depending on the design, more capacitors might be added to the circuit. In contrast, the Josephson Hamiltonian describes Cooper pair tunneling between the two bulk superconductors through the junctions. We can write down a hopping Hamiltonian for the Cooper pairs

$$\hat{H}_J = -\frac{E_J}{2} \left(\sum_N |N\rangle \langle N+1| + |N+1\rangle \langle N| \right), \tag{2.3}$$

where the energy E_J is needed for a Cooper pair to tunnel through the junction. The total Hamiltonian then reads

$$H_{SC} = E_c \sum_N (\hat{N} - N_g)^2 - \frac{E_J}{2} \left(\sum_N |N\rangle \langle N+1| + |N+1\rangle \langle N| \right). \tag{2.4}$$

In the following, we will discuss this circuit in two regimes $E_c \ll E_J$ called the transmon limit and $E_J \ll E_c$ called the Cooper pair box limit.

2.1.1 Cooper pair box

The limit $E_J \ll E_c$ for the Cooper pair box is achieved when the Josephson junction is small. The offset charge N_g of Eq. (2.2) can be controlled by an external gate voltage. Since the charging energy governs the Hamiltonian, the eigenstates are the charge eigenstates $|N\rangle$ for most gate voltages; see Fig. 2.2 where the eigenenergies are shown as a function of the offset charge N_g. At the crossing points $N_g \bmod 1 = 1/2$, the degeneracy of $|N\rangle$ and $|N+1\rangle$ states is lifted by E_J acting as

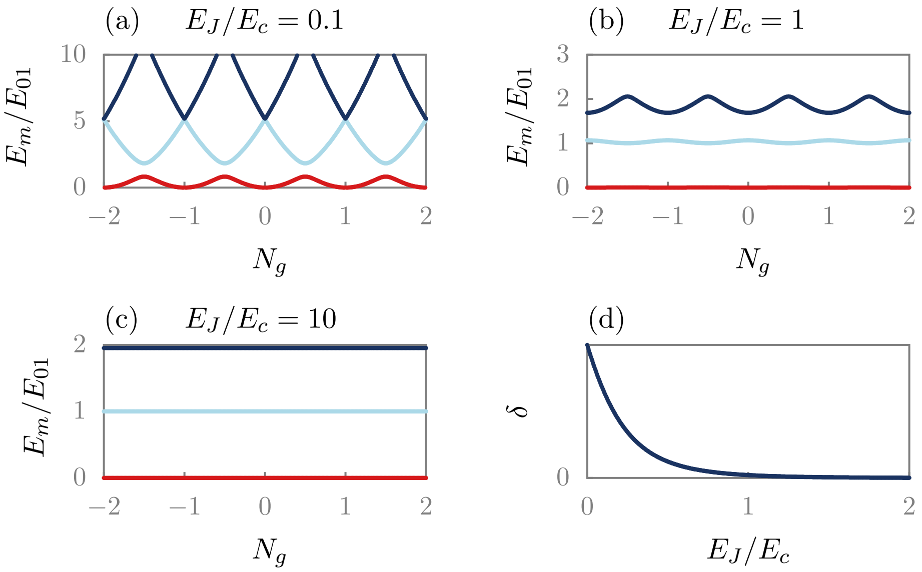

FIGURE 2.2: Energy dispersion of the superconducting qubit: Panel (a)-(c): First three eigenenergies as a function of the effective offset charge N_g for different ratios $E_J/E_c = 0.1$. The energies are normalized by the energy gap $E_{01} = E_1 - E_0$ evaluated at the point $N_g = 1/2$. All energies are shifted such that the minimum of the lowest energy level is at zero. (d) The charge dispersion $\delta = E_0(N_g = 1/2) - E_0(N_g = 0)$ decreases exponentially as a function of the ratio E_J/E_c.

an effective Zeeman energy. As shown in Fig. 2.2, the eigenenergies and therefore also transition frequencies are very sensitive to the gate voltage and thus charge noise. The Cooper pair box is the first quantum electric circuit, where a coherent superposition of the states $|0\rangle$ and $|1\rangle$ has been prepared and Rabi oscillations between the two states have been observed [35, 39]. However, this early generation of a superconducting qubit has been replaced by the transmon design to reduce the charge noise, as discussed in the next section.

2.1.2 Transmon qubit

The transmon is a Cooper pair box with an additional large capacitor C_S such that the charging energy $E_c = 2e^2/(C_J + C_S)$ is reduced [40]. The main advantage of the transmon qubit is that it is insensitive to charge noise, as a drift in gate voltage doesn't change the transition frequency. This robustness to charge noise leads to longer coherence times. For further discussion, it is useful to look at the phase representation of the Josephson Hamiltonian Eq. (2.3). The conjugate operator of the number of Cooper pairs is the phase difference between the two bulk superconductors $\hat{\phi} = \hat{\phi}_1 - \hat{\phi}_2$ with $\hat{\phi}\,|\phi\rangle = \phi\,|\phi\rangle$ and $\phi \in [0, 2\pi[$. Therefore,

$$[\hat{N}, \hat{\phi}] = -i \quad \text{and} \quad \hat{N} = -i\partial_\phi. \tag{2.5}$$

The operator $e^{\pm i\phi}|N\rangle = |N \pm 1\rangle$ increases (decreases) the number of Cooper pairs. The Josephson Hamiltonian, Eq.(2.3), reads in the phase representation

$$\hat{H}_J = -E_J \cos(\hat{\phi}). \tag{2.6}$$

In the strong limit $E_J \gg E_c$, the total Hamiltonian can be approximated by a harmonic oscillator

$$H \approx E_c(\hat{N} - N_g)^2 - E_J + \frac{E_J}{2}\hat{\phi}^2. \tag{2.7}$$

This approximation will become useful for investigating the Floquet Majorana box qubit. Note, however, that an anharmonicity of the Josephson element leads to a unique energy spacing, which is desired for a good qubit to avoid crosstalk with higher energy levels. Finally, note that the total Hamiltonian, Eq. (2.4), without any approximations can be exactly solved in the phase representation using Mathieu functions [40].

2.2 Topological quantum computation

Recommended additional literature for this section

1. Online course on topology in condensed matter, particulary the section *Topology in toy models* and *Majoranas I* [41],
2. Book by J. K. Pachos on topological quantum computation [22]
3. Reviews on Majorana condensed matter physics [42–44]
4. For the Jordan-Wigner transformation: G. B. Mbeng, A. Russomanno, and G. E. Santoro [45]

In topological quantum computation, quantum information is stored in exotic particles called anyons [22]. Anyons obey braiding statistics different from fermions or bosons. Exchange statistics in quantum mechanics arises because particles are indistinguishable. In three spatial dimensions, a wave function can acquire either a phase 0 (bosons) or π (fermions) when two particles are exchanged. In two spatial dimensions, however, acquiring more exotic braiding statistics is possible, as in the case for anyons. The quantum evolution of anyons is described by topology and is, therefore, independent of the geometric details. Using anyons makes the topological quantum computer more resilient against errors and perturbations. The notion of anyons is strongly linked to quantum error correction algorithms, where logical qubits are encoded in many physical qubits, and the code

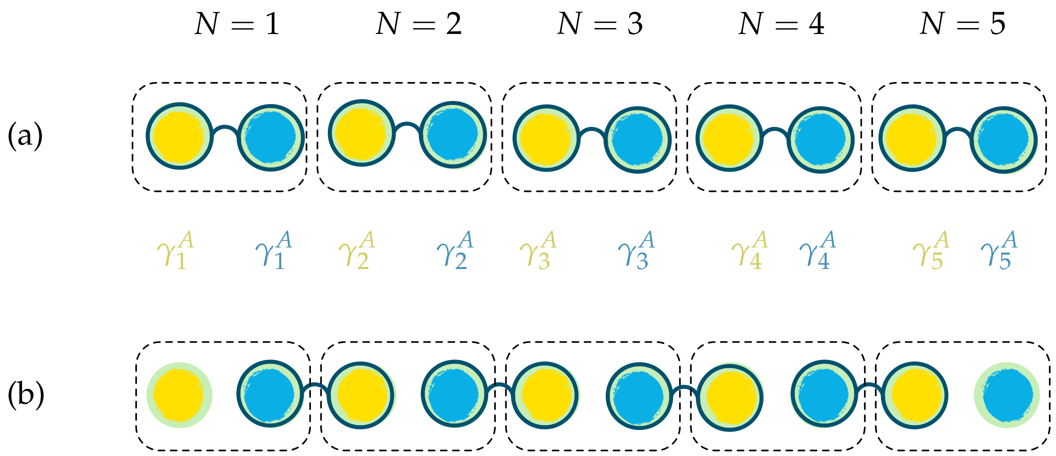

FIGURE 2.3: The two different phases of the Kitaev chain: N fermions (enclosed by the dashed line) split each into two Majorana fermions γ_i^A (yellow) and γ_i^B (blue). (a) Trivial phase: If $\mu > |t|$, the two Majorana operators of the same site couple to each other (encircled by the blue line) and form a fermion that coincides with the original fermion. (b) Topological phase: $\mu < |t|$, γ_i^B and γ_{i+1}^A of different sites couple. The effective fermionic quasi-particles are spread over two neighboring sites. At the boundary, the two Majorana operators γ_1^A and γ_N^B don't have a partner. The effective fermionic mode is localized a the edges and is topologically protected.

takes advantage of the topological protection of the logical qubit, see Sec. 2.3.4. In a sense, topological quantum computers thus have built-in error correction hardware, which makes them more robust than *conventional* quantum computers.

The Majorana box qubit is one of the most promising topological quantum computation platforms [46]. It is also the basis for the Floquet Majorana box qubit discussed in chapter 4. In this section, we review the one-dimensional Kitaev chain and see how topological superconductivity is imprinted there [47]. In the end, we discuss how to build a useful qubit out of topological superconducting quantum wires.

2.2.1 1D Kitaev chain

The simplest model to describe a topological superconducting quantum wire is the one-dimensional Kitaev chain [47]. The model describes N spin-less fermions arranged in a chain at a potential μ, nearest neighbor hopping t, and a superconducting pairing Δ,

$$H_{\text{Kitaev}} = \sum_i -\mu_i c_i^\dagger c_i - \frac{t_i}{2} c_i^\dagger c_{i+1} + \frac{\Delta_i}{2} c_i c_{i+1} + h.c., \tag{2.8}$$

where $c_i^\dagger$ (c_i) are the fermionic creation (annihilation) operators. One can rewrite the Hamiltonian in terms of so-called Majorana operators $\gamma_i^A = c_i + c_i^\dagger$ and $\gamma_i^B = i(c_i^\dagger - c_i)$. These new operators obey the fermionic anti-commutation relation $\{\gamma_i^A, \gamma_j^B\} = 2\delta_{i,j}\delta_{A,B}$. Importantly, the operator property $(\gamma_i^A)^2 = (\gamma_i^A)^2 = 1$ means that they are their own antiparticles. Rewriting the Hamiltonian doesn't change the physics, but for special points, it is easy to distinguish the Hamiltonian's trivial and topological phases. For $\mu = 0$ and $t = \Delta$, the Hamiltonian simplifies to

$$H_{\text{top}} = \Delta \sum_i \gamma_i^B \gamma_{i+1}^A, \tag{2.9}$$

while for $t = \Delta = 0$

$$H_{\text{trivial}} = -\mu \sum_i \gamma_i^A \gamma_i^B. \tag{2.10}$$

In the trivial case, the two Majorana operators of the same site couple with each other and form one local fermionic mode. In the topological case, two Majorana operators of neighboring sites couple with each other, leaving two operators at the end of the chain without a partner. The edge mode doesn't explicitly appear in the Hamiltonian, has zero energy, and makes the ground state degenerate. The existence of the Majorana zero mode is protected by the symmetry of positive and negative energies around zero and the absence of zero modes in the bulk.

It is convenient to write the Kitaev Hamiltonian in the Bogoliubov-de-Gennes form, where it becomes clear that Majorana modes indeed don't depend on fine-tuned parameters. In Bogoliubbov-de Gennes formalism $H = \frac{1}{2}C^\dagger H_{BdG} C$ with $C = (c_1, ..., c_N, c_1^\dagger, ..., c_n^\dagger)$, the Hamiltonian becomes

$$H_{\text{BdG}} = -\sum_n \mu\tau_z \left|n\right\rangle \left\langle n\right| + \sum_n \left[\left(-\frac{t}{2}\tau_z + i\frac{\Delta}{2}\tau_y\right) \left|n\right\rangle \left\langle n+1\right| + h.c. \right], \tag{2.11}$$

where the Pauli matrices τ_i act in the particle-hole space and $|n\rangle$ is the column vector e_n corresponding to the nth site. The Hamiltonian H_{BdG} is a $2N \times 2N$ matrix acting on basis states $|n\rangle |\tau\rangle$ with $\tau = \pm 1$ for electrons and holes, respectively, and can easily be solved numerically. In Fig. 2.4, the energy for $\Delta = t$ as a function of the chemical potential shows a gap for $|\mu| < |t|$. At the same point, the Majorana modes split as well. Similarly, the Majorana modes become less localized with increasing chemical potential but only couple with each other if $\mu > t$, see Fig. 2.4b. One can also verify that the Hamiltonian is particle-hole symmetric $\mathcal{P} H_{BdG} \mathcal{P}^{-1} = -H_{BdG}$ with $\mathcal{P} = \tau_x \mathcal{K}$ and complex conjugation $\mathcal{K}$. Note, however, that the particle-hole symmetry is intrinsic for a BdG Hamiltonian and cannot be lifted.

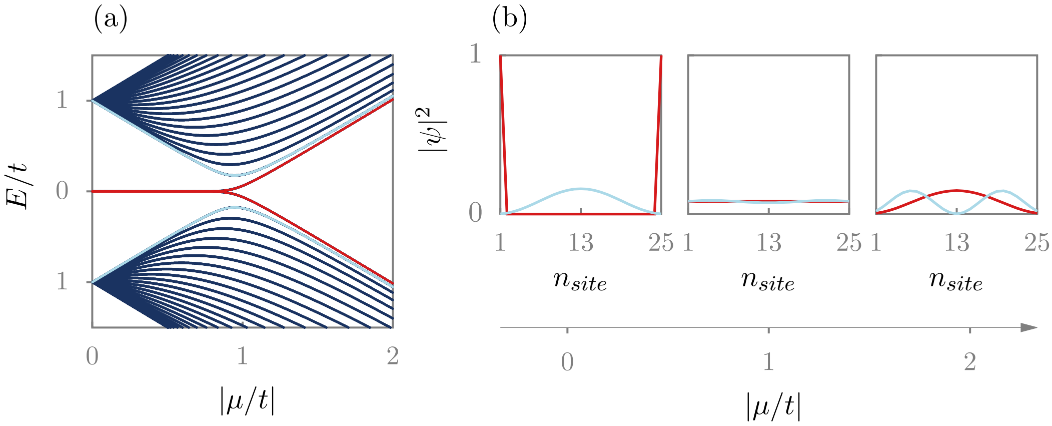

FIGURE 2.4: The spectrum of the Kitaev chain as function of the chemical potential ($N_{site} = 25$, $t = -\Delta = 1$): (a) For $|\mu/t| < 1$, the Majorana zero mode (red) is protected by a bulk gap. The Majorana zero mode vanishes at $|\mu/t| = 1$, and the lowest energy level becomes finite. (b) The wave function of the lowest energy level (red) and the first excited state (light blue): The Majorana zero mode is localized at the edges of the chain. The lowest energy mode becomes completely delocalized at $\mu/|t| = 1$.

The topological nature of the zero-energy edge modes can be further classified by a bulk topological invariant or by the bulk-edge correspondence discussed below. It can also be used as a building block for topological quantum computation.

2.2.2 Bulk edge correspondence

Majorana modes appear because of the bulk-edge correspondence, and as such at the interface of trivial and topological systems. To study the bulk of the system, we can use periodic boundary conditions for the BdG Hamiltonian of Eq. (2.11). Then, the Hamiltonian becomes translationally invariant, and we can apply the Bloch theorem. We use the Fourier transform $|k\rangle$ of $|n\rangle$

$$|k\rangle = \frac{1}{\sqrt{N}} \sum_{n=1}^{N} e^{ikn} |n\rangle \,, \tag{2.12}$$

where the momentum k is conserved and thus a good quantum number. k can take values $2\pi p/N$ with $p = 0, \ldots, N-1$ and eigenstates are 2π periodic. Therefore, it is enough to analyze the Hamiltonian in the Brillouin zone $k \in [-\pi, \pi]$.

The Hamiltonian transforms as

$$\begin{aligned} H_k = \langle k| H_{BdG} |k\rangle &= -\mu\tau_z - \frac{t}{2}(e^{-ik}\tau_z + e^{ik}\tau_z) + \frac{\Delta}{2}(e^{-ik}i\tau_y - e^{ik}i\tau_y) \\ &= -(\mu + t\cos(k))\tau_z + \Delta\sin(k)\tau_y, \end{aligned} \tag{2.13}$$

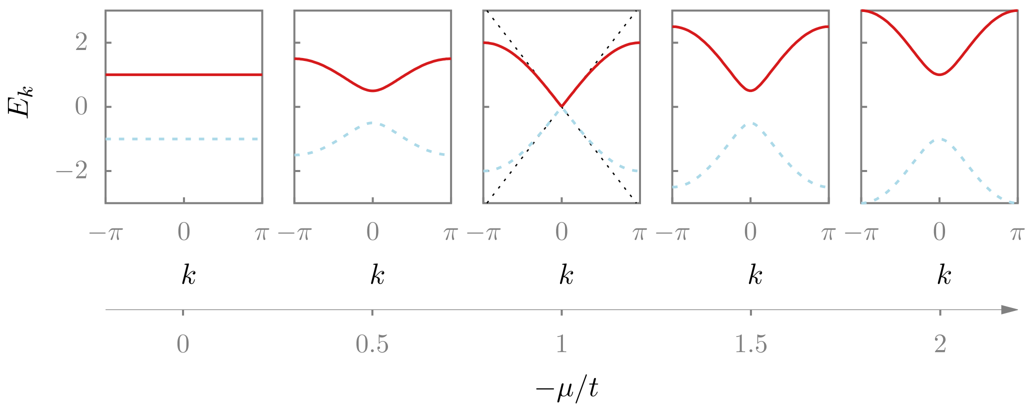

FIGURE 2.5: The bulk spectrum of the Bogoliubov-de Gennes Hamiltonian for different ratios μ/t: The physical excitation energies are positive (red), while "the Bogoliubov shadows" (dashed blue) have negative energies. At the phase transition, the two band touch and show a linear dispersion (dashed black). At this point, the model can be described by an effective Dirac Hamiltonian for small momenta.

where we used that for periodic boundary conditions

$$\sum_n \langle k|n\rangle \langle n+1|k\rangle = \sum_{m,l,n} \frac{1}{N} e^{-ikm} e^{ikl} \langle l|n\rangle \langle n+1|m\rangle = e^{-ik}. \tag{2.14}$$

Thus, the $2N \times 2N$ matrix reduces to a 2×2 problem in momentum space. The eigenenergy can be calculated as

$$E(k) = \pm\sqrt{(\mu + t\cos(k))^2 + \Delta^2 \sin(k)^2}. \tag{2.15}$$

The spectrum is gapped, and the bulk gap closes for $\mu = -t$ at $k = 0$ and $\mu = t$ at $k = \pi$, marking the topological phase transition. For $\mu \approx -t$, we can expand the Hamiltonian up to first order in k around $k = 0$ and arrive at an effective Dirac model

$$H_k \approx -(\mu + t)\tau_z + \Delta k \tau_y \tag{2.16}$$

with an effective mass $m = -(\mu + t)$. Now we can differentiate the trivial phase ($\mu > -t$) from the topological phase ($\mu < -t$) by the sign of the mass. When the bulk gap closes and the mass changes sign, the finite-size system has a phase transition between hosting and not hosting Majorana zero modes.

2.2.3 Mapping to the transverse field Ising model

The Kitaev chain is closely related to the transverse field Ising model by a Jordan-Wigner transformation, a model which we will use extensively in Chap. 5 and

6. The transverse field Ising model was the first to describe quantum magnets and is a versatile test case for many problems in statistical mechanics and non-equilibrium dynamics [48]. The Hamiltonian describes spins in a chain with nearest neighbour $\sigma_x\sigma_x$-interaction $J > 0$ and a transverse field h_z,

$$H_{\text{Ising}} = -J\sum_i \sigma_i^x\sigma_{i+1}^x - h_z\sum_{i=1}^{L}\sigma_i^z\,, \tag{2.17}$$

where the first summation goes from 1 to $L-1(L)$ for open (periodic) boundary conditions. This model shows two different phases. For $J > h_z$, the system is ferromagnetic, while it is paramagnetic for $h_z > J$. In the paramagnetic phase, the model has only trivial local excitations, whereas in the ferromagnetic case, the excitations are topological (non-local) in the form of domain walls. At dual points, $J_1 = a$, $h_{z,1} = b$ and $J_2 = b$, $h_{z,2} = b$, the excitation spectrum looks the same since the high energy excitations of one phase are mapped to the low-energy excitations of the other phase. This property helps to investigate the effect of topological excitation, e.g., on the performance of the cooling protocol discussed in Chap. 5.

The ferromagnetic case maps to the topological phase of the Kitaev chain, which hosts Majorana zero modes. The connections between the two models might not be evident at first sight. In the following, we discuss how the Jordan-Wigner transformation can be applied, following Ref. [45].

Spins are very different from the usual, canonical bosons or fermions as the spin operators commute only at different sites

$$[\sigma_i^\alpha, \sigma_j^\alpha] = 2i\epsilon_{\alpha\beta\gamma}\sigma_j^\gamma\delta_{i,j}\,, \tag{2.18}$$

where the Greek letters denote the different Pauli operators, and the Latin letters the site and there is no summation over i. The raising and lowering operators $\sigma_j^\pm = (\sigma_j^x \pm i\sigma_j^y)/2$, however, obey the fermionic anti-commutation relation $\{\sigma_j^+, \sigma_j^-\}$ at the same site. We can first introduce the so-called hard-core bosonic operators $b_j^\dagger$ and b_j. As usual bosonic operators, the creation operator $b_j^\dagger$ creates a particle from the vacuum $b_j^\dagger\left|0\right\rangle = \left|1\right\rangle$ and the annihilation operator obeys $b_j\left|1\right\rangle = \left|0\right\rangle$. However, we restrict the Hilbert space to two states $\{\left|0\right\rangle, \left|1\right\rangle\}$ such that $b^\dagger\left|1\right\rangle = 0$ mimicking the spin-$\frac{1}{2}$ Hilbert space. We can associate $\left|0\right\rangle = \left|\uparrow\right\rangle$ ($\left|1\right\rangle = \left|\downarrow\right\rangle$) and the hard-core bosonic operators with the raising and lowering spin operators $\sigma_j^{\pm}$ such that

$$\begin{aligned}\sigma_j^+ \left|\downarrow\right\rangle &= \left|\uparrow\right\rangle = \left|0\right\rangle = b_j \left|1\right\rangle,\\ \sigma_j^- \left|\uparrow\right\rangle &= \left|\downarrow\right\rangle = \left|1\right\rangle = b_j^\dagger \left|0\right\rangle,\\ \sigma_j^z &= 1 - 2b_j^\dagger b_j\,.\end{aligned} \tag{2.19}$$

Note that the new bosonic operators commute only at different sites but anticommute at the same site. The hard-core bosons are a good basis for spin-less fermions since the Pauli principle only allows for one spin-less fermion per site. For the one-dimensional chain, it is possible to keep track of the ordering of the fermionic operators and to transform the hard-core bosons into spin-less fermions. In higher spatial dimensions, this transformation is not useful any more as it generically becomes non-local. The Jordan-Wigner transformation maps the hard-core bosons b_j to spin-less fermions

$$b_j = e^{-i\pi\sum_{j'=1}^{j-1} n_{j'}} c_j, \tag{2.20}$$

where the string operator $K = e^{-i\pi\sum_{j'=1}^{j-1} n_{j'}} = \prod_{j'=1}^{j-1}(1-2n_{j'})$ amounts to a sign ±1 and counts the fermion number parity before site j. In the end, we can transform the Pauli operators σ_j^x and σ_j^z as follows

$$\sigma_j^x = K_j(c_j^\dagger + c_j) \quad \text{and} \quad \sigma_j^z = 1 - 2n_j. \tag{2.21}$$

Now we can transform the transverse field Ising chain

$$\begin{aligned} H_{\text{Ising}} &= -J\sum_i \sigma_i^x\sigma_{i+1}^x - h_z\sum_i \sigma_i^z\\ &\leftrightarrow\\ H_{\text{Kitaev}} &= -J\sum_i \left(c_i^\dagger c_{i+1} + c_i^\dagger c_{i+1}^\dagger + h.c.\right) - h_z\sum_i (1-2n_i),\end{aligned} \tag{2.22}$$

where h_z now acts as a chemical potential for the fermions and J accounts for nearest neighbor tunneling and superconducting pairing of the fermions. The phase transition between the paramagnetic and ferromagnetic phase of the transverse field Ising model coincides with the phase transition of the trivial and topological phase of the Kitaev model at $J = h_z$ for open boundary conditions. One has to be careful with transforming the Ising chain under periodic boundary conditions since it doesn't imply periodic boundary conditions for the spinless fermions. The fermionic model has periodic boundary conditions if the fermionic number parity is odd $e^{i\pi N} = -1$ and anti-periodic boundary conditions otherwise. Note also that the local operator σ_x transforms in a very non-local way.

2.2.4 Topological invariants

Similar to the sign of the mass in the effective Dirac system, we want to find a bulk property that is a topological invariant and that can be calculated directly from H_k of Eq. (2.13). In general, one can classify two Hamiltonians H and H' as topological equivalent if H' can be continuously transformed into H. Without any constraints, this task is trivial and always possible. However, for a gapped system, one can ask whether H can be continuously transformed without closing the gap, and this answer is non-trivial. Let us consider non-interacting free fermion Hamiltonians in which the chemical potential lies within a band gap. If two Hamiltonians have the same number of eigenstates below the gap, they then can be transformed continuously as the energy bands below the gap can be freely shifted. By counting the number of eigenstates below the gap, we can define a topological invariant $\mathcal{Q}$, which cannot change without a zero energy crossing

$$\mathcal{Q} = \#\text{ of eigenstates below the gap.} \tag{2.23}$$

Equivalently, one can track the topological invariant by the number of zero-energy crossings. Systems with different $\mathcal{Q}$ are separated by a topological phase transition.

For symmetry-protected topological phases, the topological invariant is connected to the symmetry of the Hamiltonian. For example, the spectrum is doubly degenerate in a spin-$\frac{1}{2}$ system with time-reversal symmetry. The Kramer degeneracy implies that energy levels cross zero energy always in pairs, and the topological invariant $\mathcal{Q}$ can only change in multiples of two.

The Bogoliubov-de-Gennes Hamiltonian (Eq. (2.11)) is particle-hole symmetric. For every eigenstate with energy E, there exists an eigenstate with energy $-E$. Note that only the positive energies are physical. The negative energies only come from the Bogoliubov framework, which we call "Bogoliubov shadows". As the positive and negative energies always come in pairs, the number of eigenstates below and above the gap is always equal. It doesn't change during the topological phase transition, even though the gap closes. Thus, we need to define another topological invariant. Although the Bogoliubov-de-Gennes Hamiltonian does not conserve the particle number, fermion number parity is conserved. The gap closure marks the change in the fermionic number parity.

The tool to quantify the change in fermionic number parity of H_{BdG} is the Pfaffian. A Pfaffian is defined for an anti-symmetric matrix A. For such a matrix eigenvalues come in pairs of $\pm A_n$. The determinant of A is therefore $\det(A) = \prod_n(-A_n^2)$. The Pfaffian is constructed such that it uniquely defines the sign of

$$\sqrt{\det(A)} = \pm \prod_n A_n. \tag{2.24}$$

For example, for a simple skew-symmetric 2×2 matrix $A_{2\times 2}$,

$$A_{2\times 2} = \begin{pmatrix} 0 & a \\ -a & 0 \end{pmatrix}, \tag{2.25}$$

the Pfaffian is $\mathrm{Pf}(A_{2\times 2}) = a$. When the fermion number parity changes, a single E_n reverses its sign or, equivalently, a particle and a hole are interchanged. The sign change is not reflected in the determinant but in the Pfaffian.

To compute the Pfaffian for the bulk of the Kitaev chain, we need to transform H_k (Eq. (2.13)) by a unitary transformation into an anti-symmetric form

$$\tilde{H}(k) = \frac{1}{2}\begin{pmatrix} 1 & 1 \\ i & -i \end{pmatrix} H_k \begin{pmatrix} 1 & -i \\ 1 & i \end{pmatrix}. \tag{2.26}$$

As discussed in Sec. 2.2.2, the gap closure only happens at $k = 0$ and $k = \pi$ and the transformed Hamiltonian simplifies to

$$\tilde{H}(0) = -i\begin{pmatrix} 0 & -t-\mu \\ t+\mu & 0 \end{pmatrix} \quad \text{and} \quad \tilde{H}(\pi) = -i\begin{pmatrix} 0 & t-\mu \\ -t+\mu & 0 \end{pmatrix}. \tag{2.27}$$

If we calculate $\mathrm{Pf}(i\tilde{H}_{BdG}(k))$ for $k = 0$ and $k = \pi$, we recover the same point of phase transition as derived above in Sec. 2.2.2. $\mathrm{Pf}(i\tilde{H}_{BdG}(0)) = -t-\mu$ changes sign at $\mu = t$ and $\mathrm{Pf}(i\tilde{H}_{BdG}(\pi)) = t-\mu$ at $\mu = -t$. Note that we added an extra i to make the Pfaffian real. We can combine the two Pfaffians to obtain the topological invariant of the Bogoliubov-de-Gennes Hamiltonian

$$\mathcal{Q} = \mathrm{sign}(\mathrm{Pf}(i\tilde{H}_{BdG}(0))) \times \mathrm{sign}(\mathrm{Pf}(i\tilde{H}_{BdG}(\pi))). \tag{2.28}$$

This topological invariant can also be generalized to Floquet systems, as will be discussed in the next chapter.

2.2.5 Majorana box qubit

As discussed in Sec. 2.2.1, a one-dimensional topological superconductor can host Majorana zero modes at the edges [47]. The fermion formed by a pair of Majorana zero modes can encode a qubit in a non-local way. The non-locality of the stored quantum information protects it against local noise. Furthermore, Majorana modes obey non-Abelian braiding statistics [49, 50], which makes them a great candidate for topological quantum computation. Majorana based quantum computation is not universal as only Clifford gates can be implemented. Universal, physical topological quantum computing platform candidates are fractional Hall quantum systems which are currently not close to realization.

There has been a lot of experimental effort in realizing Majorana zero modes in condensed matter systems. However, what seemed theoretically relatively simple, has proven to be an arduous task in experiments. The main challenge is to *remove* the spin of the electron and obtain effectively spin-less electrons like in the Kitaev Hamiltonian (Eq. (2.8)). In principle, such systems can be realized in semiconducting quantum wires with strong spin-orbit coupling or in topological insulators, proximity coupled to conventional superconductors [51–58]. However, experimental evidence for Majorana zero-modes in those systems is still disputed.

In a single topological superconducting quantum wire, one could define a topological qubit by the occupation of the Majorana modes $q = i\gamma_1\gamma_2 = \pm 1$, where γ_1 and γ_2 are the two Majorana modes at the edges. However, for such a qubit, the information is encoded in the fermion number parity, and a coherent superposition of the two states is very difficult to prepare. Furthermore, long-range Coulomb interactions split the degenerate Majorana zero mode states into the even (not occupied) and odd (occupied) parity sectors if the system is not grounded. Thus, it is not possible to encode a useful qubit in a single wire. The most straightforward extension is adding another wire called the Majorana box qubit [46, 58–60]. A Cooper pair box with one topological quantum wire on top of each bulk superconductor forms a Majorana box qubit, as shown in Fig. 2.6. At low energy, we now have four states: no Majoranas, Majorana modes in only one of the wires, and Majorana zero modes at the edge of both wires. A relative charge between the wires costs a finite charging energy and splits the low-energy Hilbert space into odd (only one wire with Majoranas) and even parity sectors. The computational Hilbert space then reduces from four to two states. In the end, one obtains a single qubit by giving up one pair of Majorana modes for the fermion parity. Thus, the information is no longer encoded in the fermion parity, negating the issues that arise in a single wire. The Majorana box qubit can then be used as a hardware building block for topological quantum computers [59].

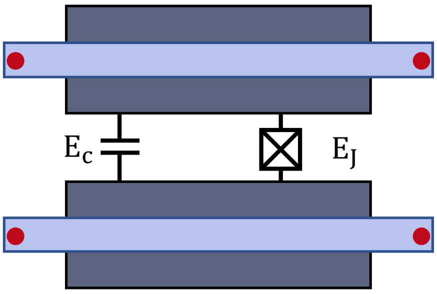

FIGURE 2.6: Schematic of the Majorana box qubit: The two bulk superconductors (dark blue) form a superconducting qubit effectively described by the Josephson tunneling element and a capacitor (see Fig. 2.1). Each bulk superconductor is proximity coupled to a topological quantum wire (light blue) that can host Majorana zero modes at the edges (red circle).

2.3 Quantum state preparation

Recommended additional literature for this section

1. Reviews on *"Quantum computational chemistry"* by S. McArdle and S. Endo [61], on *"Quantum algorithms for quantum chemistry and quantum material science"* by Bauer et al. [62] and on *"Quantum computer systems for scientific discovery* by Y. Alexeev et al. [63].
2. Reviews on the theory of variational quantum algorithms by McClean et al. [64] and Yuan et al. [65].
3. Review on adiabatic quantum computation by T. Albash [66] and lecture notes by A. M. Childs [67].
4. S. Polla et al. [68] use a very similar approach for *"Quantum digital cooling"* as introduced later in Chap. 5.

Among the most promising applications of quantum computing are the fields of quantum chemistry and material sciences [8, 61, 62, 69–72]. For example, for a known structure of an electronic ground state or thermal state of a given Hamiltonian, one can predict, e.g., reaction rates, location of stable structures, and optical properties [73]. More generally, it can also be utilized for various quantum information problems, e.g., optimization, which can often be mapped to the problem of finding the ground state of a Hamiltonian [74]. Therefore, the question of finding the ground state of a system is not only an academic problem but also has a significant impact on the industry. However, the computational complexity of realistic models of, e.g., high-temperature superconductivity or transition metal catalysis exceeds the capabilities of a classical computer [61]. Moreover, for a general Hamiltonian, even if it is spatially local, even a quantum computer struggles

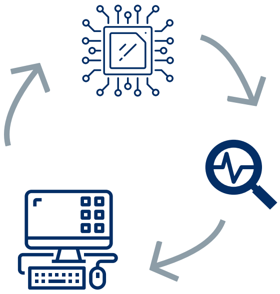

FIGURE 2.7: Variational quantum simulation is a hybrid simulation using a classical and a quantum computer. (1) A quantum state $|\psi(\theta)\rangle = U(\theta)\,|\psi\rangle$ is prepared on a quantum chip using unitary gates $U(\theta)$ parametrized by θ. (2) The expectation value of the energy $E(\theta)$ is measured by repeated initialization of $|\psi(\theta)\rangle$. (3) The measurement results are used to classically optimize the gates $U(\theta)$ to minimize the energy.

with efficiently solving for the ground states [75, 76].

Many approaches of ground state preparation are physically inspired like variational quantum simulation [64, 65, 77–81], adiabatic evolution [66, 82–84] and, more recently, also algorithms that mimic cooling by coupling to a "bath" [68, 85–90].

2.3.1 Variational quantum simulation

Variational quantum simulation uses the variational principle to approach the ground state from an initial guess wave function [64, 65, 77, 78]. It combines classical optimization with quantum state preparation and measurements, and, therefore, it is also called hybrid quantum computing.

The following steps are necessary to find the ground state of a Hamiltonian. First, the Hamiltonian needs to be written in terms of the qubit or spin operators. For an electronic Hamiltonian, the fermionic operators can be, e.g., transformed by a Jordan-Wigner or Bravyi-Kitaev transformation [91]. The Jordan-Wigner transformation is discussed in more detail for the Kitaev chain in Sec. 2.2.3. For specific cases like the Kitaev chain, the transformation is local in the target space. However, it introduces non-local string operators for general systems [64, 91]. The non-local string operators are either (quantum) computationally expensive or require highly connected qubits [63].

Next, one has to choose a good ansatz wave function $|\psi(\theta)\rangle$ parametrized by a classical variable θ. $|\psi(\theta)\rangle$ should be close to the real ground state function, and it must be possible to prepare the state on the quantum computer. The performance of variational quantum simulation is highly dependent on the quality of the variational ansatz that is often as challenging to find. After the state preparation, the

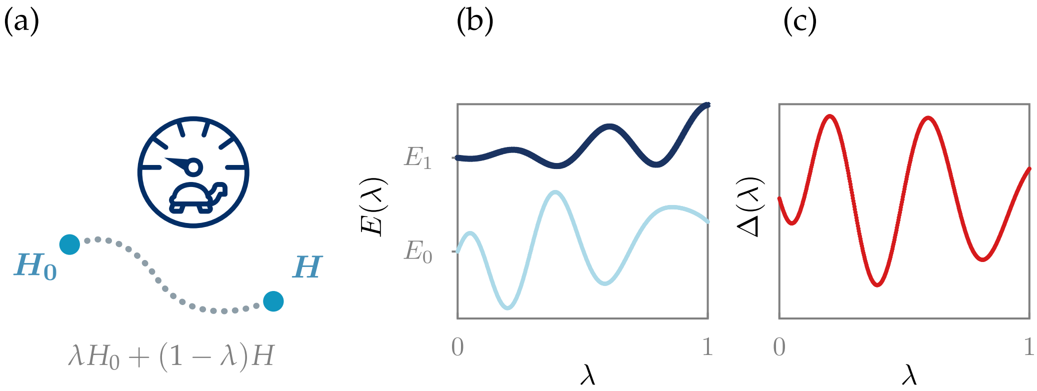

FIGURE 2.8: (a) The parameter λ is slowly changed to find a path from the initial Hamiltonian H_0 to the Hamiltonian of interest H. (b) Exemplifying energy dispersion along a path λ. (c) The gap between the ground state and the first excited state. The system is initially prepared in the ground state of H_0. Only if the parameter λ is very slowly swept with respect to the energy gap, the system stays in the ground state. Optimizing the sweep's speed according to the gap along the path is challenging because the energy dispersion is usually unknown.

expectation value of the Hamiltonian,

$$E(\theta) = \langle\psi(\theta)| H |\psi(\theta)\rangle , \tag{2.29}$$

is evaluated by repeated state preparation and measurement of the Hamiltonian. Using the variational principle,

$$E_0 \leq \langle\psi(\theta)| H |\psi(\theta)\rangle , \tag{2.30}$$

one can find the ground state wave function by classically optimizing the variable θ. For example, the state $|\psi(\theta)\rangle$ can be prepared by starting in the computational ground state and applying unitary gates parametrized by θ

$$|\psi(\theta)\rangle = U(\theta) |0\rangle . \tag{2.31}$$

The parameter(s) θ are optimized by a classical computer. This method always gives at least an upper bound to the ground state energy.

2.3.2 Adiabatic state preparation

Adiabatic quantum computing is a very powerful method since it has been shown to be equivalent to *standard* (gate-based) quantum computing [92].

The strategy of adiabatic state preparation is to start with a ground state $|\psi_0\rangle$ of a reference Hamiltonian H_0 that is easy to prepare on a quantum computer. Then, the state is slowly evolved with a Hamiltonian $H(t)$ that connects the reference Hamiltonian H_0 to the Hamiltonian H of interest

$$H(t) = (1 - \lambda(t))H_0 + \lambda(t)H. \tag{2.32}$$

Without specifying the exact path, the parameter $\lambda(t)$ starts at zero and ends with the value of one. The adiabatic theorem guarantees that the system stays close to the ground state during the evolution. Thus, at the end of the evolution, the system is close to the ground state of H.

This method had two major drawbacks: Firstly, an adiabatic evolution of the Hamiltonian, i.e., the adiabatic tuning of the system parameters, needs time. A slow preparation process adds up if the measurement has to be repeated many times to measure an expectation value with high precision.

Secondly, the adiabatic theorem breaks down if a phase transition separates the initial and the target state. The sweeping rate must be slower than $1/\Delta$, where Δ is the gap between the ground state $E_0(t)$ and the first excited state $E_1(t)$. The sweep duration T tends to depend strongly on the system size and the choice of the reference Hamiltonian [62]. In the worst case, the sweep duration T scales as

$$T \sim \mathcal{O}\left(\frac{1}{\mathrm{min}_t \Delta(t)^3}\right), \tag{2.33}$$

where it is essential to know the minimum gap $\Delta_{min} = \mathrm{min}_t \Delta(t)$ along the path [93]. This upper bound can be improved to $\mathcal{O}(1/\Delta_{min}^2)$ up to a polylogarithmic factor in Δ_{min} for a sufficiently smooth variation of the Hamiltonian [66, 94]. Generally, the minimum gap during the evolution is unknown and has to be approximated. At a phase transition, however, the gap vanishes in the thermodynamic limit and $T \to \infty$ [95]. Hence, the ground state of a topological Hamiltonian cannot efficiently be prepared by starting with a *simple* product state because they are not smoothly connected.

2.3.3 Quantum refrigerator

More recently, algorithms have been proposed that mimic how a physical system is cooled by coupling it to a low-entropy "bath" [68, 85–90]. Following the fundamental laws of thermodynamics, a system should approach its ground state when the temperature decreases to zero. When cooling a physical system, the bath has to be much larger than the system. Otherwise, the bath itself heats up. In the case of algorithmic cooling on a quantum computer, a fraction of the qubits is used to simulate the bath. If the bath is periodically reset to its ground state, energy and entropy can be extracted from the system. Thus, the bath size does not have to be larger than the system.

The key advantage of such a cooling algorithm is that it is independent of the initial state of the system and requires no prior knowledge of the target ground state. The target state does not need to be adiabatically connected to a product state. Building on these ideas, in Chapter 5, we investigate a cooling algorithm inspired by adiabatic demagnetization.

2.3.4 Preparation of known complex quantum states

In the previous sections, we discussed techniques that (approximately) prepare the unknown ground state of an Hamiltonian of interest. This section focuses on quantum states that exhibit interesting features and might even be easily written down on paper. Does this mean that the state is easy to prepare on a quantum computer and why is that even relevant?

In quantum many-body physics, a particular class of ground states has brought much excitement, namely those with long-range entanglement. The topological nature of these states makes them a very powerful tool for quantum computing. In contrast to topological quantum hardware, see Sec. 2.2, one can use them to encode logical qubits consisting of many physical qubits. Error correction codes like the surface code take advantage of this feature, and, thus, act like "topological quantum software". A quantum state with long-range entanglement, by definition, cannot be prepared by a finite-depth local unitary [96]. For example, one can imagine a circuit with only two-qubit gates, see Fig. 2.9a spreading the entanglement like a light cone [97]. Even for finite-size systems, a circuit depth that scales with the system size is challenging to realize on current quantum computers because gate operations are costly.

In the remainder of this section, we discuss the implementation of the toric ground state as an example for long-range entanglement. We use this example to show how a combination of unitaries, measurements and feed-forward can prepare a ground state with long-range entanglement in finite depth, i.e., independent of the system size.

The toric code model which has been proposed to realize fault tolerant quantum computation [21]. This toric code has a ground state with topological order and anyonic braiding statistics. The Hamiltonian is defined on links of a square lattice

$$H = -\sum_{s} A_s - \sum_{p} B_b, \tag{2.34}$$

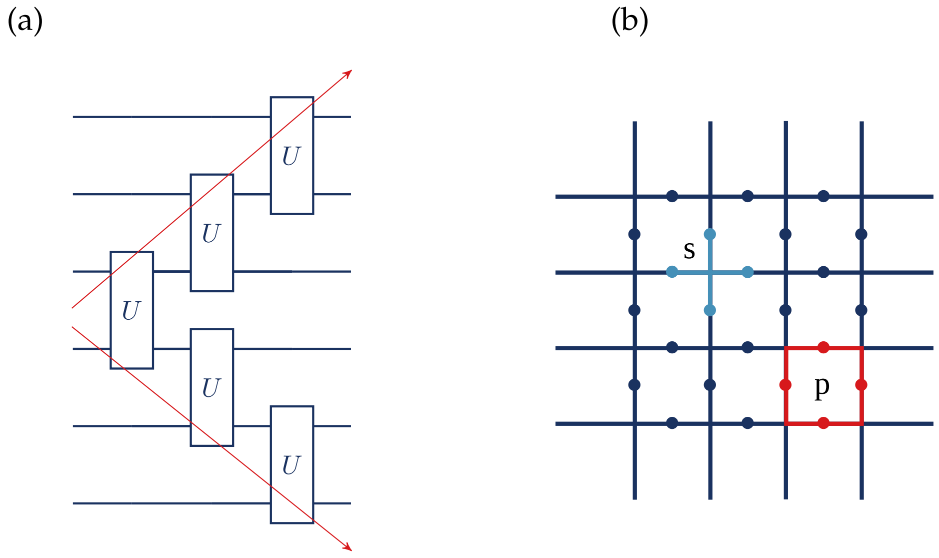

FIGURE 2.9: (a) Information spreading in a relativistic theory is bounded by the speed of light captured by the light cone. Similarly, the entanglement spreading in many interacting many-body systems is bounded by the Lieb Robinson bound [96–98], here visualized has two-qubit entangling operations that propagate the correlations. (b) The toric code model is defined on the links of a square lattice. The "star" operator $A_s = \sum_{i \in s} \sigma_i^z$ acts on the vertices (light blue), while $B_p = \sum_{i \in p}$ is defined for a plaquette (red).

where the "star" operators $A_s = \prod_{i \in s} \sigma_i^z$ act on vertices and the "plaquette" operators $B_p = \prod_{j \in p} \sigma_j^x$ on plaquettes, respectively, see Fig. 2.9. One can realize that the ground state $|GS\rangle$ of Eq. (2.34) must be an eigenstate of all individual plaquette and star operators simultaneously with eigenvalue $+1$ such that $A_s |GS\rangle = B_p |GS\rangle = + |GS\rangle$. Such a state can be formally implemented by initializing all qubits in the $|0\rangle^{\otimes N}$ state, and thus, a $+1$ eigenstate of all A_s operators. Then, the ground state is obtained by projecting the $|0\rangle^{\otimes N}$ to the $+1$ B_p-eigenstates as

$$|GS\rangle = \frac{1}{\mathcal{N}} \prod_p (\mathbb{I} + B_p) |0\rangle^{\otimes N},$$

where $\mathcal{N}$ normalizes the state. Satzinger et al. prepared this ground state on 31 superconducting qubits by a sequence of Hadamard and CNOT gates that effectively implement the projector $\mathbb{I} + B_p$ [14]. Thus, the preparation of such a topologically-ordered state is not restricted to pen and paper. However, it is known that the optimal circuit depth, i.e., the number of necessary gate layers, scales linear with the system width [98]. The long-range entanglement is also the reason, why adiabatic state preparation fails, see Sec. 2.3.2, – the long-range entangled state is topologically distinct from a product state.

However, one can take a shortcut to realize the toric code ground state using measurements. Instead of applying unitary gates, one can project into the B_p and

A_s eigensectors by measuring once these commuting operators. All star (plaquette) operators can be measured in parallel, thus, requiring only two measurement steps. Furthermore, starting from the state $|0\rangle^{\otimes N}$ only the B_p measurements are necessary because the state is already an eigenstate of all A_s. Measurements, of course, randomly select the $+1$ and -1 eigenstates. However, the -1 excitations always come and pairs and can be eliminated by a feed-forward layer of σ^x-string operators [21]. Feed-forward means using the classical information, i.e. the measurement results, to identify the errors and correct them.

The above approach generalizes for commuting projector Hamiltonians that exhibit Abelian topological order [21, 99, 100]. For non-Abelian topological order, the excitations cannot be removed using a finite-depth circuit [101]. However, other strategies with several measurement and feed-forward layers have been recently proposed [102–105].

Finally, let us remark on the Lieb-Robinson bound [96], that bound on the speed of entanglement spreading is not lifted by measurements alone. The trick lies in the feed-forward step that classically communicates the information about the measurement results.

Chapter 3

Non-Equilibrium Dynamics

"Let's face it, the universe is messy. It is nonlinear, turbulent, and chaotic. It is dynamic. It spends its time in transient behavior on its way to somewhere else, not in mathematically neat equilibria. It self-organizes and evolves. It creates diversity, not uniformity. That's what makes the world interesting, that's what makes it beautiful, and that's what makes it work. " — Donella H. Meadows

There has been remarkable progress in the theoretical and experimental understanding of non-equilibrium processes in closed and open systems. A closed system is isolated from any environment. In contrast, an open system considers the interaction with an environment that is not itself fully characterized.

The first part of this chapter focuses on closed Floquet systems. Floquet theory describes systems that are periodically driven. A Floquet system can be realized in solid-state, e.g., by using a laser, and in synthetic systems like quantum computing devices. A time-periodic field can generate new non-equilibrium phases with no static equivalent. The properties of the system, like the band mass, lifetime, and topological order can be drastically changed and even be controlled by "Floquet engineering".

Interesting effects can also be observed in driven open systems. However, the last part of this chapter instead focuses on the impact of measurements and noise in open systems, since noise cannot be neglected in current quantum computing devices. Furthermore, only through measurements can one observe the quantum world.

3.1 Floquet theory

Recommended additional literature for this section

1. The section mainly follows the reviews by M. S. Rudner and his collaborators [11, 106].
2. There exist many more reviews on (topological) Floquet systems [9–11, 107–111].
3. The Bloch theorem is a special case of the Floquet theorem. Many concepts of Floquet systems are related to spatially translational invariant systems (see your favourite condensed matter textbook).
4. Suzuki-Trotter decomposition [112].

Floquet theory [17] is a powerful tool set to describe periodically driven systems. For a time-periodic Hamiltonian $H(t) = H(T+t)$, we can write the the Schrödinger equation

$$i\hbar\partial_t|\psi(t)\rangle = H(t)|\psi(t)\rangle. \tag{3.1}$$

The dynamics of the system can be well described by the Floquet time evolution operator, which is defined over one cycle of the drive,

$$U(T) = \mathcal{T}e^{-\frac{i}{\hbar}\int_0^T \mathrm{d}t' H(t')}, \tag{3.2}$$

where $\mathcal{T}$ is the time ordering [106]. The stationary states of the Floquet time evolution operator and the corresponding eigenenergies, called quasi-energies, define a good basis for analyzing Floquet systems and will be thoroughly discussed in this section. We will first introduce the Floquet theorem, a fundamental concept in Floquet theory. The Floquet theorem may seem familiar as the Bloch theorem is a particular case of the Floquet theorem. By driving the system periodically, continuous time translation symmetry is broken. Thus, energy is not conserved any more. In analogy to crystals and the crystal momentum, only the quasi-energy, that is the energy modulo the driving frequency, is conserved.

We will encounter that new topological phases with no equivalent in equilibrium like Floquet Majoranas may arise in Floquet systems. However, due to the lack of energy conservation, Floquet systems are always at the risk to heat up to infinite temperatures such that the interesting states cannot be observed. Luckily, Floquet system are still closer to equilibrium than systems with generic drives since they are discrete time-translational symmetric. In a system with $\mathcal{O}(N)$ conserved quantities heating can be avoided [109]. Driven free fermion systems like the driven Kitaev chain, which we discuss later, fall in this category [113]. Furthermore, Floquet systems exhibiting many-body localization allow for interesting long-time steady states [114–116]. Finally, one can investigate the stability of Floquet phases in the presence of interactions, e.g., using Fermi's golden rule which is introduced at the end of this section.

3.1.1 Floquet theorem

Instead of solving for the stationary states of the time evolution operator and integrating the Schrödinger equation mentioned above, there is an elegant way to solve the problem using the Floquet theorem. The Floquet theorem converts the problem from time space into frequency space. In frequency space, one only has to solve a matrix equation. A time-periodic Hamiltonian $H(t) = H(t+T)$ can be decomposed as

$$H(t) = H_0 + \sum_n H_n e^{i\omega n t} \tag{3.3}$$

with the driving frequency $\omega = 2\pi/T$. The quasi-stationary states $\{|\Psi_i(t)\}$ of the Hamiltonian $H(t)$

$$|\Psi_i(t)\rangle = e^{-i\epsilon_i t}|\psi_i(t)\rangle, \qquad |\psi_i(t)\rangle = |\psi_i(t+T)\rangle \tag{3.4}$$

form a complete orthonormal basis, where $|\psi_i(t)\rangle$ is itself periodic in time. Therefore, we further decompose $|\psi_i(t)\rangle$ in Fourier components

$$|\psi_i(t)\rangle = e^{-i\omega n t} \sum_n |\psi_i^n\rangle. \tag{3.5}$$

With this ansatz and $\hbar = 1$, we can rewrite the Schrödinger equation, Eq.(3.1), as

$$\sum_n (\omega n + \epsilon_i) e^{-i\omega n t} |\psi_i^n\rangle = H_0 \sum_n e^{i\omega n t} |\psi_i^n\rangle + \sum_{n,m} H_n e^{i\omega(n+m)t} |\psi_i^m\rangle, \tag{3.6}$$

where we cancelled out the factor $e^{i\epsilon_i t}$. Each Fourier-component $\left|\psi_i^m\right\rangle$ is coupled to the other components through the drive coupling $H_{m-m'}$

$$(\epsilon_i + m\omega)\,|\psi_i^m\rangle = \sum_{m'} H_{m-m'} \left|\psi_i^{m'}\right\rangle. \tag{3.7}$$

Eq. (3.7) can be expressed as an (infinitive size) matrix equation $\mathcal{H}\boldsymbol{\psi_i} = \epsilon_i \boldsymbol{\psi_i}$ [106], where we define the vector $\boldsymbol{\psi_i} = (\dots, \left|\psi_i^{-1}\right\rangle, |\psi_i^0\rangle, |\psi_i^1\rangle, \dots)^T$ with the Fourier components as entries and $\mathcal{H}$ as

$$\mathcal{H} = \begin{pmatrix} \cdots & H_{-1} & H_{-2} & & & & \cdots \\ H_1 & H_0 + 2\omega & H_{-2} & & & \cdots & \\ H_2 & H_1 & H_0 + \omega & H_{-1} & H_{-2} & & \\ & H_2 & H_1 & H_0 & H_{-1} & H_{-2} & \\ & & H_2 & H_1 & H_0 - \omega & H_{-1} & H_{-2} \\ & \cdots & & H_2 & H_1 & H_0 - 2\omega & H_{-1} \\ \cdots & & & & H_2 & H_1 & \cdots \end{pmatrix}. \tag{3.8}$$

The Hilbert space of the Floquet matrix $\mathcal{H}$ is much larger than the Hilbert space of the original Hamiltonian $H(t)$. It is over-complete and has an infinite number of eigenstates. The solutions are linearly dependent and encode the same physical solutions since we introduced infinite copies of the original Hilbert space. The associated eigenvalues are the so-called quasi-energies of the system and can be shifted by multiples of the driving frequency

$$\begin{aligned} |\psi_i(t)\rangle &= e^{-i(\epsilon_i + m\omega)t} \sum_n e^{-i(n-m)\omega t} |\psi_i^n\rangle \\ &= e^{-i\tilde{\epsilon}_i t} \sum_n e^{-in\omega t} |\tilde{\psi}_i^n\rangle , \end{aligned} \tag{3.9}$$

where $\tilde{\epsilon}_i = \epsilon_i + m\omega$ and $\left|\tilde{\psi}_i^n\right\rangle = e^{im\omega t} \left|\psi_i^n\right\rangle$. Therefore, it is enough to look at only one Floquet-Brillouin zone with eigenvalues $\epsilon_{min} \leq \epsilon < \epsilon_{min} + \omega$.

3.1.2 Solving the Floquet matrix

In the previous section, we have seen that one can elegantly rewrite a time-periodic Hamiltonian in a Floquet decomposition. However, this technique seems a bit useless since it blows up the Hilbert space to infinity and gives us infinite equivalent solutions. As we will discuss in the following, the structure of the Floquet matrix leads to a convenient approximation of the problem and nice physical intuition. For the discussion, we simplify the problem and analyze a Hamiltonian $H(t) = H_0 + V(t)$ with a static part H_0 and a time-periodic part $V(t) = Ve^{i\omega t} + V^\dagger e^{-i\omega t}$. We can construct the Floquet matrix

$$\mathcal{H} = \begin{pmatrix} \cdots & V & & & \\ V^\dagger & H_0 + \omega & V & & \\ & V^\dagger & H_0 & V & \\ & & V^\dagger & H_0 - \omega & V \\ & & & V^\dagger & \cdots \end{pmatrix}, \tag{3.10}$$

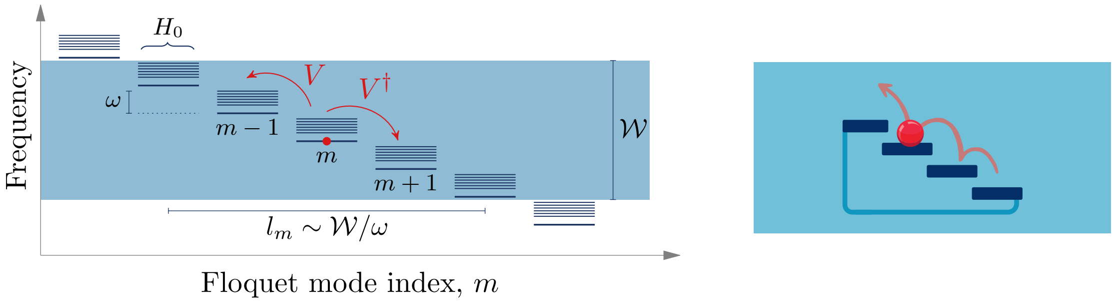

FIGURE 3.1: Floquet Matrix as a potential ladder: The Floquet matrix equation, Eq. (3.8), can be interpreted as a particle hopping on a chain where a decreasing electric field along the chain acts as a potential ladder. Within this analogy, the Floquet mode index m corresponds to a site m, and the Floquet states' frequency corresponds to the Bloch states' momentum. Within each unit cell m, the physics, i.e., all energies and couplings, are governed by the time-averaged Hamiltonian H_0. The energies between two unit cells are shifted by ω according to the diagonal of the Floquet matrix. A drive with only a single harmonic induces hopping V between neighboring sites (see Eq. (3.10)). Without the linear potential, the eigenstates have a total bandwidth $\mathcal{W} \sim \max\{||V||, ||H_0||\}$. The potential leads to a wave function localization in m space. Semi-classically, this can be understood as an effective particle with a finite kinetic energy that can only access sites in the range of $l_m \sim \mathcal{W}/\omega$. This figure is inspired by Fig. S2 of Ref. [106].

where $H_1 = V^\dagger$, $H_{-1} = V$ and $H_{|m|} = 0$ for $|m| > 1$. The static Hamiltonian, H_0 on the diagonal, is shifted by multiples of the frequency. On the off-diagonal blocks, V and $V^\dagger$ couple different frequency sectors by the driving. This Hamiltonian looks like a tight-binding Hamiltonian with nearest neighbor hopping on a lattice and a linear potential (see Fig. 3.1). Without the potential ($\omega = 0$), H_0 describes the on-site energies and intra-unit-cell hopping, whereas V and $V^\dagger$ account for inter-unit-cell hopping in frequency space. For a one-dimensional Hamiltonian, the bandwidth of the kinetic energy is given by $\mathcal{W} = 2|V|$. In higher but finite dimensions, the bandwidth can be approximated as $\mathcal{W} \approx \max\{\|V\|, \|H_0\|\}$. The wave functions in the absence of the potential are extended in frequency space, but they become localized once $m\omega$ is finite. The localization occurs due to the finite bandwidth of the kinetic energy. The effective particle doesn't have enough kinetic energy to climb the potential ladder. More precisely, the total energy $E = E_{kin} + E_{pot}$ of the particle is only constant over a finite range l_m of multiples m of the frequency. The accessible range at a given quasi-energy ϵ_i can be approximated by $l_m \sim \frac{\mathcal{W}}{\omega}$. Outside that range, the wave function is falling off (faster than) exponentially in m. Therefore, only a finite number of Floquet copies strongly contribute to a wave function with quasi-energy ϵ_i. One can truncate the Floquet matrix and achieve a solution with arbitrary accuracy. Note that at the boundary of the truncation, the solutions might strongly deviate, but the Floquet zone in the middle gives accurate results. The Floquet matrix approach is useful if the driving frequency is sufficiently big such that not too many Floquet copies have to be considered. Using this approach, we can, for example, analytically investigate the Floquet Majorana box qubit, see Chap. 4.

3.1.3 Suzuki-Trotter decomposition

Another approach to solving the problem is to numerically compute the time evolution operator $U(T) = \mathcal{T}e^{i\int_0^T \mathrm{d}t' H(t')}$, where the time ordering is important [112]. We can write the time evolution operator as a product of time slices,

$$U(T) = \prod_{n=0}^{N} e^{iH(\frac{nT}{N})\frac{T}{N}}. \tag{3.11}$$

Eq. (3.11) is only exact in the limit $N \to \infty$ or if the Hamiltonian commutes at different times. For finite N, Eq. (3.11) is the simplest Suzuki-Trotter decomposition with a correction of $\mathcal{O}(\frac{T^2}{N})$. We can confirm the relation for two non-commuting operators A and B by expanding the exponential operator up to the first order

$$e^{\delta(A+B)} = \mathbf{1} + \delta(A+B) + \frac{1}{2}\delta^2(A^2 + AB + BA + B^2) + \mathcal{O}(\delta^3) \tag{3.12}$$

$$e^{A}e^{B} = \mathbf{1} + \delta(A+B) + \frac{1}{2}\delta^2(A^2 + 2AB + B^2) + \mathcal{O}(\delta^3). \tag{3.13}$$

In the second line, the operator A only comes from the left. Since A and B don't commute, the difference between the two lines arises. The 2nd order Suzuki-decomposition removes the difference from the commutator by applying $B/2$ from both sides. For N time steps, we arrive at

$$\left(e^{\frac{B}{2}}e^{A}e^{\frac{B}{2}}\right)^N = \left(e^{\delta(A+B)+\mathcal{O}(\delta^3)}\right)^N = e^{T(A+B)+\mathcal{O}(\frac{T^3}{N^2})}, \tag{3.14}$$

where $\delta = T/N$ is the length of a single time step [112]. The advantage of time slicing the time evolution operator instead of interrupting the Taylor expansion of the exponential function at the same order, e.g., $e^{\delta(A+B)} = 1 + \delta(A+B) + \mathcal{O}(\delta^2)$, is that the time slices are still unitary operators. Thus, the exponential form conserves the norm of the wave function, whereas the perturbative approximation generally leads to an increase in the norm. Furthermore, the matrix $(m \times m)$, describing the time evolution operator, is not artificially enlarged compared to the Floquet matrix $((2N+1)m \times (2N+1)m)$, m is the dimension of the Hilbert

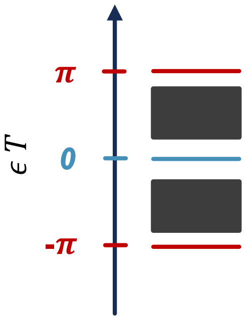

FIGURE 3.2: Schematic of a Floquet system with particle-hole symmetry: The Floquet bulk is plotted in black. Interestingly, there are two special energies, where negative and positive quasi-energies ϵ are the same $\epsilon T = -\epsilon T$. This condition is only fulfilled in equilibrium when $\epsilon = 0$ (blue) leads to the emergence of Majorana zero modes. Due to temporal translational invariance, $\epsilon T = \pi$ ($\epsilon = \omega/2$) is equivalent to $\epsilon T = -\pi$ (red). Therefore, Floquet systems can host additional Majorana π modes, also called Floquet Majoranas.

space and N the number of Floquet modes. Using the Suzuki-Trotter decomposition, one can compute the quasi-energy spectrum of the Floquet Hamiltonian $H_F = i\log(U(T))/T$. In practice, the quasi-energies $\epsilon_i = iu_i/T$ can be obtained by solving for the eigenvalues u_i of $U(T)$. In the next section, we use this approach to calculate the spectrum of the driven Kitaev chain.

3.2 Floquet spectrum and topology

Recommended additional literature for this section

1. Two reviews by M. S. Rudner and his collaborators [11, 106]
2. The topological invariant calculation follows Refs.[117, 118] by L. Jiang et al. and B. Bauer et al.
3. For concepts of topology in equilibrium see Sec. 2.2.4
4. The Floquet Fermi golden rule calculation follows Ref.[119] by T. Bilitewski and N. R. Cooper

By engineering a time-periodic drive, we can design systems that have rich non-equilibrium topological phases [11]. These topological phases don't necessarily have an equilibrium counterpart and thus, are fascinating to investigate in theory [117, 120–125] as well as in experiments [126–128].

For non-interacting systems, the topology of a system can be characterized in terms of time-reversal, particle-hole and chiral symmetries. The topology is encoded in the band spectrum, see Sec. 2.2.4. However, in a Floquet system, the ground state is not well-defined anymore and we need to expand the notion of the system's topology from the Hamiltonian to the time-evolution operator [11].

For example, the particle-hole symmetry of the time evolution operator can be enforced by an particle-hole symmetric Hamiltonian $H(t)$ at every time instance. This symmetry is always present for a superconductor at the mean-field level, i.e., if the system is described by a Bogoliubov- de Gennes Hamiltonian.

In the previous sections, we have discussed how one can obtain the quasi-energy spectrum of the effective Floquet Hamiltonian $H_F = i\log(U(T))/T$. In Fig. 3.2, we show the pictographic Floquet spectrum of a Hamiltonian with particle-hole symmetry. Importantly, the spectrum has two special quasi-energies, where the positive quasi-energy equals the negative,

$$\epsilon = -\epsilon, \tag{3.15}$$

namely not only at $\epsilon = 0$, but also at $\epsilon = \frac{\omega}{2}$. In the previous chapter, we have seen that localized Majorana zero edge modes can only arise at energy $E = 0$ in equilibrium for a spin-less superconductor. Due to the particle-hole symmetry, particle and anti-particle have the same energy only at $E = 0$. Here, the presence of another quasi-energy $\epsilon = \frac{\omega}{2}$ with the same property already hints that many new phenomena can arise in a non-equilibrium setup. In particle-hole symmetric case, so called Floquet Majoranas emerge [117, 129, 130]. This non-equilibrium topological mode is introduced in detail in the next section followed by the notion of the corresponding Floquet topological invariant.

While topological systems are protected by the band gap in equilibrium, this protection is lost in a driven set-up. In Floquet systems only quasi-energy is conserved. By driving the system, energy is continuously pumped into the system. In (clean) free fermion models, like the Kitaev chain, heating is avoided due to the extensive number of conservation laws [113]. But already weak interaction effects can lead to thermalization in Floquet systems [109]. At the end of this section, we introduce a tool, the Floquet Fermi's golden rule, to approximate the heating effect by weak perturbations. We will later use the Fermi's golden rule to investigate the stability of the Floquet Majorana box qubit in Chap. 4.

3.2.1 Floquet Majoranas

Floquet Majoranas can arise in a periodically driven topological spin-less superconductor [117, 118, 129]. As the simplest example, we will introduce an additional drive to the one-dimensional Kitaev chain (Eq.(2.8))

$$H^F_{Kitaev}(t) = \sum_i -\left(\bar{\mu} + \delta\mu\cos(\omega t)\right) c_i^\dagger c_i - t/2 c_i^\dagger c_{i+1} + \Delta/2 c_i c_{i+1} + h.c., \tag{3.16}$$

where $\bar{\mu}$ is the static chemical potential, $\delta\mu$ is the amplitude of the drive and ω the driving frequency. As for the equilibrium case, we consider spin-less electrons hopping on a one-dimensional chain with an amplitude t and a superconducting pairing Δ. In analogy to the example discussed in Sec. 3.1.2, the Floquet matrix can be constructed with blocks $H_0 - m\omega$ on the diagonal,

$$H_0 = \sum_i -\bar{\mu} c_i^\dagger c_i - t/2 c_i^\dagger c_{i+1} + \Delta/2 c_i c_{i+1} + h.c., \tag{3.17}$$

and the coupling ,

$$V = V^\dagger = -\delta\mu \sum_i c_i^\dagger c_i, \tag{3.18}$$

on the off-diagonal. The spectrum can also be computed by the trotterized time-evolution operator as explained in Sec. 3.1.3. The spectrum reveals two important features, see Fig. 3.3a. The spectrum shows three different phases as a function of the chemical potential. The system can host Majorana zero modes that also appear in an undriven setup. Additionally, Floquet Majoranas arise at a quasi-energy $\frac{\omega}{2}$. Since $\frac{\omega}{2} = \frac{\pi}{T}$, these modes are also called Majorana π modes. Both modes are localized at the edges. However, they are distinct in quasi-energy and don't hybridize. Therefore, both modes can also coexist. As shown in the phase diagram of Fig. 3.3b, a trivial fourth phase without any topological modes can also exist. The phase diagram is obtained by calculating the bulk topological invariant introduced in the next section [117, 118]. The phase diagram is periodic in the chemical potential as well as the tunneling. However, the spectrum shows a decreasing gap around the topological modes for larger chemical potential.

3.2.2 Floquet topological invariant

Floquet systems can possess more diverse topological phases than static systems. Therefore, it is not sufficient to characterize them with equilibrium topological invariants only. Instead, we need to expand the description of topological invariants

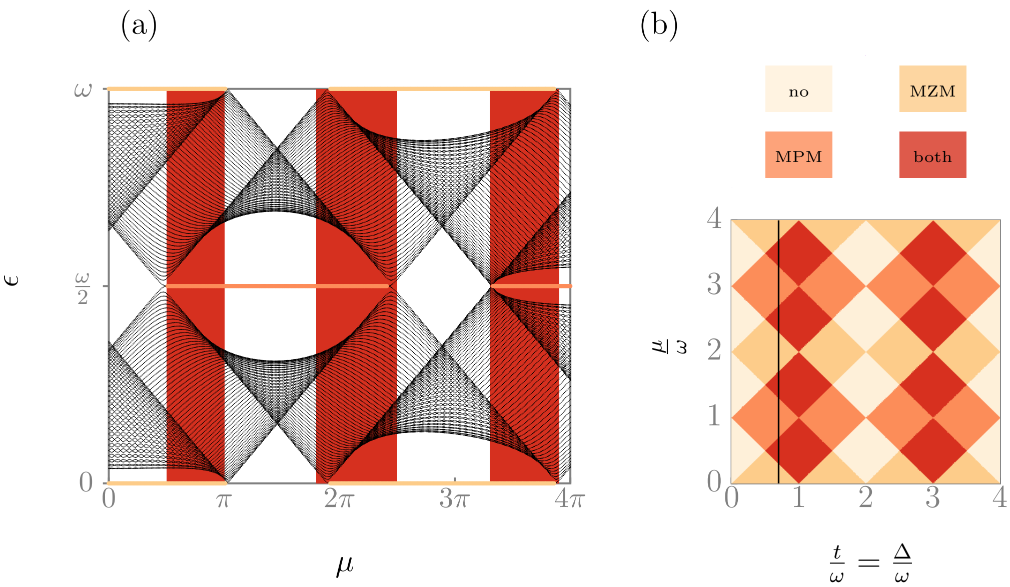

FIGURE 3.3: (a) Floquet spectrum as a function of the static chemical potential μ ($N = 60$, $\delta\mu = 3\pi$, $t = \pi$, $T = 1.4$, $N_{\text{steps}} = 100$, $\Delta = -\pi$). The Majorana zero mode (MZM, light orange) and the Majorana π modes (MPM, orange) can coexist (red-shaded areas). (b) Phase diagram of the driven Kitaev chain, as a function of $\frac{t}{\omega} = \frac{\Delta}{\omega}$ and $\frac{\mu}{\omega}$, shows four different phases: trivial, only MZM, only MPM, and both modes. This figure is reproduced from Ref. [P131]

to include topological phases that can only appear in a driven system. We exemplify this concept for the driven Kitaev chain following Refs.[117, 118]. For a general classification of Floquet topological phases, we refer the reader to Ref. [121]. As discussed in the previous section, the time-periodic Kitaev chain can host both Majorana zero modes and Majorana π modes at quasi-energy 0 and $\omega/2$, respectively. Thus, our goal is to derive two topological invariants $\mathcal{Q}_0$ and $\mathcal{Q}_\pi$ that can capture whether the system can host Majorana zero modes ($\mathcal{Q}_0 = -1$) and Majorana π modes ($\mathcal{Q}_\pi = -1$).

This section builds on Sec. 2.2.4, where the ground state fermion number parity is introduced as the topological invariant of a BdG Hamiltonian [41]. However, instead of the instantaneous Hamiltonian, the time evolution operator contains information about the system's topology in the Floquet case.

We start by transforming the Floquet Kitaev Hamiltonian of Eq. (3.16) into momentum space $H = \sum_k H_k^F(t) |k\rangle \langle k|$, where

$$H_k^F(t) = -(\mu(t) + t\cos(k))\tau_z + \Delta\sin(k)\tau_y \tag{3.19}$$

with $\mu(t) = \bar{\mu} + \delta\mu\cos(\omega t)$. Then the time-evolution operator has a momentum decomposition

$$U(T) = \prod_k U_k(T), \qquad U_k(T) = \mathcal{T} e^{-i\int_0^T \mathrm{d}t H_k^F(t)}, \tag{3.20}$$

where T is the period of the drive. Like the equilibrium case, the topological phase transition happens when the gap closes at the quasi-energy 0 and $\omega/2 = \pi/T$. This gap closure happens at the momenta $k = 0$ and $k = \pi$. Thus, monitoring the eigenvalues of $U_0(T)$ and $U_\pi(T)$ is sufficient. The topological charges $\mathcal{Q}_0$ and $\mathcal{Q}_\pi$ count how many times the eigenvalues of the time evolution operator cross $1 = e^{i0}$ and $-1 = e^{i\pi}$, respectively, and distinguishes whether this number is even or odd. We can write this number parity

$$\mathcal{Q}_0\mathcal{Q}_\pi = \text{sign}\left(\text{Pf}[M_0]\text{Pf}[M_\pi]\right), \qquad \mathcal{Q}_0 = \text{sign}\left(\text{Pf}[N_0]\text{Pf}[N_\pi]\right), \tag{3.21}$$

where $M_k = \log(U_k(T))$ and $N_k = \log\left(\sqrt{U_k(T)}\right)$ and only the momenta $k = 0, \pi$ of the gap closure are important [117]. Eq. (3.21) uses the Pfaffian to define the sign of the eigenvalue uniquely; see Sec. 2.2.4 for details on the Pfaffian. As discussed below, $\mathcal{Q}_0$ is equivalent to the equilibrium topological invariant. For $k = 0, \pi$, the different time instances of the time evolution operator commute, and we can calculate the Pfaffian

$$\text{Pf}[M_k] = \log\left(e^{iT(\bar{\mu}+t\cos(k))}\right), \qquad \text{Pf}[N_k] = \log\left(e^{i\frac{T}{2}(\bar{\mu}+t\cos(k))}\right), \tag{3.22}$$

where $\log\left(e^{ix}\right)$ can only resolve $0 \le x < 2\pi$. $\text{Pf}[N_k]$ changes sign if $T(\bar{\mu} + t\cos(k)) = 2n\pi$, i.e. if the quasi-energy crosses 0. Therefore, it monitors the change of Majorana zero mode parity. On the other hand, $\text{Pf}[M_k]$ changes sign if $T(\bar{\mu} + t\cos(k)) = n\pi$. This condition is fulfilled if the quasi-energy crosses 0 (n even) or $\omega/2$ (n odd or even). Thus, the joint parity of the two topological modes changes in this case.

We can further simplify the sign of the Pfaffian into a more convenient form using

$$\text{sign}(\log\left(e^{ix}\right) = (-1)^{\lfloor x \rfloor}, \tag{3.23}$$

where $\lfloor x \rfloor = \text{floor}(\frac{x}{2\pi})$. Now, the topological invariants have the form

$$\mathcal{Q}_0 = (-1)^{\lfloor(\bar{\mu}+t)T\rfloor}(-1)^{\lfloor(\bar{\mu}-t)T\rfloor}, \qquad \mathcal{Q}_0\mathcal{Q}_\pi = (-1)^{\lfloor(\bar{\mu}+t)\frac{T}{2}\rfloor}(-1)^{\lfloor(\bar{\mu}-t)\frac{T}{2}\rfloor}. \tag{3.24}$$

In this form, the topological invariant can also be interpreted as how many times the time-averaged energy $\bar{E}_k = -\frac{1}{T}\int_0^T(\mu(t) + t\cos(k)) = \bar{\mu} + t\cos(k)$ is folded back to the first Floquet zone [118]. In the Majorana zero mode phase, $\bar{E}_k$ is folded back for an odd number of times and $\mathcal{Q}_0 = -1$. Like in equilibrium, the phase transition happens at $\mu = t$ and $\mu = -t$. To calculate $\mathcal{Q}_0\mathcal{Q}_\pi$, the period is doubled, and the quasi-energy of the π mode is mapped to 0. The presence of Majorana π modes is captured by $\mathcal{Q}_\pi = \mathcal{Q}_0\mathcal{Q}_0\mathcal{Q}_\pi = -1$ The phase diagram of the Floquet Kitaev Hamiltonian is shown in Fig. 3.3b.

3.2.3 Floquet Fermi's golden rule

In this section, we want to derive the Floquet equivalent to Fermi's golden rule following Ref. [119]. Using Floquet Fermi's golden rule, we can investigate heating effects in a Floquet system in the presence of interactions. This tool becomes important for the discussion of the Floquet Majorana box qubit in Chap. 4. Let us consider a Hamiltonian $H(t) = H_0(t) + V$ with a non-interacting part $H_0(t)$ and a small interaction V. $H_0(t)$ consists of a static part and a time-periodic single particle coupling term that is strong and must be treated in a non-perturbative way. The strategy of deriving a transition rate between Floquet states is the following. First, we write the time evolution operator of H_0 in terms of the Floquet eigenbasis. In the interaction picture, we expand the time evolution up to first order in the interaction such that we obtain the overlap $A(i \to f, t)$ of an initial state $|\psi_i(0)\rangle$ at time $t_0 = 0$ with a final state $|\psi_f(t)\rangle$ at time t. Then we calculate the transition rate $\gamma_{i\to f} = \lim_{t\to\infty} \frac{P(i\to f,t)}{t}$ with the transition probability $P(i \to f, t) = |A(i \to f, t)|^2$.

The time evolution operator $U_0(t,t')$ associated with $H_0(t)$ is defined as

$$|\psi(t')\rangle = U_0(t',t)\,|\psi(t)\rangle\,. \tag{3.25}$$

Since $H_0(t)$ is time-periodic, we can use the spectral representation of the time evolution operator in terms of its Floquet eigenbasis,

$$\begin{aligned} U_0(t,t') &= \sum_\alpha e^{-i\epsilon_\alpha(t'-t)}\,|\Phi_{0,\alpha}(t')\rangle\,\langle\Phi_{0,\alpha}(t)| && (3.26)\\ &= \sum_{\alpha,n,m} e^{-i\epsilon_\alpha(t'-t)}e^{-i(n\omega t - m\omega t')}\,|\phi^m_{0,\alpha}(t')\rangle\,\langle\phi^n_{0,\alpha}(t)|\,, && (3.27)\end{aligned}$$

where α runs only over states in one Floquet zone $\epsilon_{min} \leq \epsilon_\alpha < \epsilon_{min} + \omega$. At equal times, the Floquet eigenstates $|\Phi_{0,\alpha}(t)\rangle$ form a complete set of the single-particle Hamiltonian $H_0(t)$ Hilbert space.

To account for the interaction V, we switch to the interaction picture via

$$\left|\psi^I(t)\right\rangle = U_0(t,t_0)\psi(t_0) \tag{3.28}$$

The wave function $\left|\psi^I(t)\right\rangle$ satisfies the modified Schrödinger equation

$$i\hbar\partial_t \left|\psi^I(t)\right\rangle = V^I(t) \left|\psi^I(t)\right\rangle, \tag{3.29}$$

where the interaction becomes $V^I(t) = U_0^\dagger(t, t_0) V U_0(t_0, t)$. The corresponding time evolution operator $U^I(t, t_0)$ then satisfies the differential equation

$$i\hbar\partial_t U_I(t, t_0) = V^I U_I(t, t_0). \tag{3.30}$$

With the initial condition $U_I(t_0, t_0) = \mathbb{1}$, the equation can be transformed into an integral equation

$$\begin{aligned} U_I(t, t_0) &= \mathbb{1} - \frac{i}{\hbar}\int_{t_0}^{t} dt' V^I(t') U_I(t_0, t') \\ &\approx \mathbb{1} - \frac{i}{\hbar}\int_{t_0}^{t} dt' V^I(t') + \mathcal{O}(V^2), \end{aligned} \tag{3.31}$$

where we approximated the iterative solution of the equation up to first order.

To calculate the scattering amplitude in the presence of an interaction V, we assume that V is switched on at $t = 0$. Furthermore, the initial state $|\psi_i(t=0)\rangle = |\Phi_{0,i}(t=0)\rangle$ is prepared at $t = 0$ and the final state $\left|\psi_f(t)\right\rangle = e^{-i\epsilon_\alpha t}\left|\Phi_{0,\alpha}(t)\right\rangle$ is a Floquet eigenstate of the Hamiltonian $H_0(t)$ at all times. We calculate the scattering amplitude as the overlap of the time evolved state, $U(t, 0)\left|\psi_i(t=0)\right\rangle$, with the final state, $\left\langle\psi_f(t)\right|$,

$$\begin{aligned} A(i \to f, t) &= \left\langle\psi_f(t)\right| U(t, 0) \left|\psi_i(0)\right\rangle \\ &= \left\langle\psi_f(t)\right| U_0(t, 0) U_I(t, 0) \left|\psi_i(0)\right\rangle \\ &= \left\langle\psi_f(0)\right| U_I(0, t) \left|\psi_i(0)\right\rangle, \end{aligned} \tag{3.32}$$

where $|\psi(0)\rangle$ is again in the Schrödinger picture and we applied the time-evolution operator corresponding to H_0 to the final state and evolved it back in time. For the case $i \neq f$, we rewrite the interaction as $V^I(t') = U_0(0, t') V U_0(t', 0)$ and obtain

$$\begin{aligned} A(i \to f, t) &= \left\langle\psi_f(0)\right| U_I(0, t) \left|\psi_i(0)\right\rangle \\ &\approx -\frac{i}{\hbar}\left\langle\psi_f(0)\right| \int_0^t dt' V^I(t') \left|\psi_i(0)\right\rangle \\ &= -\frac{i}{\hbar}\int_0^t dt' \left\langle\psi_f(0)\right| U_0(0, t') V U_0(t', 0) \left|\psi_i(0)\right\rangle \\ &= -\frac{i}{\hbar}\int_0^t dt' e^{-i(\epsilon_i - \epsilon_f)t'/\hbar} \left\langle\Phi_f(t')\right| V \left|\Phi_i(t')\right\rangle, \end{aligned} \tag{3.33}$$

where we used the assumption that the initial and final states are both Floquet eigenstates of H_0 with quasi-energy ϵ_i and ϵ_f. Finally, we can expand the states in the Fourier decomposition and perform the integral

$$\begin{aligned} A &= -\frac{i}{\hbar}\sum_{n,m}\int_0^t dt' e^{-i(\epsilon_i-\epsilon_f-(n-m)\hbar\omega)t'/\hbar}\left\langle \phi_f^m \right| V \left|\phi_i^n\right\rangle \\ &= \sum_{n,m}\frac{e^{-i(\epsilon_i-\epsilon_f-(n-m)\hbar\omega)t/\hbar}-1}{\epsilon_i-\epsilon_f-(n-m)\hbar\omega}\left\langle \phi_f^m \right| V \left|\phi_i^n\right\rangle \\ &= \sum_{l,m}\frac{e^{-i(\epsilon_i-\epsilon_f-m\hbar\omega)t/\hbar}-1}{\epsilon_i-\epsilon_f-m\hbar\omega}\left\langle \phi_f^l \right| V \left|\phi_i^{l+m}\right\rangle, \end{aligned} \tag{3.34}$$

where the frequency shift is transferred to the Fourier component of the initial state in the last line. Fermi's golden rule is obtained by calculating the rate $\gamma_{i\to f} = \lim_{t\to\infty}\frac{P(i\to f,t)}{t}$ with the transition probability $P(i\to f,t) = |A(i\to f,t)|^2$

$$\gamma_{i\to f} = \sum_{l,m,n}\frac{2\pi}{\hbar}\delta(\epsilon_i-\epsilon_f-m\hbar\omega)\left\langle \phi_f^l \right| V \left|\phi_i^{l+m}\right\rangle \left\langle \phi_f^{n+m} \right| V \left|\phi_i^n\right\rangle. \tag{3.35}$$

The Floquet Fermi's golden rule Eq. (3.35) is very similar to the usual Fermi's golden rule, but we have an additional summation over m. In a Floquet system, quasi-energy is only conserved up to multiples m of the driving frequency. Due to quasi-energy conservation, transitions occur if different Floquet modes are coupled by the interaction V, i.e., if $\left\langle \phi_f^l \right| V \left|\phi_i^{l+m}\right\rangle \neq 0$ and $\left\langle \phi_f^{n+m} \right| V \left|\phi_i^n\right\rangle \neq 0$.

3.3 Linear response theory

Linear response theory describes the response of a system to small perturbations. For example, we can use it to describe the weak coupling limit in Chap. 5. It turns out that the fluctuations due to a small non-equilibrium perturbation are still governed mainly by the equilibrium dynamics of the system. In this section, we want to derive the fluctuation-dissipation theorem [132–135]. This theorem relates the imaginary part of the (retarded) response function $\chi''(\omega)$ in the frequency domain and the auto-correlation function $\langle \hat{A}(t)\hat{A}(0)\rangle$ of the observable of interest. Here $\chi''(\omega)$ is a measure of dissipation of the system, and the auto-correlation function describes fluctuations of the observable A. Let's consider a Hamiltonian $H(t)$ with a static part H_0 and a small perturbation $V(t) = \theta(t-t_0)f(t)\hat{A}$, which is switched on at time t_0

$$H(t) = H_0 + \theta(t-t_0)f(t)\hat{A}. \tag{3.36}$$

The parameter $f(t)$ is small such that we can expand the time evolution operator in the interaction picture up to the first order (as in Eq. (3.31)). Therefore, the time-dependent expectation value of $\hat{A}$ in the presence of the perturbation is given as

$$\begin{aligned}\langle \hat{A}(t)\rangle &= \langle \hat{A}_I(t)\rangle + i\int_{t_0}^{t} \mathrm{d}t' f(t')\langle[\hat{A}_I(t),\hat{A}_I(t')]\rangle \\ &= \langle \hat{A}_I(t)\rangle + \int_{-\infty}^{t} \mathrm{d}t' f(t')\chi(t-t'),\end{aligned} \tag{3.37}$$

where the time-dependence of the operator $\hat{A}_I(t) = U^\dagger(t,t_0)\hat{A}U_0(t,t_0)$ in the interaction picture comes only from the time evolution $U_0(t) = e^{-iH_0 t}$ of the stationary Hamiltonian. Eq. (3.37) shows that the observable A responds linearly to the perturbation $f(t)$ with the response function $\chi(t-t')$. The Kubo formula captures this linear response

$$\chi(t-t') = i\theta(t-t_0)\langle[\hat{A}_I(t),\hat{A}_I(t')],\tag{3.38}$$

where $\theta(t-t')$ is the Heaviside function and signals that the perturbation is switched on at t_0. To derive the fluctuation-dissipation theorem, we want to calculate the imaginary part of χ

$$\chi''(\omega) = \frac{\chi(\omega)-\chi^*(\omega)}{2i}.$$

The imaginary part of the Fourier-transformed response function $\chi''(\omega)$ can be represented by the auto-correlation function $\langle\hat{A}(t)\hat{A}(0)\rangle$ using

$$\begin{aligned}\mathrm{Im}(\chi(\omega)) &= \frac{1}{2}\int_{-\infty}^{\infty}\langle\hat{A}(t)\hat{A}(0)-\hat{A}(0)\hat{A}(t)\rangle e^{i\omega t}\mathrm{d}t \\ &= \frac{1}{2}\int_{-\infty}^{\infty}\langle\hat{A}(t)\hat{A}(0)-\hat{A}(t-i\beta)\hat{A}(0)\rangle e^{i\omega t}\mathrm{d}t,\end{aligned}\tag{3.39}$$

where the cyclic property of the trace was used. By a substitution $t' = t - i\beta$, Eq.(3.39) can be further simplified

$$\begin{aligned}\mathrm{Im}(\chi(\omega)) &= (1-e^{-\beta\omega})\int_{-\infty}^{\infty}\langle\hat{A}(t)\hat{A}(0)\rangle \\ &= (1+n_B(\omega))^{-1}\int_{-\infty}^{\infty}\langle\hat{A}(t)\hat{A}(0)\rangle,\end{aligned}\tag{3.40}$$

where $n_B(\omega) = (e^{\beta\omega}-1)^{-1}$ is the Bose function. Thus, we arrive at the fluctuation-dissipation theorem

$$\int \mathrm{d}t\langle\hat{A}(t)\hat{A}(0)\rangle e^{i\omega t} = (1+n_B(\omega))\,\mathrm{Im}(\chi(\omega)).\tag{3.41}$$

Here, the fluctuations $\langle \hat{A}(t)\hat{A}(0)\rangle$ are related to the dissipative part of the response function, namely the imaginary part. Quantum fluctuations are an important noise source in nano-scale and biological systems since the tunneling and transport of electrons and other (quasi-) particles is assisted by this quantum effect at low temperatures [134]. At higher temperatures, there exists a cross-over to the classical fluctuation-dissipation theorem.

3.4 Open quantum systems

Recommended additional literature for this section

1. Book on *quantum computation and quantum information* by M. A. Nielsen and I. L. Chuang, particularly, Chap. 2.2 on *measurements* and Chap. 8 on *quantum noise and quantum operations* [23]
2. Lecture notes on *quantum information*, particularly, Chap. 3 by J. Preskill [136]
3. Lecture by M. D. Lukin, notes written by L. Childress, particularly, the section on *stochastic wave functions* [137]
4. Chapter on *Von Neumann's theory of quantum measurements* by J. Bub [137]

Until now, we have mainly considered closed quantum systems, i.e., systems that do not interact with an environment. This very idealized setup is conducive to predicting a system's qualitative behavior. However, we can never observe a truly closed quantum system in experiments. The quantum system will constantly interact with the environment, for example, via the measurement apparatus [23].

In the following, we briefly discuss three examples where the openness of the system becomes crucial. First, let us mention Floquet systems since they have been the main target of this chapter so far. In driven systems, time-translational invariance is broken, and energy is not conserved. As we learned in Sec. 3.1, only quasi-energy is conserved. While non-interacting, free fermion models host stable Floquet phases, they generally heat up to infinite temperatures in an experimental setup due to the interaction with the environment [109].

Secondly, any quantum system coupled to a thermal bath can be described as an open quantum system where the thermal bath acts as the environment. In Sec. 2.3.3, we discuss a class of algorithms that mimic a bath. In the quantum simulation, the quantum system is coupled to a low-entropy bath to approach the system's ground state. The finite-size bath is measured and reset so entropy and energy can be extracted, and the algorithm can be repeated until convergence. We

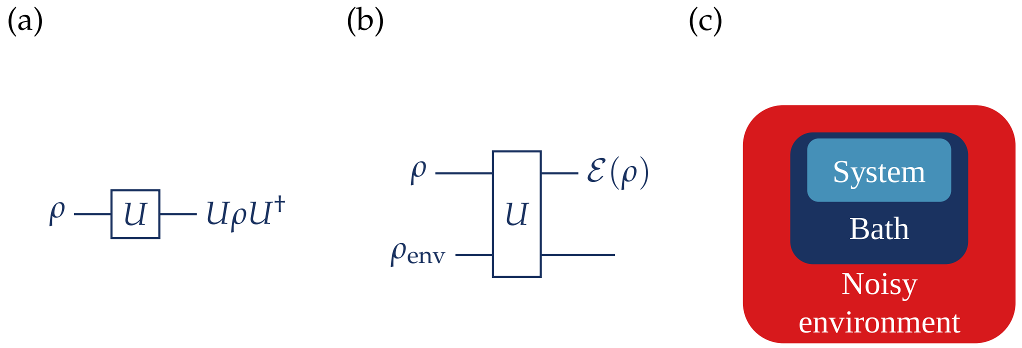

FIGURE 3.4: Open and closed quantum systems: (a) A closed quantum system can be described by unitary evolution alone. (b) A quantum channel $\mathcal{E}$ captures the effect of the environment during the evolution of an open system. (c) When simulating a system coupled to a bath on a noisy quantum device, the system alone can be treated as an open system. The system and the bath can be treated as a closed system by fully tracking the composite system. The closed "system-bath" system becomes open in a noisy environment. Panel (a) and (b) are inspired form Ref. [23].

can describe the evolution of the system in the presence of the bath in terms of an open quantum system. Both system and bath together again form a closed system, see Fig. 3.4.

Finally, the simulation of the system and the bath on current noisy quantum devices means the two are exposed to an *external* environment, see Fig. 3.4. However, we don't have as much control over this external environment as over the simulated bath. The effect of the environment is usually platform dependent and can only be approximated. Often, qubit fidelities change daily, if not from hour to hour, and exact noise models are challenging to find. Still, we can find a good qualitative description of the noise using the language of open quantum systems [23].

This section aims to give a conceptual introduction to the work on simulated cooling, see Chap. 5. First, we discuss the fundamental postulate of quantum mechanics - measurements. We are particularly interested to see how a measurement of the bath influences the system.

In the second part, we describe the noise in a quantum computing device as a quantum channel. Quantum channels are linear maps of density matrices and provide a good toolbox for the description of open quantum systems. Assuming that the noise is Markovian, we show that a Master equation can model the evolution of the system. While density matrices are the prime object in open quantum systems, increasing memory cost compared to wave functions makes it more difficult to simulate them numerically. Therefore, we introduce the stochastic Schrödinger equation to solve this equation on the wave function level. The stochastic Schrödinger equation is the basis of the numerical calculations of Chap. 5.

3.4.1 Quantum measurements

The postulate of measurement is fundamental for quantum mechanics. Only through measurements one can observe quantum phenomena. Like the other postulates, measurement can be well described by our mathematical toolbox, but the interpretation is not always trivial. Measurements open closed quantum systems as the unitarily evolving closed quantum system interacts with the observant environment (usually the experimentalist) through the measurement.

Generally, a quantum measurement is characterized by a set of Hermitian measurement operators M_m with the possible measurement outcomes m. The measurement operators act on the Hilbert space of the observed system. Right before the measurement, the probability of the measurement outcome is given by

$$p(m) = \langle\psi| M_m^\dagger M_m |\psi\rangle , \tag{3.42}$$

where $|\psi\rangle$ is the system's wave function immediately before the measurement [23]. With the probability $p(m)$, the wave function after the measurement is given as

$$\frac{M_m |\psi\rangle}{\sqrt{\langle\psi| M_m^\dagger M_m |\psi\rangle}}, \tag{3.43}$$

where the measurement operator M_m is applied to the wave function, and the denominator ensures the normalization of the wave function. The measurement operators M_m are not necessarily projection operators but obey the completeness equation

$$\sum_m M_m^\dagger M_m = \mathbb{I}. \tag{3.44}$$

Eq. (3.44) ensures that the probability of all measurement outcomes sum to one

$$1 = \sum_m p(m) = \sum_m \langle\psi| M_m^\dagger M_m |\psi\rangle .$$

In the following, we elaborate on the measurement postulate from the strong and the weak measurement perspective. Strong measurements are described by projective measurements. Projective measurements form a special case of the general measurement postulate. However, by combining projective measurements with unitary evolution, one arrives at a description which is equivalent to the general measurment postulate [23]. Projective measurements project a state $|\psi\rangle$ onto the eigenspace of an observable. Thus, they are described by projection operators in contrast to the general measurement operators from above. After the measurement, the wave function has collapsed, and repeated measurements of the same observable yield always the same result.

On the other hand, weak measurements (approximately) don't change the state during the measurement process in the limit where the coupling strength between the system and the measurement device goes to zero. Instead, the measurement device is shifted by an expectation value of the system observable [138, 139]. In experiments, this limit seems unreachable. However, the weaker the measurement, the less information is extracted and the more protected the wave function of the system. By cleverly designing a weak measurement, we can gain information of interest while preserving the quantum nature of the system.

Projective measurements

Projective measurement is described by an observable A [23]. The observable is a Hermitian operator with eigenvalues a and a spectral decomposition

$$A = \sum_a a P_a. \tag{3.45}$$

An eigenvalue a is measured with a probability $p(a) = \langle\psi| P_a |\psi\rangle$, where $|\psi\rangle$ is the wave function right before the measurement. After the measurement the wave function has collapsed and is projected to

$$\frac{P_a |\psi\rangle}{\sqrt{p(a)}},$$

where P_a is the projector into the sub-space of the observable with eigenvalue a. We use this definition of projective measurement combined with unitary evolution to describe a measurement on a system using a measurement device. Our example measurement protocol is known as *von Neumann measurements*. Ref. [140] serves as a good review.

We aim to measure an observable A of the system S. The measurement is carried out by the measurement device M. The quantum system S undergoes two processes during the measurement. It evolves directly due to the projective measurement, and it undergoes unitary time evolution $|\psi\rangle = U(t) |\psi\rangle$.

If we want to measure, we need to couple the system and measurement device. The total Hilbert space is formed by the tensor product $\mathcal{H}_s \otimes \mathcal{H}_M$. The interaction Hamiltonian couples the observable A to the measurement pointer V, where V could be, e.g., the momentum operator with $[\hat{x}, V] = i$. We assume that the interaction Hamiltonian is given by

$$H_{\text{int}} = g(t) A \otimes V, \tag{3.46}$$

where the coupling strength $g \gg 1$ for the measurement duration $0 \leq t \leq T$ and 0 otherwise. Since the Hamiltonian is non-interacting before $t = 0$ and during the measurement $g \gg 1$, the interaction governs the dynamics, and we can approximate the total Hamiltonian during the measurement as

$$H_{\text{tot}} = H_{\text{int}} \,. \tag{3.47}$$

Thus, the combined system must obey the Schrödinger equation

$$i\partial_t \left|\psi(t)\right\rangle = H_{\text{int}} \left|\psi(t)\right\rangle = g(t) A \otimes V \left|\psi(t)\right\rangle, \tag{3.48}$$

which can be formally solved by the ansatz $\left|\psi(t)\right\rangle = e^{\int_0^t -ig(t')A\otimes V \mathrm{d}t'}$ [140]. We assume a constant coupling $g(t) = g$ during the interaction to simplify the problem. Furthermore, we assume that the system and the pointer are in a product state $\left|\psi(0)\right\rangle = \left|\psi_0^S\right\rangle \otimes \left|\psi_0^V\right\rangle$ before the measurement and the measurement does not change the state of the pointer $\left|\psi_0^V\right\rangle$. Therefore, the combined wave function after the measurement duration T is given as

$$\left|\psi(T)\right\rangle = e^{-igTA\otimes V} \frac{P_a \left|\psi_0^S\right\rangle}{\sqrt{p(a)}} \otimes \left|\psi_0^V\right\rangle = e^{-igTaV} \left|a\right\rangle \otimes \left|\psi_0^V\right\rangle, \tag{3.49}$$

where we used that the system collapsed to the state $\left|a\right\rangle$ of the observable A with the eigenvalue a [140]. If x is the position of the pointer and $V = -i\partial_x$ is the momentum operator, the position of the measurement device $\left|\psi_0^V(x)\right\rangle$ is shifted by gTa

$$\left|\psi(T)\right\rangle = \left|a\right\rangle \otimes \left|\psi_0^V(x - gTa)\right\rangle. \tag{3.50}$$

If the measurement is repeated again, the measurement result will be the same since $\left|a\right\rangle = P_a \left|a\right\rangle$. The expectation value of the observable A can be estimated only by repeating the measurements on a newly prepared system. The repeated measurements require the preparation of the quantum state each time since it collapses after the measurement and $\left|a\right\rangle = P_a \left|a\right\rangle$.

In Chap. 5, we do repeated projected measurements of a bath. We probabilistically determine the measurement outcome a by a random number in the numerical implementation. Then, we collapse the bath qubits by setting the wave function to

$|a\rangle$ according to the outcome.

Weak measurements

In contrast to the projected measurement, during a weak measurement the system's state is approximately protected, i.e., it does not collapse. To achieve this protection, the coupling between the system and measurement device must be weak. Furthermore, the measurement is an adiabatic process, and the measurement time is long, in contrast to a strong short-timed interaction in the projective measurement scheme [138, 139].

As mentioned above, the interaction Hamiltonian is given by

$$H_{\text{int}} = g(t) A \otimes V, \tag{3.51}$$

where V describes the measurement device and A is an observable of the system. For our example, V denotes the momentum operator. The very slow measurement is implemented by taking $g(t) = 1/T$ for most of the time and very slowly switching the coupling on and off. In the adiabatic limit, the adiabatic theorem guarantees that the initial state is not excited to another eigenstate during the process. We approximate the infinitesimal shift of energy due to the interaction by first-order perturbation theory

$$\delta E = \langle H_{\text{int}} \rangle = \frac{\langle A \rangle V}{T}, \tag{3.52}$$

where $g(t) = 1/T$ for most of the time. Even though the system is not directly changed due to the measurement in this approximation, the time evolution of the system is affected by the energy shift δE and the wave functions is given by

$$\begin{aligned} |\psi(t)\rangle &= e^{-i(E_0^S + \delta E + E_0^V)T} \left|\psi_0^S\right\rangle \otimes \left|\psi_0^V(x)\right\rangle \\ &= e^{-i(E_0^S + E_0^V)T} e^{-i\langle A\rangle V} \left|\psi_0^S\right\rangle \otimes \left|\psi_0^V(x)\right\rangle \\ &= e^{-i(E_0^S + E_0^V)T} \left|\psi_0^S\right\rangle \otimes \left|\psi_0^V(x - \langle A\rangle)\right\rangle, \end{aligned} \tag{3.53}$$

where we used in the last line that the measurement device couples through its momentum to the system. Compared to the projective measurement scheme, the position of the pointer has shifted by the expectation value of the pointer. Note that the system is *not* collapsed but can, in theory, be used again and again for repeated measurements of different observables.

However, the long measurement time and small coupling strength put constraints on experiments that are not as easy to realize, and we refer the reader to the literature for a deeper discussion, e.g., Refs. [141–143] and references therein. For example, the *protective* measurement scheme was also proposed for qubits [144].

To illustrate the weak measurement, let us instead give an outlook to the quantum algorithm of Chap. 5 that mimics a system coupled to a bath. In that setup, we have two sets of qubits; one describes the system, the other the bath. While the algorithm details are discussed in Chap. 5, only the following is essential at this stage. The algorithm implements a cyclic protocol, where the system and bath qubits are weakly coupled for most of the time, and the coupling is adiabatically switched on and off. In the end, the bath qubits are projectively measured, as discussed above. The measurement disentangles the bath and the system. However, the measurement of the bath qubits acts like a weak measurement on the system. Therefore, we gain only little information on the system. On the other hand, the system's wave function is not collapsed, and we can use it again in the following protocol cycle. In Chap. 5, we show that the information is still enough to enhance the protocol's performance.

3.4.2 Quantum channels

For the description of open quantum systems, it is often convenient to use the language of density matrices, especially, if the exact state of the system is not known. We do not explicitly use the density matrix toolbox in the following chapters. However, using this detour, we derive the stochastic Schrödinger equation. Furthermore, we gain additional insights into (noisy) open quantum systems.

The general evolution of a density matrix $\rho \to \rho'$ can be described by a quantum channel $\mathcal{E}(\rho)$, see Fig. 3.4. A quantum channel is a linear map that preserves the trace and the positive-definiteness of ρ, and traces out the environment. A general quantum channel $\mathcal{E}$ has an operator-sum representation

$$\rho \to \mathcal{E}(\rho) = \sum_a M_a \rho M_a^\dagger, \tag{3.54}$$

where the Hermitian operators M_a satisfy the completeness equation $\sum_a M_a^\dagger M_a = \mathbb{I}$ [23, 136]. In this form, it becomes clear that a measurement is a quantum channel.

Let us exemplify the notion of a quantum channel on the later discussed cyclic protocol of Chap. 5. One step of the protocol includes the measurement and reset of the qubits. After the reset, the qubits are in the $|0\rangle$ state. We can model the measurement and reset by a feed-forward of the measurement result. We apply a spin flip operation only if the measurement outcome of the qubit is 1. For one qubit, the density matrix thus transforms like

$$\mathcal{E}(\rho) = P_0 \rho P_0 + X(1 - P_0)\rho(1 - P_0)X, \tag{3.55}$$

where the quantum channel is averaged over the two measurement outcomes $0, 1$, P_0 is the projector onto the $|0\rangle$ state, and X is the Pauli X operation.

If we assume that the system and the environment are initially in a product state, Eq. (3.54) can also be expressed as

$$\mathcal{E}(\rho) = \mathrm{tr}_{env}\left(U(\rho \otimes \rho_{env})U^{\dagger}\right), \tag{3.56}$$

where U describes the unitary evolution of the system and the environment together [23, 136]. Without any system and bath interaction, it is sufficient to just unitarily evolve the (closed) system alone as $\mathcal{E}(\rho) = \tilde{U}\rho\tilde{U}^{\dagger}$. Usually, a quantum system constantly interacts with the environment such that they build up correlations. But in experiments where a quantum state is newly prepared, one can assume that the system and the environment are approximately in a product state.

Often the form of the joint evolution is not known, and we have to approximate the effective evolution of the system due to the environment. In that case, we can imagine the environment as noise that disturbs the "*pure*" evolution of the system. The next section discusses how noise can be modeled as a quantum channel. We focus on depolarizing noise, which is a very general and frequently used noise model in quantum computing setups. Depolarizing noise is also implemented in Chap. 5, where we investigate the robustness of the quantum state preparation protocol in the presence of noise.

3.4.3 Noise as a quantum channel

Noise in a system due to the interaction with an environment can be described as a quantum channel. To make the (numerical or analytical) analysis of the noise approachable, one often assumes a simple noise model. For example, depolarizing noise is a very important and widely used model, particularly in the theory of fault tolerant quantum computation [145–149], as we discuss in the following.

For a single qubit, the depolarizing channel describes that with a probability p the system is replaced by a completely mixed state $\frac{\mathbb{I}}{2}$, while it stays unchanged otherwise

$$\mathcal{E}(\rho) = p\frac{\mathbb{I}}{2} + (1 - p)\rho, \tag{3.57}$$

see [23]. In Fig. 3.5, the effect of this noise channel is shown in the Bloch sphere representation $\rho(\boldsymbol{P}) = \frac{1}{2}(\mathbb{I} + \boldsymbol{P} \cdot \boldsymbol{\sigma})$, where $\boldsymbol{P}$ is the polarization of the spin qubit

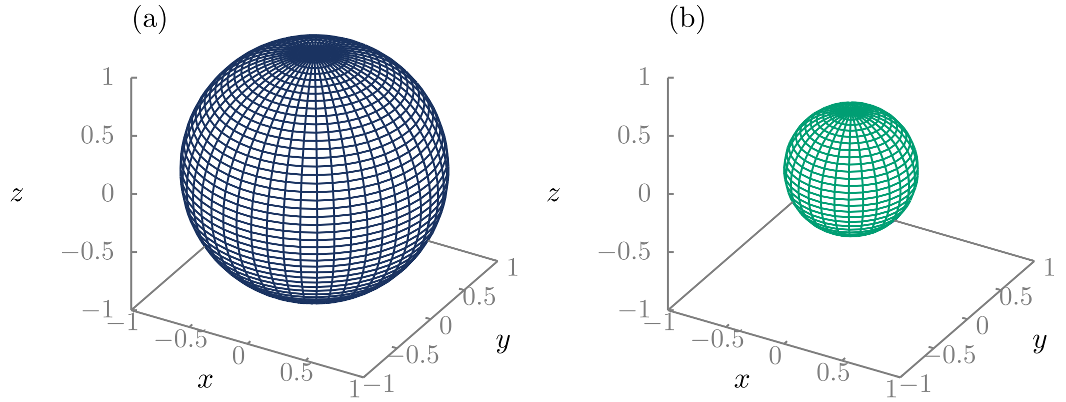

FIGURE 3.5: Effect of the depolarizing channel on the Bloch sphere: (a) Bloch sphere representation with a radius $|\boldsymbol{P}| = 1$, where $\boldsymbol{P}$ is the polarization vector. (b) The depolarizing channel, Eq. (3.57), with $p = 0.5$ shrinks the sphere uniformly and the radius decreases to $|\boldsymbol{P}'| = 0.5|\boldsymbol{P}|$.

and $\boldsymbol{\sigma_i}$ are the Pauli matrices. Due to the depolarizing noise, the length of the polarization $|\boldsymbol{P}'| = (1-p)|\boldsymbol{P}|$ decreases, and the Bloch sphere shrinks uniformly according to the probability p. To transform Eq. (3.57) into the operator sum representation form, we use that

$$2\mathbb{I} = \rho + X\rho X + Y\rho Y + Z\rho Z. \tag{3.58}$$

The quantum channel now has the form

$$\mathcal{E}(\rho) = (1 - \frac{3p}{4})\rho + \frac{p}{4}(\rho + X\rho X + Y\rho Y + Z\rho Z), \tag{3.59}$$

where with equal likelihood $p/4$ the Pauli X, Y and Z operations are applied to the system. In this representation, we see that this noise channel includes phase flip (Z), bit flip (X), and combined bit-phase flip (Y) errors. One can further realize that $\mathcal{E}(\mathbb{I}) = \mathbb{I}$. Thus, a totally mixed state stays completely mixed under the application of this noise channel. Note that this channel is a special case of the general Pauli-diagonal channel

$$\mathcal{E}_P(\rho) = \sum_{i=0}^{3} p_i \sigma_i \rho \sigma_i \tag{3.60}$$

with $\sigma_0 = \mathbb{I}$ [150]. The exact distribution of phase-flip, bit-flip, and phase-bit-flip errors strongly depends on the quantum computing platform and may strongly vary over time. To standardize the influence of the environment and simplify the problem, white noise $p_i = p$ is often assumed. However, this approach remains quite general as any quantum channel can be transformed at least into the Pauli-diagonal form in terms of depolarization without altering the diagonal elements [146].

In Eq. (3.59), the environment is already traced out, but, in principle, the errors are distinguishable by different states of the environment. Tracing out the environment means information is lost, and the channel is not reversible. In other words, coherence cannot be restored by a physical process. The irreversibility can be illustrated in the Bloch sphere representation, where decoherence leads to a contraction of the sphere. Inflation of the sphere increases $\boldsymbol{P}$ such that it can take values greater than one so that the density matrix would gain negative eigenvalues. Thus, such a map does not preserve the positivity of the density matrix and is unphysical and not a quantum channel. [136]

3.4.4 Lindblad Master equation

Quantum channels describe very generally the evolution of a system from a pure state to a mixed state. Thus, quantum channels also include decoherence, while unitary evolution describes only coherent processes. In this section, we enforce further assumptions on the system and the environment to obtain a differential equation similar to the Schrödinger equation for unitary dynamics, where $\rho(t+dt) = \rho(t) - idt[H, \rho(t)]$. This so-called Master equation can describe situations where the density matrix after an infinitesimal time step $\rho(t+dt)$ depends only on the density matrix $\rho(t)$. Thus, such a description requires that the evolution is local in time, i.e., Markovian.

For a general open system, this approximation is not valid because information can flow from the system to the environment and return at later times. Due to this memory effect, the density matrix of the system at time $t+dt$ is not determined solely by time t, but requires knowledge about earlier times as well. The dissipation leads to non-Markovian fluctuations connected to the fluctuation-dissipation theorem (see Sec. 3.3). Still, it is often possible to describe open systems in the Markovian approximation [136].

In the following, we derive the Master equation by starting from a general quantum channel $\mathcal{E}_{dt}$ that describes an infinitesimal time step

$$\rho(t+dt) = \mathcal{E}_{dt}(\rho(t)). \tag{3.61}$$

Then, we discuss how to more efficiently simulate this equation using wave functions instead of density matrices, see Sec. 3.4.5. Eq. (3.61) already imposes the strong assumption that the environment is reset to its initial state since the environment is traced out after each time step. Now we expand the quantum channel up to the first order in dt

$$\mathcal{E}_{dt} = \mathbb{I} + dt\mathcal{L}. \tag{3.62}$$

Inserting this expansion into Eq. (3.61), we can formally solve the equation as

$$\rho(t) = \lim_{n\to\infty} \left(1 + \frac{\mathcal{L}t}{n}\right)^n (\rho(0)) = e^{\mathcal{L}t}\left(\rho(0)\right), \tag{3.63}$$

if the so-called *Lindbladian* $\mathcal{L}$ is constant in time [136]. We can reformulate the quantum channel in the operator sum representation

$$\rho(t+dt) = \mathcal{E}_{dt}(\rho(t)) = \sum_a M_a \rho(t) M_a^\dagger = \rho(t) + \mathcal{O}(dt), \tag{3.64}$$

where the operators M_a must obey the completeness relation, and we are again only interested in terms linear in dt [136]. Without loss of generality, we can set the operators to

$$M_0 = \mathbb{I} + (-iH + K)dt \qquad \text{and} \qquad M_a = \sqrt{dt}L_a, \tag{3.65}$$

where the operator M_0 is linear in dt and the operators M_a for $a > 0$ scale with $\sqrt{dt}$. We can determine the operator K and write the evolution of the density matrix in form of a differential equation by using the completeness relation, Eq. (3.44). First, we insert the definitions, Eq. (3.65), into the completeness relation allowing only terms linear in dt

$$\mathbb{I} = \sum_a M_a^\dagger M_a = \mathbb{I} + dt(2K + \sum_{a>0} L_a^\dagger L_a) + \mathcal{O}(dt^2). \tag{3.66}$$

Thus, K must be set to

$$K = -\frac{1}{2}\sum_{a>0} L_a^\dagger L_a, \tag{3.67}$$

in order to ensure the completeness relation. With this definition, Eq. (3.64) leads to the Lindblad Master equation

$$\dot{\rho} = \mathcal{L}(\rho) = -i[H,\rho] + \sum_{a>0} L_a \rho L_a^\dagger - \frac{1}{2}\{L_a^\dagger L_a, \rho\}, \tag{3.68}$$

where the operators L_a describe possible transitions of the system by interactions with the environment, and the last term ensures normalization [136]. In this form, we can identify H as the Hamiltonian of the system that describes the unitary evolution and the L_a lead to decoherence. For example, for depolarizing noise, the *jump* operators can be identified with $L_a = \sigma_a$ that occur with probability p.

This Master equation is an excellent tool for analyzing the time evolution of an open quantum system [136]. However, for large (spin) systems, numerically implementing the solution in terms of wave functions is often favorable. Reducing the $d \times d$ dimensional matrix to a d vector allows a more efficient system simulation. The reformulation of the Master equation in terms of stochastic wave functions is called the stochastic Schrödinger equation and is the subject of the next section.

3.4.5 Stochastic Schrödinger equation

Instead of tracking the evolution of the density matrix by solving the Master equation, we now sample trajectories of pure states [136, 137]. However, averaging over many trajectories reproduces the density matrix evolution. Thus, we can simulate the same evolution by considering d dimensional vectors only. The environment is left unobserved in the Master equation, Eq. (3.68). To track the wave function, we now have to monitor the effect of the environment on the system, i.e., we need to detect the quantum jumps of the system that occur due to the environment. A jump occurs with a probability of

$$\text{prob}(a) = dt \left\langle \psi(t) \right| L_a^\dagger L_a \left| \psi(t) \right\rangle . \tag{3.69}$$

If we detect a jump, then we need to update the wave function according to

$$\left| \psi(t+dt) \right\rangle = \frac{L_a \left| \psi(t) \right\rangle}{\sqrt{prob(a)}}, \tag{3.70}$$

where L_a are the jump operators defined in the previous section. Otherwise, the wave function evolves as

$$\left| \psi(t+dt) \right\rangle = \frac{M_0 \left| \psi(t) \right\rangle}{|| M_0 \left| \psi(t) \right\rangle ||}, \tag{3.71}$$

where M_0 includes the evolution due to the system Hamiltonian and the additional term ensures the normalization as defined in Eq. (3.65). This formalism is known as the stochastic Schrödinger equation.

In Chapt. 5, we consider qubits under the evolution of a Hamiltonian H with additional depolarizing noise. The above stochastic wave function approach is slightly altered [136, 137]. First, we unitarily evolve the wave function as $e^{-iHt} \left| \psi \right\rangle$

using a second-order Suzuki-Trotter decomposition if no error is detected. As discussed in Sec. 3.1.3, the Suzuki-Trotter decomposition has the advantage that normalization is always ensured. The above description only considers terms up to the first order in dt. Furthermore, we set the probability that an error happens to a fixed value p. Every Pauli operation σ_i occurs with equal probability. Therefore, we don't have to calculate the error likelihood as Eq. (3.69).

The implemented algorithm includes the following steps:

1. Choose an initial state $|\psi_0\rangle$,
2. Evolve $|\psi_0\rangle$ by dt,
3. Draw a random number $r \in [0, 1]$,
4. If $r < p$, apply σ_i with equal probability,
5. Repeat steps 2-3 until the final time t_{final},
6. Repeat steps 1-4 N times to generate a sample of trajectories,
7. Average over the trajectories to obtain density matrix or expectation values of observables.

3.5 Summary

In this chapter, we have introduced three concepts to describe non-equilibrium systems. Floquet theory, see Sec. 3.1, elegantly describes periodically driven systems. Interestingly, Floquet systems can host topological phases that do not exist in equilibrium, for example, Floquet Majoranas. The Floquet concepts form the basis for the investigation of the Floquet Majorana box qubit in Chap. 4.

In linear response theory, see Sec. 3.3, the fluctuation-dissipation theorem describes how fluctuations of an observable are related to the dissipative part of the response function. We use this concept in the analytical derivation of the cooling rate in Chap. 5.

Furthermore, open quantum systems allow one to describe the evolution of a system coupled to an environment that is not fully characterized, see Sec. 3.4. For example, we use the stochastic wave function approach to numerically simulate a quantum algorithm on a noisy quantum computer in Chap. 5.

Chapter 4

Stability of Floquet Majorana Box Qubits

“Driving is a spectacular form of amnesia. Everything is to be discovered, everything to be obliterated.” — Jean Baudrillard

The previous chapters discuss the importance and underlying principles of quantum computing and the rich world of novel phases in non-equilibrium systems. In this chapter, we enhance the Majorana box qubit (see Sec. 2.2.5) by driving the system periodically. A one-dimensional topological periodically-driven superconductor can not only host Majorana zero modes at the edges but also Floquet Majoranas (see Sec. 3.2) [117, 129, 130, 151–153]. Floquet Majoranas are like the Majorana zero modes localized at the edges of the topological superconductor. However, the two topological modes are distinct in quasi-energy, so they don’t hybridize. Floquet Majoranas have a quasi-energy $\frac{\hbar\omega}{2} = \frac{\hbar\pi}{2T}$, where ω is the driving frequency and T the period of the drive. Using incommensurate frequencies, it is possible to engineer multiple Floquet Majoranas at distinct quasi-energies [154]. The quasi-energy can thereby serve as a second dimension. Therefore, braiding becomes possible using Floquet and zero modes even in one spatial dimension provided that the periodic drive is nearly perfect [118].

We investigate the Majorana box qubit with an applied AC gate voltage. The "Floquet Majorana box qubit" can encode three topological qubits using four Majorana zero modes and four Majorana π modes in a fixed electron number parity subspace. As a basis, two topological superconducting quantum wires, each proximity coupled to a bulk superconductor, build the usual Majorana box qubit (see Fig. 4.1). The bulk superconductors are coupled through Josephson junctions with energy E_J. In the so-called Coulomb blockade regime, the electron number parity can be fixed with a large charging energy E_c. Additionally, we capacitively couple the bulk superconductor with a periodically oscillating gate voltage. The periodic drive gives rise to two extra Floquet Majoranas in each quantum wire.

In a similar setting, Bomentara and Gong have shown that the Floquet corner modes of a second-order topological superconductor can be used to operate one and two-qubit Clifford gates in a topologically protected manner [155]. Clifford gates do not form a universal set of quantum gates. However, the set of Clifford gates is the maximum that can be achieved using Majorana quasi-particles.

Here, our goal is to investigate the consequences of interaction effects that unavoidably are present in the Coulomb blockade regime. First, we derive a low-energy theory of the Floquet Majorana box qubit and show that Floquet Majoranas indeed emerge. Then, we use perturbation theory to examine the stability of the setup against interactions. We find that the stability of the Floquet Majorana box qubit depends crucially on the preparation protocol.

This chapter has been previously published in Physical Review Letters [P131]. Achim Rosch and Erez Berg designed the study. Under the supervision of Achim Rosch, I derived the analytical results outlined in this chapter. In addition, I wrote the code and made the plots. The chapter follows closely the manuscript of reference [P131], which I have written with the help and revision of Achim Rosch, Erez Berg, and Jinhong Park. The plots are reproduced from the paper.

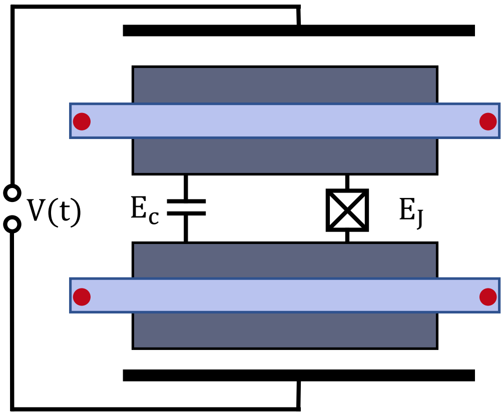

FIGURE 4.1: Schematic of the Floquet Majorana box qubit: A superconducting qubit formed by two Josephson coupled bulk superconductors (dark blue) with Josephson energy E_J. The system is in the Coulomb blockage regime with large charging energy E_c and capacitively driven with a voltage $V(\tau)$. Each bulk superconductor is proximity coupled to a topological superconducting nanowire (light blue).

4.1 Model

We describe the Floquet Majorana box qubit with a minimal model. The topological superconducting quantum wires are modeled as two Kitaev chains (see

Sec. 2.2.1), $\alpha = 1, 2$, which are each proximity coupled to a superconducting island

$$H = \frac{E_c}{2}\hat{Q}^2 - E_J \cos(\hat{\phi}) + \hat{Q}V(\tau) - \sum_{i,\alpha} \mu c^\dagger_{i,\alpha} c_{i,\alpha}$$
$$+ \sum_{i,\alpha} \left(-\frac{t}{2} c^\dagger_{i,\alpha} c_{i+1,\alpha} + \frac{\Delta}{2} e^{(-1)^\alpha i\hat{\phi}/2} c^\dagger_{i,\alpha} c^\dagger_{i+1,\alpha} + h.c. \right), \tag{4.1}$$

where $\hat{\phi} = \hat{\phi}_1 - \hat{\phi}_2$ is the phase difference between the two bulk superconductors and $\hat{Q} = \hat{Q}_1 - \hat{Q}_2$ is the difference between Cooper pairs. The setup describes a Majorana box qubit (see Sec. 2.2.5) with an additional oscillation voltage $V(\tau) = V_0 \cos(\omega\tau)$, where τ denotes the time in contrast to the nearest neighbor hopping t of the Kitaev chain. The chemical potential μ and the pairing Δ further characterize the Kitaev chain. The Josephson energy E_J describes Cooper pair tunneling from one superconducting island to the other with $[\hat{Q}, e^{\pm i\hat{\phi}/2}] = e^{\pm i\hat{\phi}/2}$. We only consider the charging energy of the charge imbalance as an interaction effect. The charging energy of the global charge $\hat{Q}_{tot} = \hat{Q}_1 + \hat{Q}_2$ is neglected because we assume conservation of the total charge. Further interaction effects between the superconducting islands and within the quantum wires are omitted. However, as we will argue later, our results generalize to the case of weak interactions.

4.2 Parameter regime

We assume that the driving frequency ω is of the order of the Kitaev chain parameters. This frequency regime is a necessary condition for the emergence of Floquet Majoranas. The energy scale of the bulk superconductors is separated from the quantum wires $\omega, \Delta, t, \mu \ll E_c \ll E_J, V_0$. We operate the qubit in the transmon (see Sec. 2.1.2) limit $E_c \ll E_J$ such that the relative charging between the superconducting island and the sensitivity to charge noise is exponentially suppressed [40, 59]. In the $E_c \ll E_J$ limit, charge fluctuations are high, but phase fluctuations are very low. Therefore we can approximate the bulk superconductors as a driven harmonic oscillator

$$H_{SC}(\tau) = \frac{E_c}{2}\hat{Q}^2 + \frac{E_J}{2}\hat{\phi}^2 + \hat{Q}V(\tau), \tag{4.2}$$

where we expand $\cos\hat{\phi} \approx 1 - \frac{\hat{\phi}^2}{2}$. We derive an effective low-energy Hamiltonian in the next section using this approximation.

4.3 Effective low-energy Hamiltonian

In this section, we derive an effective low-energy theory for the driven Kitaev chain. First, we start with the harmonic oscillator approximation (Eq.(4.2) introduced above. Then, we use the relations $e^{\pm i\alpha\hat{\phi}/2}|Q\rangle = |Q\pm\alpha\rangle$ and $e^{\pm i\alpha\hat{Q}/2}|\phi\rangle = |\phi\pm\alpha\rangle$ to shift the linear offset of the conjugate variables $\hat{Q}$ and $\hat{\phi}$. Since the offset α is time-dependent, it induces a time-dependence of the conjugate variable $i\partial_t U(t)$. The first unitary transformation $U_1(\tau) = e^{-i\hat{\phi}V(\tau)/(2E_c)}$ removes the linear term $\hat{Q}V(\tau)$ and induces a time-depend phase offset $\hat{\phi} \sim \partial_\tau Q/E_J$. We absorb the offset in $\hat{\phi}$ with a second transformation $U_2 = e^{-i\hat{Q}\partial_\tau V(\tau)/(4E_J E_c)}$. Using a Schrieffer-Wolff transformation $U_3 = e^{-i\hat{Q}\frac{\delta}{8E_J}T}$, we pertubatively remove transitions to excited states of H_{SC} triggered by $e^{\pm i\hat{\phi}/2}$ in Eq. (4.1). All approximations are well-justified for $\Delta \ll E_J$, $E_c \ll E_J$, and $V_0 \ll \frac{E_c E_J}{\omega}$.

Following this recipe step by step, we start with the harmonic oscillator approximation and, for convenience, only carry terms of the Hamiltonian that include $\hat{Q}$ or $\hat{\phi}$

$$\begin{aligned} H_0(\tau) &= \frac{E_c}{2}\hat{Q}^2 + \frac{E_J}{2}\hat{\phi}^2 + \hat{Q}V(\tau) + \frac{\Delta}{2}\left(\sum_i c_i^\dagger c_{i+1}^\dagger e^{-i\hat{\phi}/2} + h.c.\right) \\ &= \frac{E_c}{2}(\hat{Q} + \frac{V(\tau)}{E_c})^2 \frac{E_J}{2}\hat{\phi}^2 + \hat{Q}V(\tau) + \frac{\Delta}{2}\left(\sum_i c_i^\dagger c_{i+1}^\dagger e^{-i\hat{\phi}/2} + h.c.\right) + \text{const.}, \end{aligned} \tag{4.3}$$

where we disregard the total energy shift $-\frac{V(t)^2}{8E_c}$. We remove the offset in $\hat{Q}$ by the unitary transformation $U_1(\tau) = e^{-i\hat{\phi}V(\tau)/(2E_c)}$ and arrive at

$$\begin{aligned} H_1(\tau) &= U_1^\dagger(\tau)H_0(\tau)U_1(\tau) - iU_1^\dagger(\tau)\partial_\tau U_1(\tau) \\ &= \frac{E_c}{2}\hat{Q}^2 + \frac{E_J}{2}\hat{\phi}^2 + \frac{\Delta}{2}\left(\sum_i c_i^\dagger c_{i+1}^\dagger e^{-i\hat{\phi}/2} + h.c.\right) - \hat{\phi}\frac{\dot{V}(\tau)}{2E_c} + \text{const.}, \end{aligned} \tag{4.4}$$

where the time derivative of the unitary transformation implies a time-dependent displacement of $\hat{\phi}$. In the same spirit, we apply another unitary transformation $U_2(\tau) = e^{-i\hat{Q}\frac{\dot{V}(\tau)}{4E_c E_J}}$ to eliminate the $\hat{\phi}$ offset and obtain

$$\begin{aligned} H_2(\tau) &= U_2^\dagger(\tau)H_1(\tau)U_2(\tau) - iU_2^\dagger(\tau)\partial_\tau U_2(\tau) \\ &= \frac{E_c}{2}\hat{Q}^2 + \frac{E_J}{2}\hat{\phi}^2 + \frac{\Delta}{2}\left(\sum_i c_i^\dagger c_{i+1}^\dagger e^{-i(\hat{\phi}/2 + \frac{\dot{V}(\tau)}{2E_c E_J})} + h.c.\right) - \hat{Q}\frac{V''(\tau)}{4E_c E_J} + \text{const.}. \end{aligned} \tag{4.5}$$

Here, we further apply two approximations. We neglect the newly induced shift in $\hat{Q}$ since $\frac{V''(\tau)}{E_cE_J} \sim \frac{\omega^2 V_0}{E_cE_J} \ll \omega \ll E_c, E_J$. Furthermore, the phase is almost locked in the transmon regime $E_c \ll E_J$. Therefore, we can expand $e^{-i\hat{\phi}/2} \approx 1 - i\frac{\hat{\phi}}{2}$ and arrive at

$$H_3(\tau) = \frac{E_c}{2}\hat{Q}^2 + \frac{E_J}{2}\hat{\phi}^2 + \frac{\Delta}{2}\left(\sum_i c_i^\dagger c_{i+1}^\dagger e^{-i\frac{V(\dot{\tau})}{2E_cE_J}} + h.c.\right) - \frac{\Delta}{4}T\hat{\phi} + \text{const.} \tag{4.6}$$

with

$$T = i\left(e^{-i\frac{\dot{V}(\tau)}{2E_cE_J}}\sum_i c_i^\dagger c_{i+1}^\dagger - e^{i\frac{\dot{V}(\tau)}{2E_cE_J}}\sum_i c_{i+1}c_i\right). \tag{4.7}$$

Next, we want to absorb the shift in $\hat{\phi}$ with the unitary transformation $U_3 = e^{-i\hat{Q}\frac{\Delta}{8E_J}T}$. At this point, we need to include all terms of the Kitaev Hamiltonian in $\tilde{H}_3(\tau)$, since U_3 does not commute with the Kitaev Hamiltonian

$$H_k = \mu\sum_i c_i^\dagger c_i - \sum_i\left(\frac{t}{2}c_i^\dagger c_{i+1} + \frac{\Delta}{2}c_i^\dagger c_{i+1}^\dagger e^{-i\frac{\dot{V}(\tau)}{2E_cE_J}} + h.c.\right).$$

We use the Baker-Campbell-Hausdorf formula $e^{S/E_J}He^{-S/E_J} = H + \frac{1}{E_J}[S,H] + \mathcal{O}(\frac{1}{E_J^2})$ up to first order in $1/E_J$, where $U_3 = e^{-S/E_J}$ and obtain

$$\begin{aligned} H_4(\tau) &= U_3^\dagger(\tau)\tilde{H}_3(\tau)U_3(\tau) - iU_3^\dagger(\tau)\partial_\tau U_3(\tau) \\ &= \frac{E_c}{2}\hat{Q}^2 + \frac{E_J}{2}\hat{\phi}^2 + H_k - \frac{\Delta^2}{32E_J}T^2 + \frac{\Delta}{8E_J}[T,H_k]\hat{Q} + \mathcal{O}(\frac{1}{E_J^2}) + \text{const.}, \end{aligned} \tag{4.8}$$

where the T^2 term comes from the completion of the square $\frac{E_J}{2}\hat{\phi}^2 - \frac{\Delta}{4}T\hat{\phi} = \frac{E_J}{2}(\hat{\phi} - \frac{\Delta}{4E_J}T)^2 - \frac{\Delta^2}{32E_J}T^2$. We can further neglect the small displacement of $\hat{Q}$ of the order of $\frac{\Delta^2}{E_JE_c}$ which comes from the commutator $[T,H_k]$. Since the energy scales of the bulk superconductors and the Kitaev chains are separated with $\mu, t, \Delta \ll E_c, E_J$, we arrive at the time-dependent low-energy Hamiltonian

$$\begin{aligned} H_{\text{eff}}(\tau) &= -\sum_{i,\alpha}\mu c_{i,\alpha}^\dagger c_{i,\alpha} + \sum_{i,\alpha}\left(-\frac{t}{2}c_{i,\alpha}^\dagger c_{i+1,\alpha} + \frac{\Delta}{2}e^{-(-1)^\alpha i\frac{\dot{V}(\tau)}{2E_cE_J}}c_{i,\alpha}^\dagger c_{i+1,\alpha}^\dagger + h.c.\right) - \frac{\Delta^2}{32E_J}T^2, \\ T &= ie^{-i(-1)^\alpha\frac{\dot{V}(\tau)}{2E_cE_J}}\sum_{i,\alpha}c_{i,\alpha}^\dagger c_{i+1,\alpha}^\dagger + h.c. \end{aligned} \tag{4.9}$$

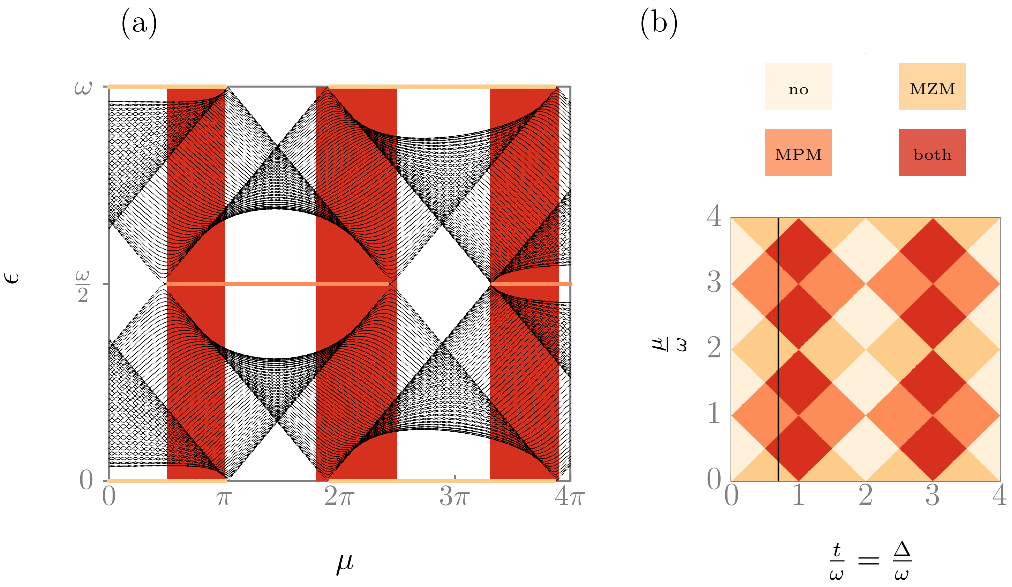

FIGURE 4.2: (a) Floquet spectrum as a function of the static chemical potential μ ($N = 60$, $\delta\mu = 3\pi$, $t = \pi$, $T = 1.4$, $N_{\text{steps}} = 100$, $\Delta = -\pi$). The Majorana zero mode (MZM, light orange) and the Majorana π modes (MPM, orange) can coexist, highlighted by the red-shaded areas. (b) Phase diagram of the driven Kitaev chain, as a function of $\frac{t}{\omega} = \frac{\Delta}{\omega}$ and $\frac{\mu}{\omega}$, shows the four different phases: trivial, only MZM, only MPM, and both modes.

4.4 Floquet spectrum

In this section, we will discuss the spectrum of the effective low-energy Hamiltonian neglecting the weak interaction effects. But the last term of Eq. (4.9) becomes essential when we discuss the stability of the box qubit in the presence of interactions. Without interaction effects, the two Kitaev chains are decoupled, and it is sufficient to investigate one chain separately. Then, the Hamiltonian has the form

$$H^0_{\text{eff}}(\tau) = -\sum_{i,\alpha} \mu c^\dagger_{i,\alpha} c_{i,\alpha} + \sum_{i,\alpha} \left(-\frac{t}{2} c^\dagger_{i,\alpha} c_{i+1,\alpha} + \frac{\Delta}{2} e^{-(-1)^\alpha i \frac{\dot{V}(\tau)}{2E_C E_J}} c^\dagger_{i,\alpha} c^\dagger_{i+1,\alpha} + h.c. \right), \tag{4.10}$$

where a gauge transformation can transfer the time-dependence of the phase to the chemical potential. Rewritten with a time-dependent chemical potential, we find the Floquet Hamiltonian familiar from Sec. 3.2.1

$$H^0_{\text{eff}} = \sum_{i,\alpha} - \left(\mu - (-1)^\alpha \delta\mu \cos(\omega\tau)\right) c^\dagger_{i,\alpha} c_{i,\alpha} - \frac{t}{2} c^\dagger_{i,\alpha} c_{i+1,\alpha} + \frac{\Delta}{2} c^\dagger_{i,\alpha} c^\dagger_{i+1,\alpha} + h.c. \tag{4.11}$$

with $\delta\mu = V_0 \frac{\omega^2}{E_c E_J}$ for an oscillating gate voltage, $V(\tau) = V_0 \cos(\omega\tau)$. The Floquet spectrum of Fig. 4.2a shows the characteristic features which have already been observed before [117, 118, 129]. Since the quasi-energy ϵ is only conserved modulo the driving frequency, we show only one Floquet zone $0 \leq \epsilon < \omega$. The spectrum shows a cut through the phase diagram of Fig. 4.2b, where the system can always host at least one topological mode. Importantly, in the red-shaded regions, the phase can host coexisting Majorana zero modes and Majorana π modes at quasi-energy $\pi/T = \omega/2$. The spectrum was numerically calculated using the Suzuki-Trotter decomposition of the Floquet time evolution operator. This method is discussed in more detail in the introduction chapter, Sec. 3.1.3. However, the Floquet matrix approach, mentioned in Sec. 3.1.2, leads to the same result. The phase diagram was obtained from the bulk topological invariant, introduced in Sec. 3.2 [117, 118].

4.5 Adiabatic preparation of the Floquet state

The spectrum alone is not able to fully characterize the Floquet system. To obtain the complete picture, one has to consider the evolution of the Floquet many-body state during the preparation process. We will first consider adiabatic state preparation. In this standard protocol, the undriven ground state of the Hamiltonian, Eq. (4.1) with $V_0 = 0$, is prepared first. Then, the amplitude of the drive V_0 is slowly increased. In the following, we discuss the consequences of the preparation by looking only at the bulk. But we have also numerically checked that the prediction holds in a finite-size system. The bulk calculation has the advantage of getting an intuitive understanding as the analysis reduces to a 2×2 matrix problem. This calculation is explained in the next section. But first, we want to discuss what is so special about a Floquet Bogoliubov Hamiltonian.

Without driving, we know that physical excitations above the ground state $a_k^\dagger |GS\rangle$ have a positive energy $E_k > 0$, where $a_k |GS\rangle = 0$. However, due to the doubling of the degrees of freedom, the Bogoliubov treatment of the Hamiltonian introduces artificial excitations with negative energies $E_k < 0$ using $E_k a_k^\dagger a_k = -E_k a_k a_k^\dagger$. The formally introduced negative energies are unphysical and only due to the formalism. Therefore, we call them ‘Bogoliubov shadows’. In equilibrium, we can distinguish the physical excitations from the Bogoliubov shadows by the sign of the energy. The situation dramatically changes once we consider a Floquet setup since quasi-energy is only defined modulo the driving frequency, and the notion of positive and negative energies doesn’t exist anymore.

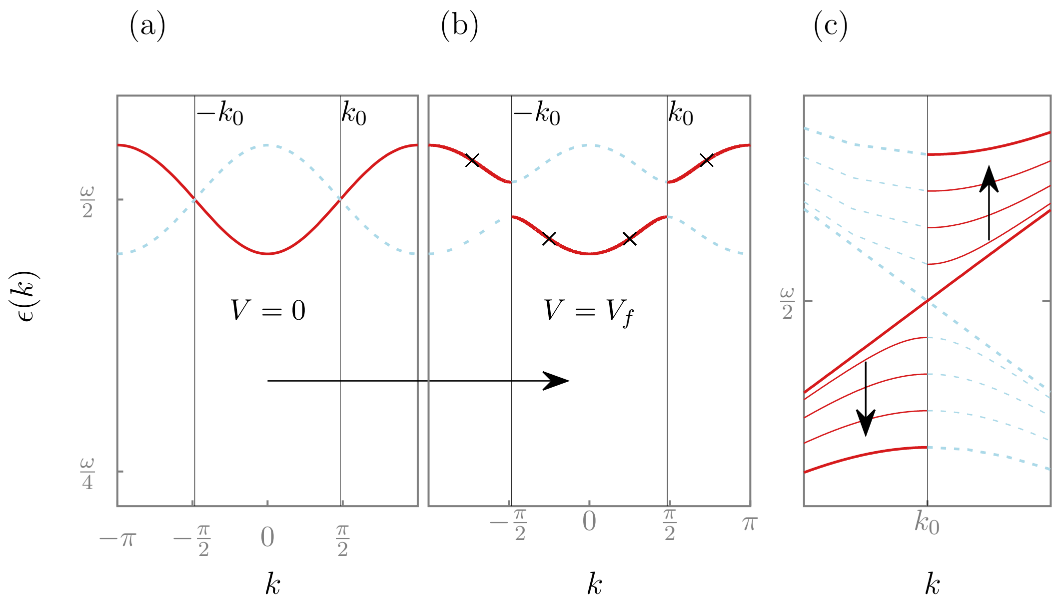

FIGURE 4.3: Bulk Floquet spectrum as a function of momentum k ($\mu = 0.1\pi$, $t = -\Delta = \pi$, $\omega = \pi$, $\delta\mu_f = 0.2$) prepared by adiabatically switching on the oscillating voltage V. (a) Quasi-energy of the physical excitation, $\tilde{a}_k^\dagger\,|\mathrm{GS}\rangle$ (solid red line) and their 'Bogoliubov shadow' (blue dashed line). (b) A band gap opens at energy $\omega/2$ in the driven system. (c) The quasi-energy of the physical excitations develops a discontinuity at $\pm k_0$ since the nature of the excitations remains the same under adiabatic evolution. As a result, the system is highly unstable as the resonant creation of four quasi-particles with total quasi-energy ω is always possible. The four crosses give an example of such a process.

In Fig. 4.3, we show the Bogoliubov spectrum without driving ($V_0 = 0$) projected onto the first Floquet zone $0 \leq \epsilon < \omega$. The red line denotes the physical excitations at E_k, whereas the dashed line shows the Bogoliubov shadows at $-E_k + \omega$. The two modes have a crossing at $\pm k_0$, where $E_k k_0 = -E_{k_0} + \omega$ and $E_{k_0} = \frac{\omega}{2}$. The modes hybridize once the oscillating voltage is switched on. The hybridization is necessary for the emergence of Floquet Majoranas at quasi-energy $\omega/2 = \pi/T$. The only possibility to distinguish the physical excitations from the Bogoliubov shadows is by tracking the excitations during the preparation process. Since we slowly switch on the oscillating voltage, we can use adiabatic continuity to follow the evolution of the excitations. While the explicit calculation is shown in the next section, one can graphically see how the physical excitations are adiabatically evolved in Fig. 4.3c. The tracking leads to physical excitations for $|k| < |k_0|$ ($|k| > |k_0|$) with an energy smaller (larger) than $\frac{\omega}{2}$, marked in red in Fig. 4.3b. At k_0, a singularity is observed; the nature of the excitation changes and the energy jumps. Equivalently, one can track the many-body wave function $\prod_k (u_k + v_k a_k^\dagger a_{-k}^\dagger)$ during the adiabatic evolution. The singularity appears in the amplitudes u_k and v_k again at k_0, where they exchange their roles.

4.6 Physical excitations and adiabatic continuity

In this section, we analytically underpin the results from the last section and Fig. 4.3. Thus, the goal is to analytically calculate the Floquet bulk spectrum for a single quantum wire and analytically track the nature of excitations. To analyze adiabatic evolution upon slowly switching on the oscillating voltage, it is sufficient to consider small amplitudes of the oscillating chemical potential.

We start with the static Hamiltonian that describes the bulk of a single Kitaev chain

$$H_{\text{BdG}} = \frac{1}{2}\sum_k (c_k^\dagger, c_{-k}) \begin{pmatrix} -(\mu + t\cos k) & -i\Delta \sin k \\ i\Delta \sin k & \mu + t\cos k \end{pmatrix} \begin{pmatrix} c_k \\ c_{-k}^\dagger \end{pmatrix}, \tag{4.12}$$

where the oscillating voltage is absent. The Hamiltonian can be diagonalized using a Bogoliubov transformation

$$H_{BdG} = \frac{1}{2}\sum_k (a_k^\dagger, a_{-k}) \begin{pmatrix} E_k & 0 \\ 0 & -E_k \end{pmatrix} \begin{pmatrix} a_k \\ a_{-k}^\dagger \end{pmatrix} = \sum_k E_k a_k^\dagger a_k, \tag{4.13}$$

where $E_k = \sqrt{(\mu + t\cos k)^2 + \Delta^2} > 0$ is the energy of the physical excitation $a_k^\dagger |0\rangle$. The ground state $|0\rangle$ is defined by the condition $a_k |0\rangle = 0$.

The oscillating gate voltage introduces a time-dependent chemical potential $V(\tau) = \delta\mu \cos(\omega\tau)$. We write the driving term in terms of the diagonal basis a_k of the static Hamiltonian

$$\begin{aligned} H_{\text{drive}}(\tau) &= -V(\tau) \sum_k c_k^\dagger c_k && (4.14) \\ &= \frac{1}{2} \sum_k \frac{V(\tau)}{E_k} \left(a_k^\dagger, a_{-k}\right) \begin{pmatrix} -\mu - t\cos k & i\Delta \sin k \\ -i\Delta \sin k & \mu + t \cos k \end{pmatrix} \begin{pmatrix} a_k \\ a_{-k}^\dagger \end{pmatrix}. \end{aligned}$$

We use the Floquet matrix approach introduced in Sec. 3.1.2 to treat the time-dependent term. First, we make an ansatz for the Floquet quasi-particle operators in the Heisenberg picture

$$\tilde{a}_k^\dagger(\tau) = \sum_{n=-N}^{N} u_{k,n}\, e^{i(E_k^{\text{FL}} + n\omega)\tau}\, a_k^\dagger + v_{k,n}\, e^{-i(E_k^{\text{FL}} + n\omega)\tau}\, a_{-k}, \tag{4.15}$$

where E_k^{FL} are the quasi-energies modulo the driving frequency ω. We restrict $0 \leq E_k^{\text{FL}} < \omega$ to the first Floquet zone and include N Floquet modes. The description is only exact in the limit $N \to \infty$. However, the sum converges quickly for small amplitudes $\delta\mu$, and small N is sufficient. The main difference to the usual Floquet ansatz discussed in the introduction chapter is that we have to include both annihilation and creation operators. The coefficients $u_{k,n}$ and $v_{k,n}$ are determined by two conditions. The new operators must obey the fermionic anti-commutation relations and follow the Heisenberg equation of motion. If we write the coefficients $u_{k,n}$ and $v_{k,n}$ in a vector w_k^{FL} of size $2(2N+1)$, we can derive a Floquet matrix equation $H^{\text{FL}} w_k^{\text{FL}} = E_k^{\text{FL}} w_k^{\text{FL}}$. The procedure is the same in the introduction chapter except that the Hilbert space has doubled due to the Bogoliubov formalism. However, the two conditions cannot uniquely define the coefficients since the particle-hole transformation relates creation and annihilation operators, and, thus, $v_{k,n}$ and $u_{k,n}$,

$$\tilde{a}_k^\dagger \longleftrightarrow \tilde{a}_{-k}, \qquad E_k^{\text{FL}} \longleftrightarrow -E_k^{\text{FL}} + \omega, \tag{4.16}$$

where we added ω to stay in the first Floquet zone. We can generalize the statement for systems without the $k \to -k$ symmetry. Then, a discrete Bogoliubov transformation maps $\tilde{a}_m^\dagger \leftrightarrow \tilde{a}_m$ and $E_m^{\text{FL}} \longleftrightarrow -E_m^{\text{FL}} + \omega$ for Floquet-Bogoliubov states with quantum number m. Again, we see that in the Floquet setup, we can only refer to the creation of quasi-particles with respect to initial conditions and the preparation process. The ambiguity of Eq. (4.16) is lifted if we define the annihilation operators such that they destroy the adiabatically prepared initial state

$|\psi_0\rangle$

$$\tilde{a}_k \, |\psi_0\rangle = 0.$$

We identify the quasi-particle operators for the adiabatic state preparation in the following. The oscillation amplitude $\delta\mu$ at a fixed frequency is slowly switched on. Using adiabatic continuity, the operators can be uniquely defined. For the static Hamiltonian, the physical excitations have positive energies $E_k > 0$, whereas the Bogoliubov shadows have negative energies $E_k < 0$. Adiabatic continuity states that a physical quasi-particle creation operator remains physical, and a Bogoliubov shadow stays a Bogoliubov shadow. We can therefore identify the nature of a Floquet Bogoliubov by tracing it back to the initial state at the beginning of the preparation. For small oscillations $\delta\mu \ll \omega, \Delta$, we can focus on quasi-resonant processes $E_k \approx -E_{k_0} = \omega$ and ignore higher order Floquet modes as they account for non-resonant processes. Thus, the $2(2N+1) \times 2(2N+1)$ Floquet matrix reduces to the 2×2 matrix

$$H_k^{\mathrm{FL}} = \begin{pmatrix} -E_k + \omega & \delta\mu \, f_k \\ \delta\mu \, f_k^* & E_k \end{pmatrix} \tag{4.17}$$

with $f_k = -i \frac{\Delta \sin k}{2\sqrt{(\mu + t\cos k)^2 + \Delta^2 \sin^2 k}}$. This matrix has the eigenvalues

$$\frac{\omega}{2} \pm \sqrt{(\delta\mu |f_k|)^2 + (E_k - \omega/2)^2}. \tag{4.18}$$

Each eigenvalue is associated with either physical excitations $\tilde{a}_k^\dagger \tilde{a}_k$ or Bogoliubov shadows $\tilde{a}_k \tilde{a}_k^\dagger$, depending on the protocol. For the adiabatic protocol, we demand that for vanishing $\delta\mu$ the initial operators are retrieved such that the physical operators have positive energy E_k

$$\lim_{\delta\mu \to 0} \frac{\omega}{2} \pm \sqrt{(\delta\mu |f_k|)^2 + (E_k - \omega/2)^2} = \frac{\omega}{2} \pm |E_k - \omega/2| \overset{!}{=} E_k. \tag{4.19}$$

Thus, the ± sign is determined by the nature of excitations: The $+$ sign ($-$ sign) is needed for $E_k > \omega/2$ ($E_k < \omega/2$) to obtain the physical excitation quasi-energies

$$E_k^{\mathrm{FL}} = \begin{cases} \frac{\omega}{2} + \sqrt{(\delta\mu |f_k|)^2 + (E_k - \omega/2)^2} & \text{for } E_k > \omega/2 \\ \frac{\omega}{2} - \sqrt{(\delta\mu |f_k|)^2 + (E_k - \omega/2)^2} & \text{for } E_k < \omega/2 \end{cases}. \tag{4.20}$$

Hence, we derived the analytical expression for the quasi-energy spectrum of Fig. 4.3 that explains the jump in the spectrum at k_0. Namely, it happens when $E_{k_0} - \omega/2$ changes sign.

4.7 Stability in the presence of interactions

To investigate the stability of the Floquet box qubit in the presence of interactions, we derive a Floquet Fermi golden rule. The detailed calculation is outlined in Sec. 4.7.1. For a general introduction, see Sec. 3.2.3. We first expand the interaction Hamiltonian, the last term of Eq.(4.9), in terms of the Floquet eigenmodes of the non-interacting Hamiltonian

$$\Delta H_{\text{int}} = \sum V^{m}_{\nu_1,\nu_2,\nu_3,\nu_4} e^{im\omega\tau} \tilde{a}^{\dagger}_{\nu_1} \tilde{a}^{\dagger}_{\nu_2} \tilde{a}^{\dagger}_{\nu_3} \tilde{a}^{\dagger}_{\nu_4}, \tag{4.21}$$

where $V^{m}_{\nu_1,\nu_2,\nu_3,\nu_4} \sim \Delta^2/E_J$ is defined in the next section (Sec. 4.7.1). For the translational invariant bulk system considered above $\nu = k$.

The Floquet Fermi golden rule can approximate the quasi-particles creation rate

$$\gamma_{qp} = 4\frac{2\pi}{\hbar} \sum_{\nu_i,m} \delta(E_{\nu_1} + E_{\nu_2} + E_{\nu_3} + E_{\nu_4} + m\omega) |V^{m}_{\nu_1\nu_2\nu_3\nu_4}|^2, \tag{4.22}$$

where E_{ν_i} are the quasi-energies of the non-interacting Floquet Hamiltonian. The factor 4 arises because four quasi-particles are created during each process. In Sec. 4.7.2, we show how to evaluate the creation rate numerically. However, applying the Floquet golden rule to the bulk energies that we derived in the last section, it becomes immediately apparent that quasi-energy conservation $E_{\nu_1} + E_{\nu_2} + E_{\nu_3} + E_{\nu_4} = m\omega$ is always fulfilled after the adiabatic state preparation. Due to the jump of the physical quasi-particle excitation energy, four quasi-particles can be resonantly created above and below $\omega/2$ such that sum of quasi-energy is a multiple of the driving frequency. Hence, the adiabatic state preparation protocol is inherently unstable. In fact, the creation rate has even a logarithmic divergence in the bulk because of the processes close to the discontinuity k_0. Furthermore, this instability is expected to affect general models hosting Floquet Majoranas since the hybridization of the Bogoliubov modes at $\omega/2$ is necessary for the emergence of Floquet Majoranas. After deriving the Floquet Fermi golden rule and discussing the numerical calculation of the quasi-particle creation rate, we introduce another preparation protocol that circumvents this instability. In the end, we discuss possible higher-order interaction effects and disorder.

4.7.1 Floquet Fermi's golden rule

This section aims to derive the Floquet Fermi golden rule formula [119, 156, 157] for the specific four-body interaction term of Eq. (4.9). A more general approach is outlined in the introductory chapter, Sec. 3.2.3, which closely follows reference [119]. We first express the creation and annihilation operators $c_i^\dagger$ and c_i in terms of the Floquet operators $\tilde{a}_\nu^\dagger$ and $\tilde{a}_\nu$. $\tilde{a}_\nu^\dagger \left|0\right\rangle = \left|\phi_\nu\right\rangle$ creates a Floquet single particle eigenstate of the non-interacting Hamiltonian with quasi-energy ϵ_ν. The initialization protocol defines the quasi-particle vacuum $\left|0\right\rangle$. Without referring to the preparation of the Floquet system, the Floquet operators are not uniquely determined as further discussed in Sec. 4.6. The Floquet eigenstates of a single Floquet zone form a complete basis set at equal times

$$\mathbb{1} = \sum_\nu \left|\phi_\nu(\tau)\right\rangle \left\langle\phi_\nu(\tau)\right| .$$

Using this identity, we can rewrite the fermionic operators in terms of the Floquet operators

$$c_j^\dagger \left|0\right\rangle = \sum_\nu \left|\phi_\nu(\tau)\right\rangle \left\langle\phi_\nu(\tau)|j\right\rangle = \sum_\nu \left\langle\phi_\nu(\tau)|j\right\rangle \tilde{a}_\nu^\dagger(\tau) \left|0\right\rangle \tag{4.23}$$

and $c_j^\dagger = \sum_\nu \bar{\phi}_\nu(t,j)\tilde{a}_\nu^\dagger(\tau)$ with $\bar{\phi}_\nu(t,j) = \left\langle\phi_\nu(\tau)|j\right\rangle$. Now we use the time-periodic nature of the Floquet eigenstates and expand them in the Floquet modes $\left|\phi_\nu(\tau)\right\rangle = \sum_n e^{-in\omega\tau} \left|\phi_\nu^n\right\rangle$.

Inserting the Floquet expansion in Eq. (4.23), we obtain the expression $\bar{\phi}_\nu^n(j) = \left\langle\phi_\nu^n|j\right\rangle$:

$$c_j^\dagger = \sum_\nu e^{in\omega\tau}\bar{\phi}_\nu^n(j)\tilde{a}_\nu^\dagger(\tau), \tag{4.24}$$

where $\bar{\phi}_\nu^n(j) = \left\langle\phi_\nu^n|j\right\rangle$ and $\tilde{a}_\nu^\dagger(\tau) = e^{i\epsilon_\nu\tau}\tilde{a}_\nu^\dagger$. Now we can write the transition amplitude of an initial state $\left|\psi_i\right\rangle$ at time $\tau = 0$ to a distinct final state $\left|\psi_f\right\rangle$ at time τ

$$\begin{aligned} A_{i\to f}(\tau) &= \left\langle\psi_f(\tau)\right| U(\tau,0) \left|\psi_i(\tau=0)\right\rangle \\ &\approx -i\int_0^\tau d\tau' \left\langle\psi_f(0)\right| U_0(0,\tau')\Delta H_{\text{int}} U_0(\tau',0) \left|\psi_i(0)\right\rangle , \end{aligned} \tag{4.25}$$

where U is the full time-evolution operator, U_0 the non-interacting time evolution operator, and we expand the full time-evolution operator up to first order in the interaction $\Delta H_{\text{int}} = \frac{\Delta^2}{32E_J}T^2$. Inserting ΔH_{int} in terms of the mode-expanded Floquet operators, we obtain

$$\begin{aligned}
A_{i\to f}(\tau) = & -\frac{i\Delta^2}{32E_J}\sum_{j,k}\sum_{n_1,n_2,n_3,n_4}\sum_{\nu_1,\nu_2,\nu_3,\nu_4}\int_0^\tau d\tau' e^{i(n_1+n_2+n_3+n_4)\omega\tau'} e^{i(\epsilon_{\nu_1}+\epsilon_{\nu_2}+\epsilon_{\nu_3}+\epsilon_{\nu_4})\tau'} \\
& \times \bar{\phi}^{n_1}_{\nu_1}(j)\bar{\phi}^{n_2}_{\nu_2}(j+1)\bar{\phi}^{n_3}_{\nu_3}(k)\bar{\phi}^{n_4}_{\nu_4}(k+1)\left\langle\psi_f(0)\right|\tilde{a}^\dagger_{\nu_1}\tilde{a}^\dagger_{\nu_2}\tilde{a}^\dagger_{\nu_3}\tilde{a}^\dagger_{\nu_4}\left|\psi_i(0)\right\rangle \\
= & \frac{\Delta^2}{32E_J}\sum_{j,k}\sum_{n_1,n_2,n_3,n_4}\sum_{\nu_1,\nu_2,\nu_3,\nu_4}\frac{e^{i((n_1+n_2+n_3+n_4)\omega+\epsilon_{\nu_1}+\epsilon_{\nu_2}+\epsilon_{\nu_3}+\epsilon_{\nu_4})\tau}-1}{(n_1+n_2+n_3+n_4)\omega+\epsilon_{\nu_1}+\epsilon_{\nu_2}+\epsilon_{\nu_3}+\epsilon_{\nu_4}} \\
& \times \bar{\phi}^{n_1}_{\nu_1}(j)\bar{\phi}^{n_2}_{\nu_2}(j+1)\bar{\phi}^{n_3}_{\nu_3}(k)\bar{\phi}^{n_4}_{\nu_4}(k+1)\left\langle\psi_f(0)\right|\tilde{a}^\dagger_{\nu_1}\tilde{a}^\dagger_{\nu_2}\tilde{a}^\dagger_{\nu_3}\tilde{a}^\dagger_{\nu_4}\left|\psi_i(0)\right\rangle, \qquad (4.26)
\end{aligned}$$

where we assume that $|\psi_i(0)\rangle$ is the adiabatically prepared quasi-particle vacuum. Therefore only four-particle creation terms contribute. The scattering is determined $\gamma_{i\to f} = \lim_{\tau\to\infty}\frac{P(i\to f,\tau)}{\tau}$ by the transition probability $P(i\to f,\tau) = |A_{i\to f}(\tau)|^2$. Finally, we obtain

$$\gamma_{i\to f} = \frac{2\pi}{\hbar}\sum_{\nu_1,\nu_2,\nu_3,\nu_4,n}\delta(\epsilon_{\nu_1}+\epsilon_{\nu_2}+\epsilon_{\nu_3}+\epsilon_{\nu_4}+n\omega)|V^n_{\nu_1\nu_2\nu_3\nu_4}|^2 \qquad (4.27)$$

with

$$V^n_{\nu_1\nu_2\nu_3\nu_4} = \frac{\Delta^2}{32E_J}\sum_{j,k}\sum_{n_1,n_2,n_3,n_4}\delta(n-(n_1+n_2+n_3+n_4))\bar{\phi}^{n_1}_{\nu_1}(j)\bar{\phi}^{n_2}_{\nu_2}(j+1)\bar{\phi}^{n_3}_{\nu_3}(k)\bar{\phi}^{n_4}_{\nu_4}(k+1).$$

The rate $\gamma_{i\to f}$ gives the rate that an initial state scatters to a final state. To count how many quasi-particles are created, we have to multiply the rate by four since every process creates four quasi-particles.

4.7.2 Numerical calculation of the quasi-particle creation rates

So far, we have analytically investigated the quasi-particle creation rate in the bulk. Here, we describe how the Floquet golden rule formula can be numerically evaluated for a finite-size system with a discrete spectrum. To account for spectral broadening, the δ-function is replaced by a box function of width ΔE. The spectral broadening captures finite-lifetime effects which are not included in the quasi-particle creation rate γ_{qp} of Eq (4.22). We numerically diagonalize the single-particle Floquet matrix to obtain the Floquet eigenstates and the corresponding matrix elements. In our calculation, we consider only 7 Floquet modes which are enough for convergence in the parameter range of interest. The phase space is calculated by setting all matrix elements to one, i.e., only counting how often the quasi-energy conservation is fulfilled.

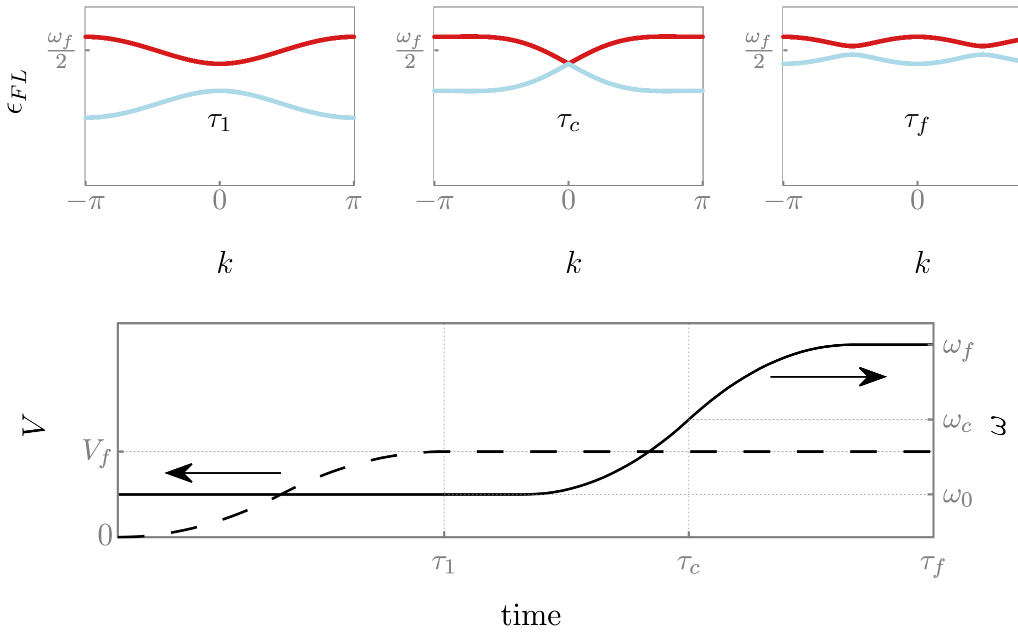

FIGURE 4.4: A 'frequency sweep protocol' allows initializing a long-lived topological Floquet state. Starting with a small frequency ω_0, the amplitude of the oscillating voltage is increased slowly before the frequency is swept up to ω_f. The Floquet topological phase is reached at $\tau = \tau_c$ ($\mu = 0.1\pi$, $t = -\pi$, $\Delta = \pi$, $V_f = 0.2$, $\omega_0 = 0.8\pi$, $\omega_c = 0.9\pi$, $\omega_f = \pi$). The Floquet spectra for $\tau = \tau_1$, τ_c and τ_f are shown on top. Except for the identification of the physical excitations (red) and Bogoliubov shadows (blue), the final Floquet spectrum is the same as the one shown in Fig. 4.3.

4.7.3 Frequency-sweep protocol

Previously, we have discussed that the stability of the Floquet Bogoliubov system crucially depends on the preparation protocol. Indeed, the standard adiabatic state preparation fails, which can be quantified by the Floquet golden rule. The instability can be avoided by a two-step process, shown in Fig. 4.4. First, the oscillating voltage is slowly switched on but at a frequency below the band gap. Therefore, the excitation energy of the physical excitations $E_k > \omega/2$ is larger than half the frequency for all k, and it doesn't cross with the Bogoliubov shadows. Thus, the physical excitation quasi-energy can be analytically calculated as

$$E_k^{\mathrm{FL}} = \frac{\omega}{2} + \sqrt{(\delta\mu|f_k|)^2 + (E_k - \omega/2)^2}, \tag{4.28}$$

where E_k^{FL} is a continuous function for all momenta k, see Sec. 4.6. It is important to note that this protocol gives a different quasi-energy than the adiabatic state preparation, Eq. (4.20). It initializes a distinct many-particle state. In this frequency regime, no Floquet Majoranas are created. We call this the Floquet non-topological phase. The phase, however, can host Majorana zero modes and can be topological

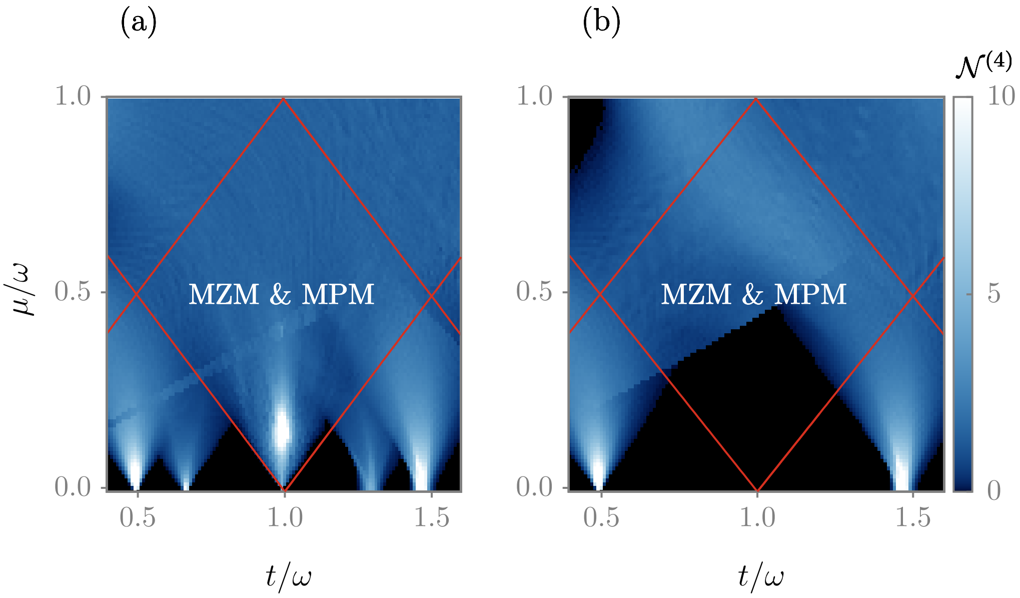

FIGURE 4.5: Normalized phase space density $\mathcal{N}^{(4)} = \frac{1}{N^4}\sum_{\nu_i,m}\delta(E_{\nu_1}+E_{\nu_2}+E_{\nu_3}+E_{\nu_4}+m\omega)$ for the creation of four quasi-particles out of the vacuum ($N = 20$, $\delta E = 0.02$, $t = -\Delta = \pi, \delta\mu = 1$) (a) By adiabatically switching on the oscillating field, the created Floquet state in the topological phase inside the square is always unstable. (b) Using the frequency-sweep protocol of Fig. 4.4 (right), the created Floquet states remain stable for large parts of the topological phase, indicated by the black color.

as defined in equilibrium. The Floquet topological phase is reached as a second step by slowly increasing the frequency. Importantly, the bands only touch instead of cross due to level repulsion. In the end, the physical excitation energy is larger than $\omega/2$ for all momenta k. Close to the phase transition, quasi-particles can be created via the Kibble-Zurek mechanism [158–161]. However, the creation rate $\Gamma^{\frac{d\nu}{1+\nu z}} = \sqrt{\Gamma}$ with $d = 1$ and critical exponents $\nu = z = 1$ for a Dirac equation can be suppressed by a low sweep rate Γ.

One can further quantify the quasi-particle creation by the Landau-Zener formula for the Dirac Hamiltonian $H = m(t)\sigma_z + vk\sigma_x$. The probability for a diabatic transition is given by

$$P = e^{-2\pi\Gamma} \tag{4.29}$$

with $\Gamma = \frac{(vk)^2}{2\partial_t m}$, where $2m(t)$ is the band gap. If we integrate over momentum space, we find the condition $\partial_t m < m^2$ such that less than one quasi-particle created in units of the correlation length $\xi = m/v$

$$P_{\text{tot}}/\xi = \int_{-\infty}^{\infty} \text{dk} e^{-\frac{\pi(vk)^2}{\partial_t m}}/\xi = \frac{\sqrt{\partial_t m}}{\xi v} = \frac{\sqrt{\partial_t m}}{m}. \tag{4.30}$$

The frequency-sweep protocol allows to prepare long-lived Floquet Majoranas

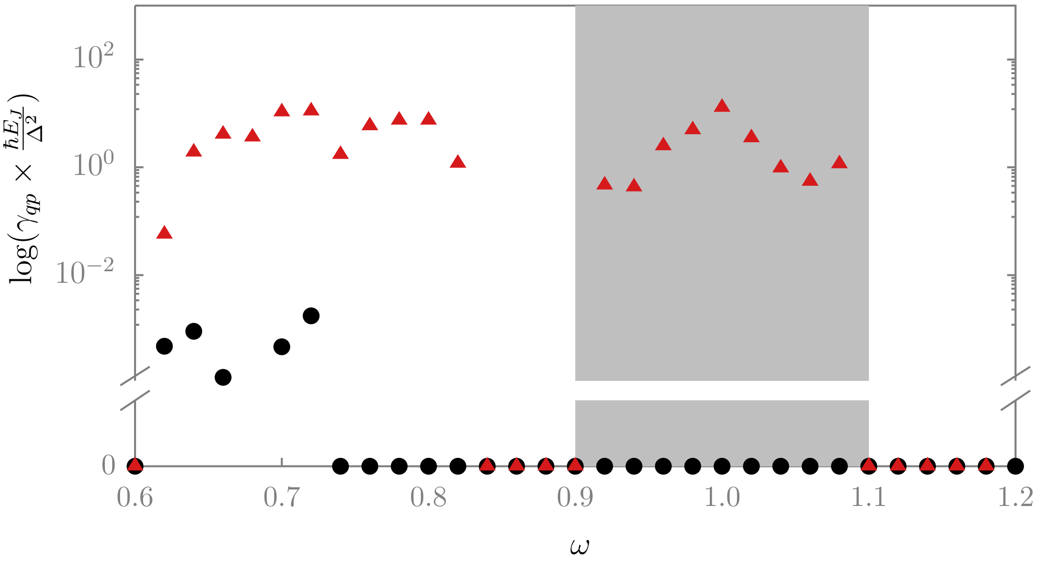

FIGURE 4.6: Quasi-particle creation rate γ_{qp}, computed for $N = 20$ by replacing the δ function by a box of width $\delta E = 0.02$, $t = -\Delta = \pi, \delta\mu = 1, m_{max} = 3$) for creating four quasi-particles out of the vacuum. In the range of coexisting Majorana zero and π modes (grey shaded), the quasi-particle creation rate for the frequency sweep protocol of Fig. 4.4 drops exactly to zero (black dots). The adiabatically prepared Floquet system (red triangles) is unstable due to the finite rate γ_{qp}.

in an extensive parameter range, as shown in the phase space diagram, Fig. 4.5. The phase space is calculated for a finite-size system and, thus, includes processes that involve the bulk and the boundary. In contrast, the instability of spontaneous four quasi-particle creation always occurs in the Floquet topological regime if the system is prepared by only slowly switching on the oscillating. We have also checked that the scattering rate remains finite when the matrix elements are included in the calculation, see Fig. 4.6. In the grey-shaded regions, where both topological modes exist, the scattering rate only vanishes exactly for the frequency sweep protocol.

4.7.4 Higher order interaction effects and disorder

So far, we have shown that the frequency-sweep protocol is stable for long-ranged interactions, appearing in the effective low-energy Hamiltonian (Eq. (4.9)), and for short-ranged interactions. The region of stability does not increase when only momentum-conserving processes are considered. Since the four particle density of states is gapped, we expect the analysis to be robust against weak spatial disorder. Processes that involve the simultaneous creation of 6 or more quasi-particles can still occur. However, these processes are of 4th or higher order in the interaction and strongly suppressed due to the small prefactor.

4.8 Conclusion

In this project, we designed a Floquet topological qubit. In fact, by enhancing the Majorana box qubit into its Floquet equivalent, one can speak of qubits since the Floquet version can encode three logical qubits instead of one. The qubits are defined using Majorana zero modes and Floquet Majoranas in a fixed parity sector. However, the stability of the Floquet Majorana box qubit is tied to the preparation protocol.

Adiabatic state preparation leads to an abundance of resonant quasi-particle creation. This instability is an inherent property of the Floquet Bogoliubov system. However, one can circumvent this problem by initializing the Floquet system first in the phase without Floquet Majoranas and tuning it to the Floquet topological phase only in the second step. This detour can be implemented using, e.g., the frequency-sweep protocol.

The Floquet Majorana box qubit is a versatile quantum tool kit that allows to operate the complete set of Clifford gates in a topologically protected way. Two qubit operations can be implemented using one of the three logical qubits as an ancilla. Furthermore, as outlined by Bomantara and Gong, measurement-based quantum computing operations can be achieved by gated quantum dots that are coupled to the edge modes [162]. Therefore, the Floquet Majorana box qubit can be a test environment for braiding operations.

In conclusion, we present a Floquet topological setup that can be operated even in the presence of weak interactions and disorder. This stability is crucial for any future experimental realizations.

Chapter 5

Programmable Adiabatic Demagnetization

One of the most promising applications of quantum computing is the simulation of complex many-body quantum systems [31]. Quantum simulation requires the ability to initialize a state of interest and to evolve it in time. The time evolution of a quantum state can be implemented on a digital quantum computer, e.g., using a Suzuki-Trotter decomposition of unitary gates. In contrast, the interactions of the qubits or artificial atoms can be tuned by, e.g., lasers in a quantum simulator such that the system evolves according to the Hamiltonian dynamics [4, 8]. In this project, we focus on the difficult task of preparing an arbitrary quantum state.

Accurate and reproducible quantum state preparation is essential for investigating ground state properties in quantum chemistry and material science [61, 69, 70, 163]. Furthermore, quantum state preparation beyond ground states has many quantum information applications [74, 164, 165]. Different quantum algorithms and hybrid techniques for ground state preparation have been proposed, e.g., variational quantum simulation [64, 77, 79–81], adiabatic state preparation [66, 82–84], and, more recently, algorithms that mimic cooling [68, 85–90].

We discussed, in more detail, variational quantum simulation in Sec. 2.3.1. One of the main drawbacks of this method is that it highly depends on the variational ansatz, which is often not easy to find [76, 81]. On the other hand, adiabatic state preparation (see Sec. 2.3.2) can start with a product state and be designed to be easy to implement, e.g., in the computational basis of the quantum computer. However, the initial state must be a ground state of a Hamiltonian which is adiabatically connected to the target Hamiltonian. If a phase transition separates the initial and target states, the protocol breaks down because the adiabatic theorem doesn't hold anymore. For example, a topologically ordered state is not adiabatically connected with a simple product state [98]. Thus, such state preparation requires exponential long times.

Algorithms that use a simulated low-entropy bath to approach the ground state can partially resolve these disadvantages. The entropy of a quantum system can be absorbed by a low-entropy bath. However, in contrast to a large thermal bath, the synthetic bath is simulated only by a small number of the qubits that are periodically reset to the low-entropy state. This class of algorithms works independently of the initial state and is not optimized for a specific target state. Furthermore, by a cyclic repetition of such a cooling protocol, the outcome is more robust against weak noise. If an error has occurred, it can be corrected in the next cycle. Finally, one can learn about the system and the protocol's success by monitoring the bath.

In this chapter, we investigate a protocol that is inspired by a cooling mechanism in solid-state systems, i.e., adiabatic demagnetization [166, 167]. After the specific outline of the protocol, we derive the cooling rate in the perturbative limit. Finally, the protocol is numerically tested by applying it to the transverse field Ising model, closely related to the Kitaev chain of the previous chapter (see Sec. 2.2.3). The model has the property that, at dual points, the excitation spectrum of the ferromagnetic phase looks the same as for the paramagnetic phase. Thus, we can compare the role of trivial (local) and topological (non-local) excitations.

This chapter is based on work in collaboration with Mark Rudner, Achim Rosch and Erez Berg. Mark Rudner and Erez Berg provided a minimal working code at the beginning of the project. I performed the numerical simulations and obtained the analytical results under the supervision of Erez Berg and Achim Rosch. I wrote the manuscript with the help and revisions of the other co-authors. The manuscript has been submitted for peer review and is available as a preprint [P168]. This chapter closely follows the manuscript and figures are mainly reproduced from the paper.

5.1 Simulated adiabatic demagnetization

Adiabatic demagnetization is used in solid-state experiments to reach temperatures in the μK regime [169, 170]. For example, if a system is coupled to nuclear moments that are polarized in a large magnetic field, the temperature can be lowered by adiabatically decreasing the magnetic field [166, 167]. Here, we translate this process for a gapped Hamiltonian to a simulation on a quantum computer, which is illustrated in Fig. 5.1. We consider a one-dimensional system with N qubits, which can be coupled to N_b bath qubits. For simplicity, we assume each system qubit has one bath qubit as a partner, i.e., $N = N_b$. The bath qubits are initialized in a polarized state in the computational basis in the presence of a large simulated Zeeman field in the direction of the polarization axis. Since the outcome of the protocol does not depend on the initial condition, the system qubits can be

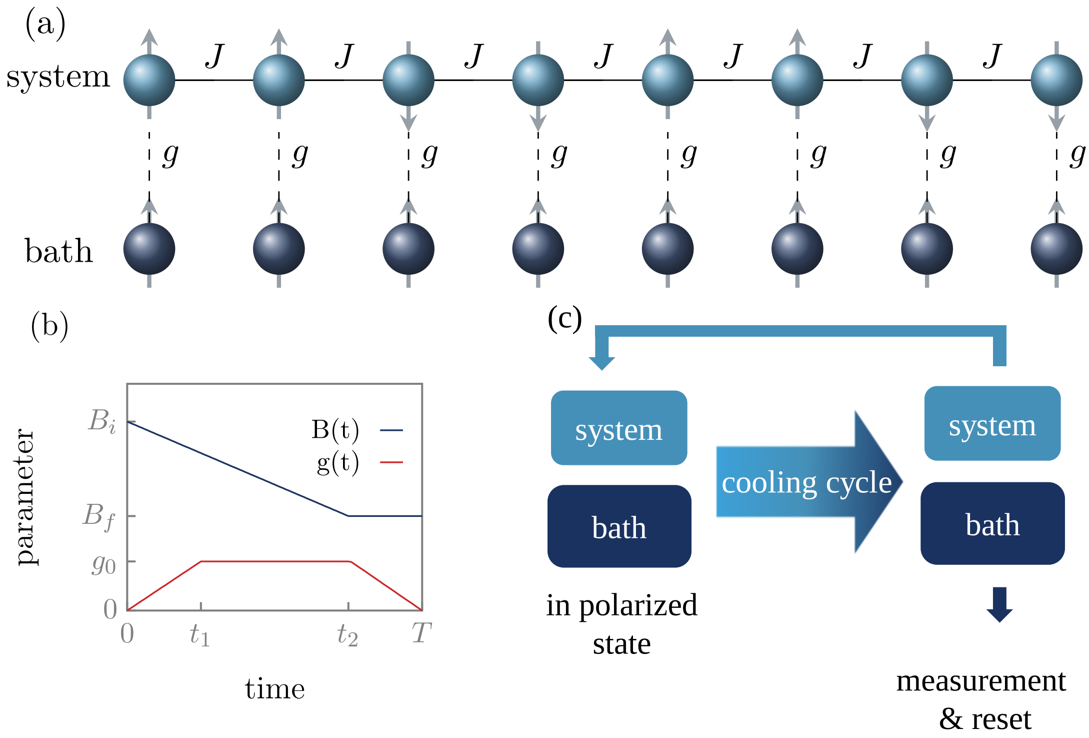

FIGURE 5.1: Schematic of the setup and the proposed protocol. (a) Each system qubit s_i (light blue) is coupled to a bath qubit σ_i by switching on the coupling $g(t)$. For our purpose, the system qubits are coupled by the next-neighbour exchange coupling J, but the couplings may be generalized to more complicated setups. At the beginning of the protocol, the bath qubits are initialized in the polarized ground state $|\uparrow\uparrow\dots\rangle$ and subject to a large simulated magnetic field $B(t)$. The system can be initialized in a random state; in our numerical simulations, we use $|\uparrow\uparrow\downarrow\downarrow\dots\rangle$ for the initialization. After the initialization, the parameters are swept according to panel (b). The magnetic field is linearly decreased from B_0 to B_1 until the time $t = 3T/$ and then kept constant. The system-bath coupling $g(t)$ is slowly increased until $t_1 = T/4$, kept constant at g_0 until $t_2 = 3T/4$, and then slowly switched off. At the end of each cooling cycle, the bath qubits are measured and reset, as illustrated in panel (c).

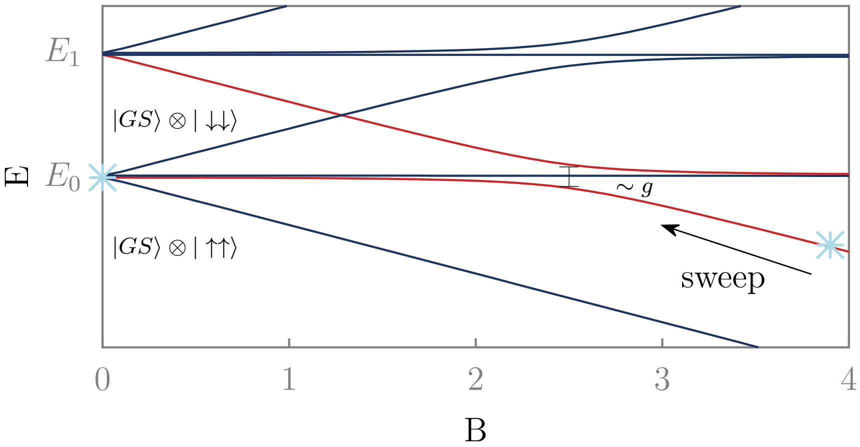

FIGURE 5.2: The system is coupled to two axillary bath qubits. For $B = 0$, the ground state and the first excited state of the composite system are four-fold degenerated. By switching on the magnetic field, the degeneracy is lifted, and a band crossing exists. This crossing becomes an avoided crossing with a gap $\sim g$ if the coupling between the system and the bath is switched on (red line). The cooling protocol starts at a high magnetic field with the bath qubits in the polarized ground state (light blue star on the right side). If the system is initially in the first excited state, the composite system thus starts in a product state at the point marked by the star. By slowly switching on the system-bath coupling and decreasing the magnetic field, one can follow the red line to reach the system's ground state (follow the arrow to the light blue star on the left).

initialized, for example, in an easily accessible product state in the computational basis. We only assume that the system is in an excited state. Energy and entropy can be transferred from the system to the bath by coupling the system and bath and slowly ramping down the simulated Zeeman field.

An intuitive picture of this process can be gained by restricting the problem to only two bath qubits. We focus on the ground state and the first excited state of the system only. If the system and bath are decoupled, and the Zeeman field is zero, the ground state of the composite system is four-fold degenerate, see Fig. 5.2. At a finite Zeeman field, the degeneracy is lifted. By coupling the system and the bath, the combined system exhibits an avoided crossing as a function of the magnetic field, thus, leading to an effective Landau-Zener tunneling problem. Suppose the system is initially in the excited state, and we start with a large magnetic field. In that case, the system can be led to the ground state by adiabatically lowering the Zeeman field. If the sweeping rate is small enough, Landau Zener tunneling is suppressed, and we can follow the lower branch, thus bringing the system to the ground state by flipping the bath qubit. In this picture, we can also understand the effect of noise. If the system was initially in the ground state but an error happened early on, it can be corrected during the same process. In contrast, later-induced excitations can only be removed in the next cycle.

After ramping down the field, and decoupling the system and the bath, we can extract the entropy by measuring and resetting the bath to the initial polarized state. Then, the cooling can be restarted. Note that during the adiabatic process, the entropy of the total system, including the system and bath, stays constant. Only after decoupling and resetting the bath is the entropy removed.

As a final remark, we would like to emphasize that the adiabatic demagnetization protocol is very different from the adiabatic state preparation, despite the similar name. In contrast to adiabatic state preparation, the cooling protocol does not require that the initial product state of the system is adiabatically connected to the target state. In fact, the protocol is independent of the initialization of the system, and no prior knowledge of the target state is needed. However, although a low-energy state can always be reached, the exact preparation of long-ranged entangled ground states is still bound by the Lieb-Robinson bound [98], see Sec. 5.2.5. Furthermore, due to the cyclic property, we can correct errors on the adiabatic path, which is impossible with adiabatic state preparation. Measuring the bath qubits can give information on whether an error occurred. This information can be used as a stopping criterion for the protocol.

5.1.1 Cooling protocol

Our main goal is to prepare the ground state or low-energy state of an arbitrary gapped quantum Hamiltonian H_s. Local degrees of freedom $\hat{A}^s$ of the system are coupled to the spin operators $\boldsymbol{\sigma}_i$ of the bath

$$H = H_s + \sum_{i=1}^{N} [g(t)\hat{A}_i^s \sigma_i^y - B(t)\sigma_i^z], \tag{5.1}$$

where $g(t)$ is the time-dependent coupling strength, and the simulated Zeeman field $B(t)$ is only applied on the bath. At the beginning of the protocol, the bath is prepared in the fully-polarized state $|\psi_B^0\rangle = |\uparrow\uparrow\uparrow \dots\rangle$, while the system is in an arbitrary excited state. The protocol is repeated for N_c cycles. During each cycle, the time dependence of the parameters $B(t)$ and $g(t)$ is shown in Fig. 5.1b. From time $0 < t < t_1$, the coupling strength is linearly increased, kept constant for $t_1 < t < t_2$, and linearly reduced to 0 for $t_2 < t < T$. At time $0 < t < t_2$, the magnetic field is linearly ramped down from B_i to B_f. At the end of each cycle the bath qubits are measured and reset to the initial state $|\psi_B^0\rangle$. The bath starts in a zero entropy state in an ideal setup without noise. During the adiabatic decrease of the Zeeman field, entropy and energy are transferred from the system to the bath. The measurement and reset of the baths extract the entropy such that the bath is again in a state with zero entropy at the beginning of the next cycle. We discuss the effect of noise in Sec. 5.2, where we show that the information of the measurement can be used to enhance the performance of the protocol.

5.1.2 Cooling rate and analytical considerations

In this section, we derive the cooling rate $\Gamma_c(t) = -\frac{d}{dt}\langle H_s \rangle = -\langle i[H_s, H] \rangle$ for small system bath coupling in the linear response regime (for an introduction to linear response theory see Sec. 3.3)

$$\Gamma_c = -ig(t)\int_0^t dt'\, g(t') \sum_i \langle \psi | [\dot{\hat{A}}_i^s(t)\sigma_i^y(t), \hat{A}_i^s(t')\sigma_i^y(t')] | \psi \rangle, \tag{5.2}$$

where $\dot{\hat{A}}_i^s(t) = i[H_s, \hat{A}_i^s(t)]$ and, in the interaction picture, all time-dependent operators follow the dynamics of the Hamiltonian with $g = 0$. We assume that H_s is generically self-equilibrating as it includes many-body interaction terms and is generally not integrable. $|\psi\rangle$ of Eq. (5.2) denotes the wave function at the beginning of the protocol, where the system and bath are disentangled, and the bath is fully polarized. As outlined below, the cooling rate can be evaluated for adiabatically changing parameters $g(t)$ and $B(t)$ using the stationary phase approximation

$$\frac{\Gamma_c}{N} \approx -4\pi g(t)^2 \int d\omega [1 + n_B(\omega)]\omega \chi_s''(\omega) \delta(\omega + 2B(t)), \tag{5.3}$$

where $n_B(\omega)$ is the Bose function and $\chi_s''(\omega) = \frac{1}{N}\sum \chi_{s,i}''(\omega)$ is the averaged imaginary part of the local retarded susceptibility $\chi_{s,i}(t) = i\theta(t)\langle [\hat{A}_i^s(t), \hat{A}_i^s(0)] \rangle$, where θ is the Heaviside function. Eq. (5.3) shows that mainly resonant processes contribute to the cooling rate. Energy is extracted if the excitation energy matches the cost of flipping a bath spin $2B(t)$. While decreasing the magnetic field, the bath absorbs high-energy excitations at short times, then lower-energy excitations at longer times. The total amount of energy $\int dt \Gamma_c$ removed during one protocol cycle depends on the sweep rate $\dot{B}$ and is inversely proportional to the sweep duration T. This relation comes from replacing the time integral with an integral over the magnetic field $\int dt = \int \frac{dB}{\dot{B}}\, g^2/\dot{B} \propto g^2 T$.

We continue this section by explicitly executing the perturbative calculation outlined above. We start with the expectation of the time derivation of the Hamiltonian H_s

$$\langle \dot{H}_s \rangle = i\langle \psi(t) | [H_c, H_s] | \psi(t) \rangle, \tag{5.4}$$

where $H_c = g(t)\sum_{i=1}^{N} \hat{A}_i^s \sigma_i^y$ describes the coupling of N local degrees of freedom A_i^s of the system to the bath spins. The bath spins are denoted by the spin operators $\boldsymbol{\sigma}_i$. We describe the time evolution of the wave function $|\psi(t)\rangle = U_I(t,0)|\psi(0)\rangle$ in the interaction picture. The Hamiltonian with $g = 0$ generates the time evolution of the operators. For small coupling g, we can use perturbation theory to expand the time evolution operator up to the first order in the interaction

$$U^I(t,0) \approx \mathbb{1} - i\int_0^t H_c(t')dt'. \tag{5.5}$$

Inserting the approximation of Eq. (5.5) into Eq. (5.4) and keeping terms up to 2nd order in the interaction, we obtain

$$\begin{aligned}\langle \dot{H}_s\rangle &\approx g(t)\int_0^t dt' \langle\psi(0)|[[\hat{A}_i^s(t)\sigma_i^y(t), H_s], H_c(t')]|\psi(0)\rangle \\ &= -ig(t)\int_0^t dt' g(t')\sum_j(\langle\hat{A}_j^s(t')\dot{\hat{A}}_j^s(t)\rangle\langle\sigma_j^y(t')\sigma_j^y(t)\rangle + \text{c.c.},\end{aligned} \tag{5.6}$$

where we use in the second line that $i\langle\psi(0)|[H_c, H_s]|\psi(0)\rangle = 0$. Next, we calculate $\langle\dot{H}_s\rangle/N$ per site. As the system and bath are initially disentangled, the expectation value factorizes into a system contribution $\Sigma_S(t,t') = \langle\hat{A}_i^s(t')\dot{\hat{A}}_i^s(t)\rangle$ and the bath contribution $\Sigma_B(t,t') = \langle\sigma_y(t')\sigma_y(t)\rangle$. Assuming that the system is thermalizing, we use the fluctuation-dissipation theorem (see Sec. 3.3) to evaluate the system correlation function

$$\Sigma_s(\omega) = 2i\omega(1 + n_B(\omega))\chi_s''(\omega), \tag{5.7}$$

where $\chi_s''(\omega)$ is the imaginary part of the local A_i^s susceptibility per site and $n_B(\omega)$ the Bose function at an effective temperature of the system. The factor ω in Eq. (5.7) comes from the time derivative $\dot{A}_i^s(t)$ in the expectation value, which is absent in the usual fluctuation-dissipation theorem. While the system contribution is a general expression, we want to evaluate the bath contribution for the suggested implementation of the protocol. Therefore, we explicitly write the time-evolved spin operators as $\boldsymbol{\sigma}_i(t) = e^{i\int H_b(t')dt'}\boldsymbol{\sigma}_i e^{-i\int H_b(t')dt'}$, where $H_b = -B(t)\sum_i \sigma_i^z$ is the Hamiltonian of the bath qubits. Then, the y-component of the spin operator has the form

$$\sigma_i^y(t) = \sin(2\theta_B(t))\sigma_i^x + \cos(2\theta_B(t))\sigma_i^y \tag{5.8}$$

with $\theta_B(t) = -\int_0^t B(t')dt'$. We evaluate the expectation value with respect to the initially fully polarized state of the bath $|\psi_i^B(t)\rangle = |\uparrow\uparrow\dots\rangle$

$$\langle\sigma_j^y(t')\sigma_j^y(t)\rangle = e^{2i(\theta_B(t')-\theta_B(t))}. \tag{5.9}$$

Now we rewrite Eq. (5.6) per site in terms of the system contribution Eq. (5.7) and the bath contribution Eq. (5.9)

$$\begin{aligned}\frac{\langle\dot{H}_s\rangle}{N} &= 2\int d\omega[\omega(1+n_B(\omega))\chi_y''(\omega) \\ &\quad\times g(t)\int_0^t dt' g(t')e^{2i(\theta_B(t')-\theta_B(t))}e^{+i\omega(t-t')}] + c.c..\end{aligned} \tag{5.10}$$

If we integrate the second line of Eq. (5.10) over the sweep duration, we can quantify how much energy is transferred to the bath from a mode at frequency ω

$$\Delta_c(T,\omega) = \int_0^T dt g(t)\int_0^t dt' g(t')e^{2i(\theta_B(t')-\theta_B(t))}e^{+i\omega(t-t')}] + c.c.. \tag{5.11}$$

With the above expression, we can formally write down the total extracted energy

$$\frac{\Delta E_{\text{tot}}}{N} = 2\int d\omega\,\omega(1+n_B(\omega))\chi_s''(\omega)\,\Delta_c(T,\omega). \tag{5.12}$$

We want to evaluate this expression for slowly varying coupling g and slow and linear ramp down of the magnetic field $B(t) = B_0 - \Gamma_b t$, where B_0 is the initial value of the magnetic field and $\Gamma_b = |\partial_t B(t)|$ is the sweep rate. Now, we use the stationary phase approximation to carry out the two time integrals. The stationary phase approximation is valid in the limit of an adiabatic sweep. We expand the argument of the exponential function in a Taylor series up to the 2nd order around the resonance point around the stationary point t^*. At times t and t' near t^*, i.e. near the resonance $2B(t^*) = -\omega$, the integrand contributes most. The factor 2 arises because a single spin flip of the bath costs $2B$ or, more technically, because we used Pauli matrices instead of spin matrices. Thus, we obtain

$$\begin{aligned}\frac{\Delta_c(T,\omega)}{g(t^*)^2} &\approx \int_0^T dt\int_0^t dt' e^{-i\left((t-t^*)^2-(t'-t^*)^2\right)\Gamma_B} + c.c. \\ &= \int_0^T dt\int_0^T dt' e^{-i\left((t-t^*)^2-(t'-t^*)^2\right)\Gamma_B} \\ &\approx \frac{\pi}{\Gamma_B} \quad \text{for } \Gamma_B \to 0,\ t^* < T,\end{aligned} \tag{5.13}$$

where the Fresnel integral $\int_0^\infty dt \cos(t^2) = \int_0^\infty dt \sin(t^2) = \sqrt{\pi/8}$ is evaluated under the condition that t^* and T scale with $1/\Gamma_b$. In the end, we find

$$\Delta_c(T,\omega) \approx g(t^*)^2 \frac{\pi}{\Gamma_B}(1-\theta(\omega+2B(T))). \tag{5.14}$$

In Fig. 5.3a, we compare the analytically derived expression of Eq.(5.14) to a numerical evaluation of the integral. Indeed, the Heaviside function well reproduces the behavior while neglecting the small oscillations. To obtain the contribution of the bath to the cooling rate, we take the time derivative of $\Delta_c(T,\omega)$

$$\Sigma(t,\omega) = \partial_t \Delta_c(t,\omega) = 2\pi g(t^*)^2 \delta(\omega + 2B(t)). \tag{5.15}$$

Finally, we insert the above expression into Eq. (5.10) such that the cooling rate per site in the adiabatic limit becomes

$$\frac{\langle \dot{H}_s \rangle}{N} \approx 4\pi g(t)^2 \int d\omega \delta(\omega + 2B(t)) \omega (1 + n_B(\omega)) \chi_s''(\omega). \tag{5.16}$$

As we discussed at the beginning of this section, energy is mainly extracted at the resonance point. However, this condition only strictly holds in the adiabatic limit. We can explore the cooling efficiency beyond the adiabatic regime by direct numerical evaluation of the integral Δ_c. In Fig. 5.3, we show the effect of faster sweeps by plotting $\Delta_s(T,\omega) = \Delta_c(T,\omega) - \Delta_c(T,-\omega)$ as a function of T. This expression includes heating and cooling processes. Heating occurs if a mode at frequency ω is added while cooling extracts the mode. The ratio of these terms is determined by the Bose function $n_B(\omega)$ and thus effectively by the temperature of the system. For the plot, we assume that the temperature is much larger than the energy $\hbar\omega$ such that $n_B(\omega) \approx \frac{T}{\omega} \approx -n_B(-\omega)$. Thus, the ratio is one, and both processes contribute equally. Furthermore, we normalize $\Delta_s(T,\omega)$ to $\Delta_s^A = \frac{\pi g(t^*)}{\dot{B}}$ which we analytically obtained in the adiabatic limit. The cooling is strongly suppressed for very fast sweeps, i.e., very short T, while very slow sweeps (very large T) recapture the analytical result. In the intermediate regime, the cooling strength depends on the exact protocol as well as on the frequency of the mode. Interestingly, energy can be extracted already quite efficiently for fast sweeping rates. Thus, the sweeping rate can be adjusted to the noise level such that cooling is more rapid than reheating due to noise. In the currently noisy devices, this is highly relevant.

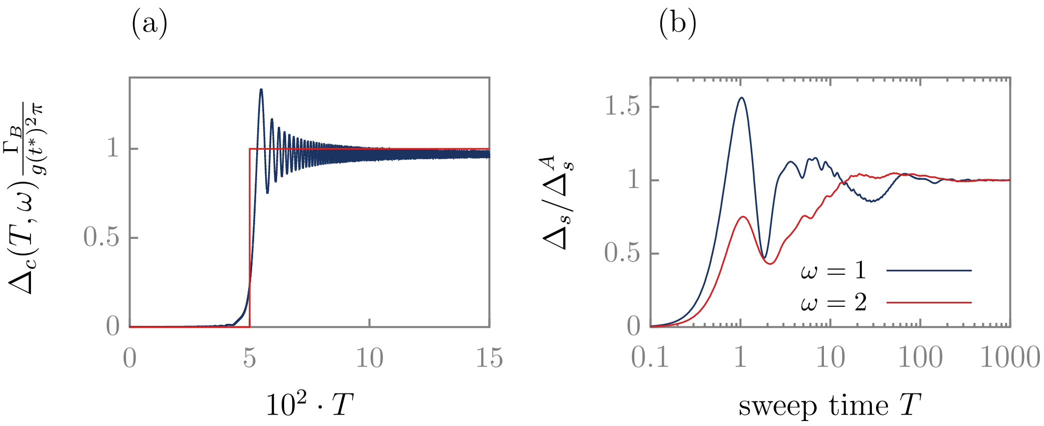

FIGURE 5.3: (a) The bath absorption rate $\Delta_c(T,\omega)$ (blue), defined in Eq. (5.11), as a function of sweep duration T in the perturbative analysis for $B_i = 1$, $B_f = 0.001$ and $\omega = -1$ compared to the approximation of Eq. (5.14). (b) Plot of $\Delta_s(T,\omega) = \Delta_c(T,\omega) - \Delta_c(T,-\omega)$ as a function of $T = 1/B_i$ for $\omega = 1$ (blue) and $\omega = 2$ (red). Δ_s is normalized to the value computed from the adiabatic approximation, $\Delta_s^A = \frac{\pi g(t^*)^2}{\Gamma_B}$, see Eq. (5.13). In this plot, we use $B(t) = 5(1 - t/T)$. The system-bath coupling $g(t)$ increases linearly for $t < T/4$ from 0 to a finite value g, remains constant for $T/4 < T < 3T/4$, and decreases linearly to 0 for $t > 3T/4$.

5.2 The effect of noise and topological excitations

To study the performance of the protocol in the presence of noise, we numerically investigate its application to the one-dimensional quantum Ising model

$$H_s = -\sum_i J s_i^z s_{i+1}^z - \sum_i \left(h_x s_i^x + h_z s_i^z\right) \tag{5.17}$$

with the exchange interaction J, a transverse field h_x and a longitudinal field h_z. The system spin operators are denoted $\boldsymbol{s_i}$, while $\boldsymbol{\sigma_i}$ refers to the bath. The longitudinal field can make the model non-integrable. In the absence of the longitudinal field, this Hamiltonian is known as the transverse field Ising model. The Jordan-Wigner transformation connects it to the Kitaev model (see Sec. 2.2.3). The model hosts a paramagnetic and ferromagnetic phase with a critical point at $J = h_x$. The low-energy excitation of the ferromagnetic phase can be mapped to the high-energy excitations of the paramagnetic phase by the Kramer-Wannier transformation. At dual points, the excitation spectrum of the ordered and disordered phases thus looks identical. We use this property to compare the efficiency of the protocol in the presence of topological excitations in the form of domain walls with trivial (local) excitations in the paramagnetic phase. In the following, we use periodic boundary conditions if not specified otherwise. The bath spin operators $\boldsymbol{\sigma_i}$ couple to the local degrees of freedom of the system $A_i^s = s_i^y$. We chose the $s_i^y \sigma_i^y$ exchange coupling because the operators do not commute with the Hamiltonian.

5.2.1 Numerical method

We use the stochastic Schrödinger equation to investigate the cooling protocol in the presence of noise numerically, see Sec 3.4.5. Without noise, we numerically integrate the Schrödinger equation by a second-order Suzuki-Trotter decomposition (see Sec. 3.1.3). The time evolution $U = \prod_n U_n$ contains n Trotter steps of length $\Delta\tau$

$$U_n = e^{-i\frac{\Delta\tau}{2}H_Z(t_n)}e^{-i\Delta\tau H_Y(t_n)}e^{-i\Delta\tau H_X(t_n)}e^{-i\frac{\Delta\tau}{2}H_Z(t_n)}. \tag{5.18}$$

The $H_{X,Y,Z}$ are the terms of the Hamiltonian that contain only X, Y, or Z operations. To account for noise, we randomly apply one of the Pauli operators on all qubits after the first unitary $U(H_Z)$ and the third unitary $U(H_Y)$ in each Trotter step with probability p_{err}. The random application of Pauli operators implements single-qubit depolarizing noise channel, see Sec. 3.4.3. In our simulation, we implemented a short step length $\Delta\tau = 0.06$, which corresponds to an almost continuous time evolution. Such an implementation can be realized in analog quantum simulators, e.g., in Rydberg atom experiments [8]. The shallow circuit depth is important for a successful experiment in the current digital quantum computers, e.g., based on superconducting qubits [19]. Thus, one has to increase $\Delta\tau$ to reduce the number of gates. After the noisy Trotter evolution, the bath qubits are projectively measured and reset to the initial fully-polarized state. After the measurement, the system is disentangled from the bath and is in a pure state. As we see later, the measurement results can be used to enhance the performance of the protocol further, but monitoring the bath is not necessary for the success of the cooling.

5.2.2 Single run

We first investigate a self-thermalizing Hamiltonian, i.e., with a finite longitudinal field. In Fig. 5.4, we plot the difference between the system energy and the ground state energy $E - E_0$ of a single trajectory for $N_c = 100$ cooling cycles, where the expectation value of system energy is always calculated after the bath is measured. In the upper panel, we show the ground state fidelity, which is the overlap of the ground-state wave function with the system wave function after measuring the bath. We also indicate with a grey vertical line whenever the bath measurement reveals that at least one bath spin has flipped. The calculation included a total of 16 qubits ($N_b = N_s = 8$). The figure caption states all other parameters. Without

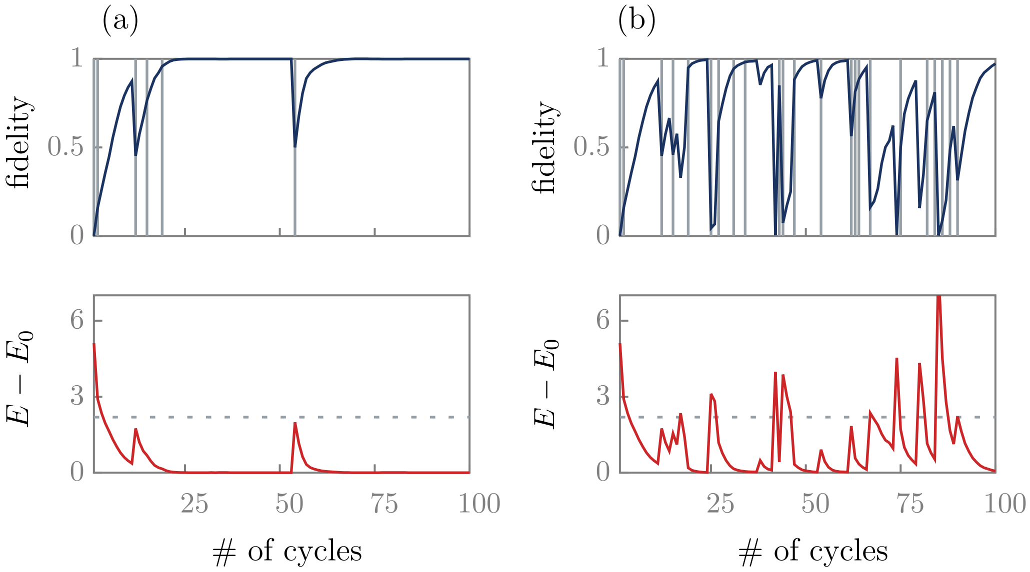

FIGURE 5.4: Single run of the protocol for the non-integrable case ($J = 1$, $h_x = 1$, $h_z = 0.2$, $N_s = 8$, $N_\tau = 101$, $T = 6$, $B_i = 5$, $B_f = 0.7$, $g_0 = 0.5$). The system's ground state fidelity and energy are calculated at the end of each cycle. (a) No external noise is applied, i.e., only adiabatic and Trotter errors occur. (b) $2 \cdot 10^{-2}$ errors per sweep and spin is applied. The top panels show the system ground state fidelity, $|\langle\psi(t_n)|GS\rangle|^2$, where t_n denotes the end of the nth cycle (blue). Vertical grey lines indicate when a flipped spin is observed in the bath at the end of a cycle. The bottom panels show the difference between the expectation value of the system's energy at the end of each cycle and its ground state energy, $\langle\psi(t_n)|H_s|\psi(t_n)\rangle - E_0$, (red). The dashed grey line indicates the energy gap of the system, $E_1 - E_0$. At the noise level used in panel (b), the average system energy remains below the gap.

noise, the system energy drops below the first excited energy level, indicated as the grey dashed line, after 3-4 protocol cycles, Fig. 5.4a. It takes longer for the system to approach the ground-state wave function. After around 20 cycles, the ground state fidelity reaches approximately one.

Occasionally, the energy abruptly increases again due to a combination of Trotter and adiabatic errors. Whether the error leads to a jump in energy also depends on the measurement, which is intrinsically random. However, these errors can be monitored through the bath since a spin flip occurs coincidentally in the bath. Thus, a (post-) selection regarding the measurement outcome can lead to an enhanced fidelity or serve as an effective thermometer. It is enough to use the measurement outcome as a signal to stop the protocol. Instead of running into the post-selection problem of selecting a specific series of measurement results, here it is a question of the right timing.

In the ideal setup without errors, the system stays in the ground state during a perfectly adiabatic process once it has reached it. There is no excess energy that the bath can absorb. Therefore, no bath spin flips either. Thus, a series of measurements where the bath has not flipped strongly indicates that the system has reached the ground state. Even with noise, the system reaches a low energy steady state, and the measurement information helps to gain a better performance.

In Fig. 5.4b, we show that the protocol is resilient to noise. We apply depolarizing noise with a probability of $p_{err} = 10^{-4}$, which amounts to an average number $\eta_e = 2 \cdot 10^{-2}$ of errors per sweep per spin. Of course, the external noise is reflected in the more significant number of jumps in energy and fidelity. But the cooling protocol can still correct the errors such that the average number of excitations stays below 1. Averaging over many noise realization leads to low-energy steady state, see below.

5.2.3 Topological and trivial excitations

Finally, we compare the efficiency of the protocol for a system with trivial and topological excitations in the presence of noise. We show the steady-state energy density $e = (E - E_0)/E_0$ averaged over $N_{init} = 1000$ trajectories for the ferro- (red squares) and paramagnetic phase (blue circles) and different error rates in Fig. 5.5. The parameters are chosen at the dual points of the transverse field Ising model (with $h_z = 0$) such that the excitation spectra look identical. The system in the paramagnetic phase is easier to cool as excitations can be removed by local operations. In contrast, it is more difficult to annihilate topological (non-local) excitations in the ferromagnetic phase.

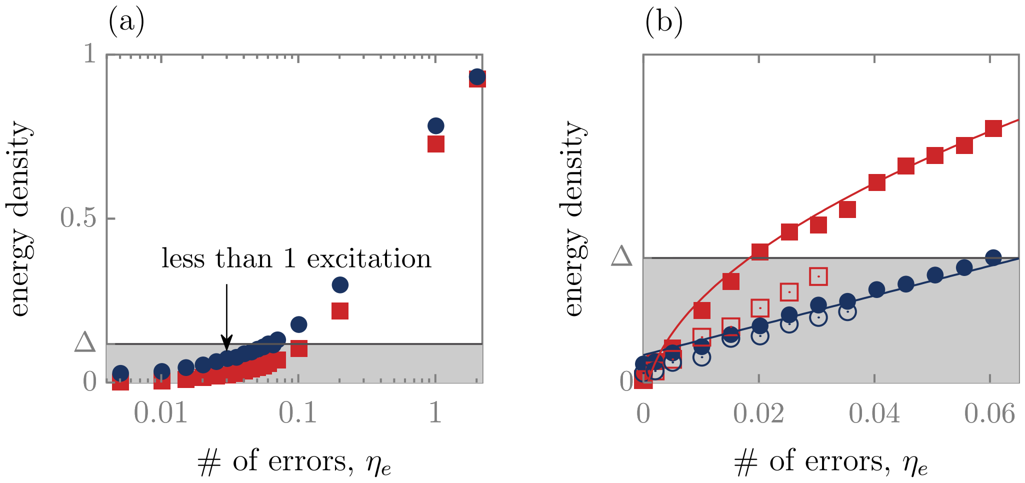

FIGURE 5.5: Energy density $(E - E_0)/E_0$ as a function of the average number of error η_e: (a) The ferromagnetic case ($J = 1$, $h_x = 0.5$, $h_z = 0$) is shown in red squares, the paramagnetic case ($J = 0.5$, $h_x = 1$, $h_z = 0$) in blue dots. Within the grey shaded area below the line at the single excitation gap $\Delta = (E_1 - E_2)/E_1$, the system hosts less than one excitation on average. (b) For small noise levels, post-selection (empty red squares FM, empty blue circles PM) decreases the energy density, thus, enhancing the outcome of the protocol. However, for large error rates, the post-selection criterion cannot identify a successful end within the 100 cycles. The straight lines are fitted with $ax + b$ (FM) and $c\sqrt{x} + d$ (PM). Fit parameters: $a = 1.4 \pm 0.03$, $b = 0.026 \pm 0.002$, $c = 1.1 \pm 0.03$, $d = -0.031 \pm 0.006$.

The eight qubit system hosts less than one excitation for noise levels below 0.02 and 0.05 for the ferro- and paramagnetic cases, respectively, indicated by the grey shaded area in the zoom-in of Fig. 5.5b. The energy density e increases linearly with the number of errors in that regime. However, due to adiabatic and Trotter errors, as seen for the single trajectory, the energy density remains finite even if the error rate goes to zero. The efficiency of the protocol can be increased by about 20%-50% (empty symbols) if the protocol is stopped at the "right" time: The protocol is executed for 20 cycles and then stopped once the bath was measured in the fully-polarized state for 5 consecutive cycles. This stopping criterion is based on the observation that for an ideal simulation the bath qubits will not change once the system reached the ground state. However, if the noise rate is too high (an average number of error above 0.03), the stopping criterion is not fulfilled in every of the 1000 trajectories during the 100 cycles. For consistency, we only plot the average of 1000 post-selected trajectories.

The numerical analysis is limited in system size, but the qualitative difference of the protocol performance due to the nature of excitations can also be revealed by a rate equation of excitation density $n = N_{\text{ex}}/V$ (the ratio of the number of excitations N_{ex} and the system's volume V),

$$\partial_t n = \Gamma_{\text{noise}} - \gamma_c n^M. \tag{5.19}$$

Excitations are created with an error rate Γ_{noise} and annihilated with a cooling rate γ_c in a process that depends on the nature of the excitations. Some types of local excitation ($M = 1$) can be removed individually, but $M > 1$ requires the simultaneous removal of M adjacent excitations. The removal of pairs or higher-order clusters is necessary for topological excitations. However, $M > 1$ is also possible for topologically-trivial excitations. For example, electron-hole excitations of a semi-conductor can only be removed in pairs, i.e., in an $M = 2$ process, whereas bound excitons are easily removed, $M = 1$.

In the steady state $\partial_t n = 0$, the excitation density amounts to

$$n = \left(\Gamma_{\text{noise}}/\gamma_c\right)^{1/M}. \tag{5.20}$$

The steady state reflects what we have guessed and seen in the numerics: Non-local excitations are more challenging to remove. Therefore, the cooling protocol is most powerful for $M = 1$, i.e., if excitations can be annihilated individually, like in the paramagnetic phase. On the other hand, in the ferromagnetic case, only domain wall pairs in close distance can be removed, thus $M = 2$.

While Eq. (5.19) models the thermodynamic limit, we can adapt it for a finite-size system. For small noise levels $\Gamma_{\text{noise}} \to 0$, the number of excitation is very low, such that the probability of finding two or more excitations at the same position scales inversely with the volume V of the system, $p \sim 1/V^{M-1}$. Thus, for $n \lesssim M/V$, we can replace n^M in Eq. (5.19) by n/V^{M-1} and we obtain the steady-state excitation density

$$n \sim \frac{\Gamma_{\text{noise}}}{\gamma_c} V^{M-1}. \tag{5.21}$$

The relation of Eq. (5.21) is also reflected in the numerical calculation shown in Fig. 5.5b, where the energy density scales approximately linearly with the error rate (paramagnetic phase) and as the square root of the error rate (ferromagnetic phase), respectively, for small noise rates. This is because, in a gapped system, the energy density can be heuristically estimated as excitation density. The two approaches yield the same qualitative result. Furthermore, we checked that the energy density is system size independent for the paramagnetic phase ($M = 1$), see Fig. 5.6. In contrast, the energy density of the ferromagnetic phase increases linearly with the system size, as expected for a $M = 2$ annihilation process.

5.2.4 Trapping of excitations

Topological excitations are notoriously difficult to cool, as shown in the last section. Even though it might not be possible to erase all topological excitations, we can at least attenuate the problem by localizing them in space. Unlocalized "free" excitations are highly mobile. These high-energetic excitations can be localized by trapping them at a specific site in lower-energy state. While the number of excitations does not change, we can remove the energy difference between the mobile and the trapped excitations by the cooling protocol. In the Ising model, the ferromagnetic phase hosts domain walls that can be trapped by lowering the exchange interaction $J_{trap} < J$ at a specific bond. It is energetically favorable for the domain wall to be at the trapping bond. We analyze the expectation value $\langle s_i^z s_{i+1}^z \rangle$ to see the effect of this trap in Fig. 5.7, where $\langle s_i^z s_{i+1}^z \rangle$ is plotted as a function of the bond index and time in terms of protocol cycles. Here, we use open boundary conditions. A smooth profile with $\langle s_i^z s_{i+1}^z \rangle$ being approximately 1 or -1 indicates ferromagnetic order as observed for the noise-less steady state in Fig. 5.7a. In the presence of noise, the expectation value $\langle s_i^z s_{i+1}^z \rangle$ is decreased, indicating that domain walls are delocalized and move freely, see Fig. 5.7b. An abrupt change in the correlation function reflects a bond that binds a domain wall. As demonstrated in Fig. 5.7c and d, the trap localizes the domain wall.

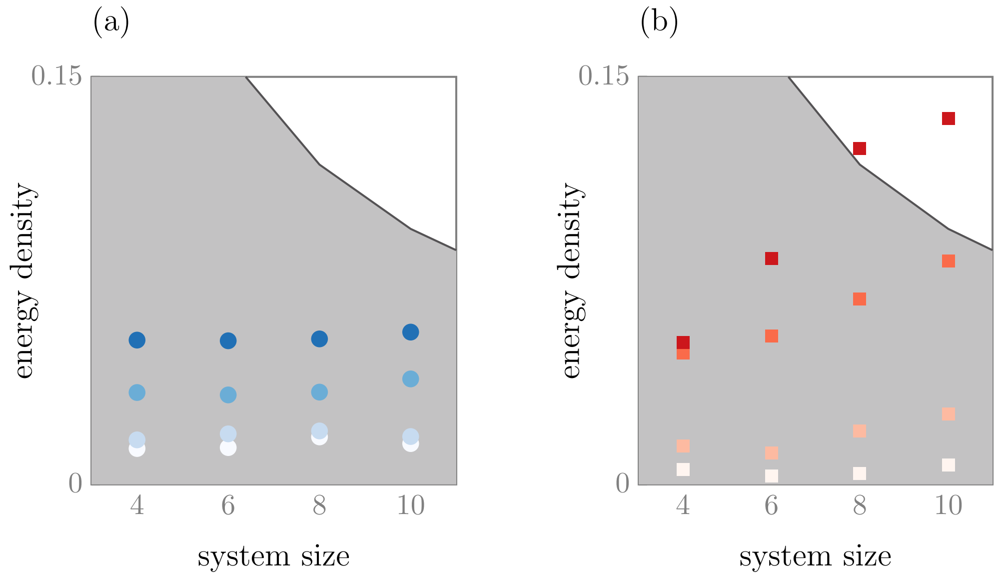

FIGURE 5.6: Energy density $(E - E_0)/E_0$ as a function system size for (a) the paramagnetic case and (b) the ferromagnetic case and for an average number of errors $\eta_e = 0, 2 \cdot 10^{-3}$, 10^{-2} and $2 \cdot 10^{-2}$ per sweep and spin (light to dark). The average energy below the gap of the system is marked by the grey-shaded area. In the paramagnetic phase, the energy density is system-size independent, growing only with η_e, whereas the energy density increases approximately linearly with system size in the ferromagnetic case. The growth of the energy density as a function of system size is higher with increasing η_e. Both the system size and error rate dependence reflect the rate equation model, Eqs. (5.19) and (5.21). Parameters are the same as in Fig. 5.5.

5.2.5 Can we efficiently prepare a topological ground state?

While we argue that our protocol works in the thermodynamic limit and has great advantages over the adiabatic state preparation technique, the question arises whether we can efficiently prepare ground states with topological order. Using adiabatic state preparation it is not possible to prepare a topologically ordered state from a product state, see Sec. 2.3.2. Similarly, topologically ordered states cannot be prepared by a finite depth unitary due to their long-range entanglement, see Sec. 2.3.4.

So far, we have discussed that the topological excitations are more difficult to annihilate but a low-energy steady state is reached in the presence of topological excitations. Despite the measurements as non-unitary elements, the cooling protocol, of course, does not outperform the Lieb-Robinson bound.

(Abelian) topological excitations can only be efficiently removed if further information on the excitations, e.g., the type and location is inferred by measurements. For example, we can use the trapping technique to localize the excitations and verify the location by measurements. Then, a similar feed-forward technique,

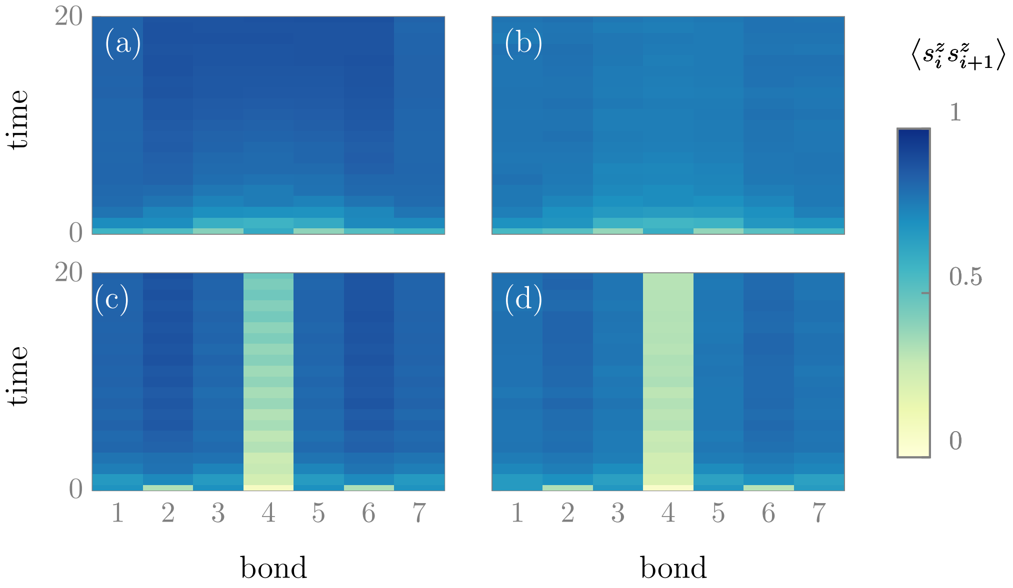

FIGURE 5.7: Bond correlation function $\langle s_i^z s_{i+1}^z \rangle$ for the ferromagnetic case ($J = 1, h_x = 0.5$, $h_z = 0$) with open boundary conditions with no noise (left) and an average number of errors of $\eta_e = 2 \cdot 10^{-2}$ per sweep and spin (right). There is no trap for data in panels (a) and (b). For panels (c) and (d), the trap is implemented by a lower J coupling $J_{trap} = 0.33J$ between the 4th and 5th spin. Parameters: $N_s = 8$, $N_\tau = 101$, $N_c = 100$, $N_{init} = 1000$, $T = 6$, $B_i = 5$, $B_f = 0.7$, $g_0 = 0.5$.

as discussed in Sec. 2.3.4, can be used to reach the ground state. In the ferromagnetic phase of the Ising model, one can use an s^x-string operator to annihilate the domain walls. While the ferromagnetic ground state of the Ising model does not exhibit long-range entanglement, the approach can be generalized to models with a topologically ordered ground state.

5.2.6 Steady-state energy distribution

The population of energy levels for the system's steady state shows striking features. In Fig. 5.8, we plot the occupation $|\langle \psi_n | \psi_{out} \rangle|^2$ of each energy level E_n, where $|\psi_{out}\rangle$ is the steady-state and n labels the energy level of the system Hamiltonian. Here, we again use periodic boundary conditions. The steady state of the system is a non-equilibrium state because the system is perturbed by the coupling to the bath and through the measurement. Still, in the (integrable) paramagnetic case, the energy population approximately follows a thermal distribution. The occupation decreases exponentially in energy. In contrast, the distribution is separated in different domain wall sectors for the ferromagnet, indicated by jumps in the distribution. For each sector with 0, 2, and 4 domain walls, the system equilibrates

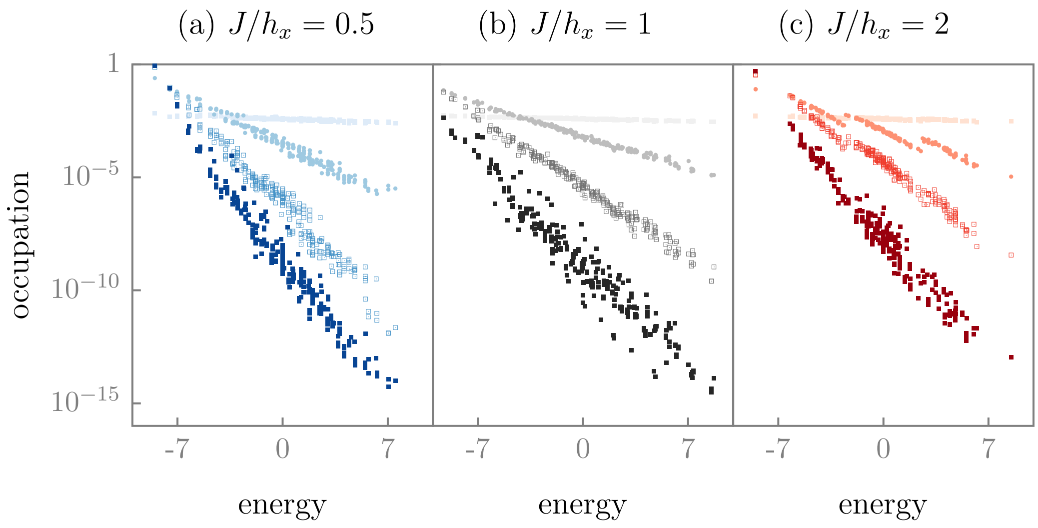

FIGURE 5.8: Occupation of system energy eigenstates for noise rates $\eta_e = 0, 0.02, 0.2, 2$ per sweep and spin (dark to light) for (a) the paramagnetic ($J = 0.5$, $h_x = 1$, $h_z = 0$), (b) the non-integrable ($J = 1$, $h_x = 1$, $h_z = 0.2$) and (c) the ferromagnetic case ($J = 1$, $h_x = 0.5$, $h_z = 0$). Parameters: $N_s = 8$, $N_\tau = 101$, $N_{init} = 1000$, $T = 6$, $B_i = 5$, $B_f = 0.7$, $g_0 = 0.5$.

separately, highlighting the fact that domain walls are more difficult to remove.

5.3 Conclusion

We have proposed a simple, scalable cooling algorithm that prepares a low-energy state of an arbitrary gapped Hamiltonian on a programmable quantum computing platform. The steady state of the protocol approaches the ground state under the condition that adiabatic and Trotter errors are well controlled, and external noise is only weak. The protocol includes unitary time evolution and measurements. The non-unitary part in the form of the measurement and reset of the bath is essential to extract the entropy and effectively cool the system. While a reset alone is sufficient for the successful execution of the protocol, the measurement adds a complementary benefit. The information from the measurement can be used to make predictions about the system itself without a collapse of the system wave function. A continuous reduction of bath spin flips signals that the protocol is effective. Conditioning the end of the protocol on the measurement outcomes improves the fidelity of the resulting wave function.

The protocol works best if local operations can remove the excitation. To annihilate topological excitations, it is necessary to bring one or more excitations together at the same position. Therefore, the efficiency of the protocol scales nonlinearly with the noise level compared to linearly for local excitations. The "coolability" measure could detect topological phases in "quantum numerical" experiments on a quantum computer, which is usually challenging.

The protocol is quite noise resilient because of its cyclic property. Thus, implementing noisy quantum computers with a small number of qubits provides a great testing environment. Indeed, an execution of the cooling protocol on a five qubit system of the IBM cloud by Imane El Achchi already shows a cooling effect [P171]. Further quantum optimal control methods could provide a platform-tailored optimization concerning noise and speed while preserving a certain generality. With larger quantum computing capabilities, the protocol can explore unknown ground states and excitations of complex quantum many-body Hamiltonians in the future.

The protocol potentially provides several additional applications which may be explored in future works. For example, states at a finite target energy E_t could be prepared by alternately sweeping the magnetic field down and up to cool and heat the system to the energy E_t. Quantum many-body scar states have been proposed for quantum-enhanced metrological phase estimation. The scar states provide large multipartite entanglement that is long-lived. However, since the states have finite energy, an efficient state preparation protocol is needed and could be provided by heating and cooling the system. Furthermore, we discussed in the previous chapter that Floquet phases are prone to heat up to infinite temperatures in the presence of interactions. A potential generalization of the cooling protocol could counteract these heating effects and create more long-lived Floquet states.

Chapter 6

Programmable Adiabatic Demagnetization Implemented on Real Quantum Hardware

Recent advances in quantum computing provide a vast playground for the application of quantum algorithms on noisy intermediate-scale quantum devices. Platforms that are open to the public, like the IBM quantum cloud, make it possible to test quantum algorithms on real devices without ever entering an experimental lab. Here, we take this opportunity as theorists to gain experimental insights into the performance of the low-energy state preparation protocol of Chap. 5.

Inspired by adiabatic demagnetization, this protocol simulates the time evolution of a system coupled to a low-entropy bath, see Fig. 5.1 and 6.1. The bath qubits are subject to a simulated Zeeman field that is slowly decreased. Energy and entropy are transferred from the system to the bath during the sweep. In the end, the system and the bath are decoupled, the bath is measured and reset to its initial low-entropy state. The measurement and reset extract the energy and entropy and allow for a repetition of the protocol cycle.

Based on the numerical simulation, the cooling protocol shows noise resilience up to a threshold due to its cyclic property. Thus, we expect to observe a cooling effect in experiments on current noisy devices. However, the slow sweep of the parameters and the very small discretization of the time evolution in the previous study are more suited to an analog quantum simulator.

In this Chapter, we outline a strategy to implement the cooling protocol of Chap. 5 on a gate-based noisy quantum computer. The noise strongly limits the gate depth and requires further optimization of the protocol. Therefore, we transfer the slow sweep of the protocol parameters into a shallow quantum circuit. Furthermore, the simulated Zeeman field and the coupling strength between system and bath need to be optimized. For the available small system size, unsophisticated optimization is sufficient to experimentally observe a cooling effect. For the

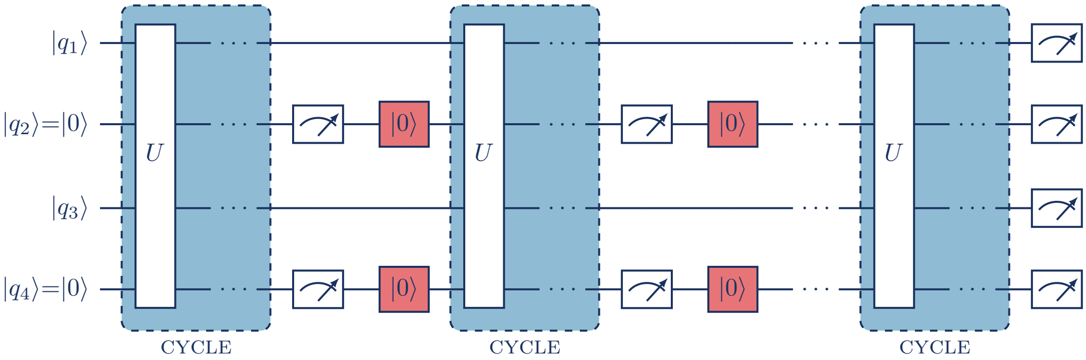

FIGURE 6.1: Schematic of the circuit implementation: The system is represented by the odd qubits $|q_{\text{odd}}\rangle$ and the bath by the even qubits, respectively. The bath qubits are initialized in the groundstate $|q_{\text{even}}\rangle = |0\rangle$. The time-evolution of the protocol cycle $U = \prod_n U_n$ is simulated by a Suzuki-Trotter decomposition for the gate representation of U_n see Fig. 6.2. After each cycle, the bath qubits are measured and reset to the $|0\rangle$ state. At the end of the protocol, all qubits are measured. This figure has been created with the help of Imane El Achchi.

future, we suggest to use quantum optimal control methods that do not limit the flexibility of the protocol to specific Hamiltonians.

This chapter is based on unpublished work in collaboration with Imane El Achchi, Mark Rudner, Erez Berg and Achim Rosch [P171]. As part of her Master's thesis, Imane El Achchi implemented the cooling protocol in qiskit [172] and obtained the results under my co-supervision.

6.1 Gate-based implementation

The cooling protocol consists of two parts – unitary time evolution U and measurements. $U = e^{-iH_{\text{tot}}t}$ simulates the system and the bath together, while only bath qubits are measured, see Fig. 6.1. The bath qubits (even qubit number in our notation) are initialized in the $|0\rangle$ state of the computational basis. Under the time evolution U, the system and bath become entangled and energy and entropy is absorbed by the bath qubits. To repeat the cycle again, the bath qubits are measured and reset $|q_{\text{even}}\rangle = |0\rangle$. In the end, all qubits are measured to calculate the expectation values of system observables. We apply the cooling protocol to the one dimensional quantum Ising model with a transverse field h_x, a longitudinal field h_z and the exchange interaction J. The total Hamiltonian yields

$$H(t_n) = -J \sum_{i=\text{odd}} s_i^z s_{i+2}^z - h_x \sum_{i=\text{odd}} s_i^x - h_z \sum_{i=\text{odd}} s_i^z - B(t_n) \sum_{i=\text{even}} s_i^z + g \sum_i s_i^y s_{i+1}^y, \tag{6.1}$$

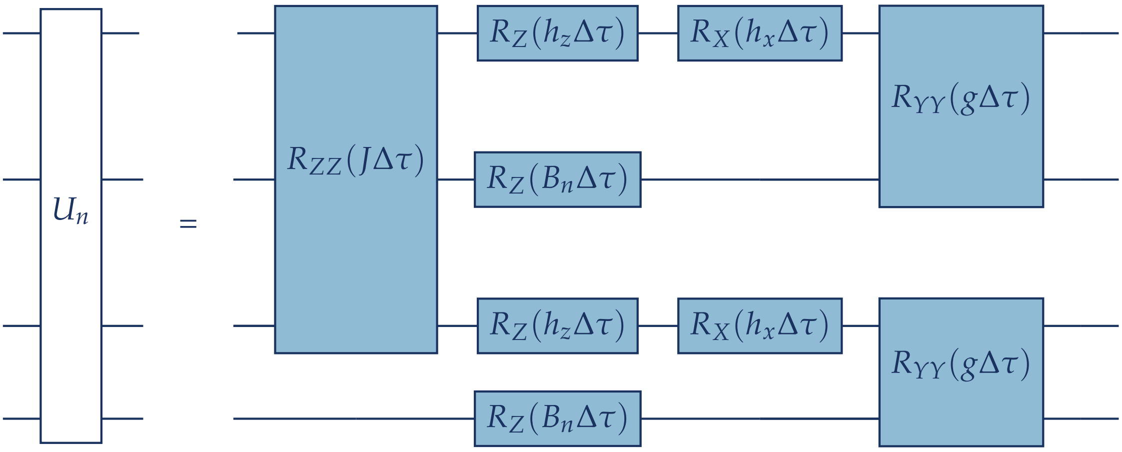

FIGURE 6.2: The full unitary evolution before the measurement is described by $U = \prod_n U_n$. Each unitary U_n of Eq. (6.2) consists of four layers, here, drawn for four qubits. The ZZ-rotation gate acts only on the two system qubits and simulates the spin exchange interaction. The Z-rotation gates, simulating magnetic fields, act on all qubits. While all other parameters are kept constant, the simulated Zeeman field acting on the bath qubits is decreased in discrete steps. The transverse field amounts to X-rotation gates acting on the system qubits. The YY-rotation gates entangle each system qubit with one bath qubit. This figure has been created with the help of Imane El Achchi.

where the system qubits are labels by $i =$ odd and bath qubits by $i =$ even. We consider only discrete values of magnetic field $B(t_n)$ acting on the bath qubits. In contrast to Chap. 5, we keep the coupling g between the system and the bath constant due to the small number of Trotter steps. Note that next-nearest-neighbour coupling is usually avoided because it introduces further qubit switching gate operations. Here, we assume that the geometry allows for a nearest-neighbour interaction implementation and the next-nearest neighbour interaction is just an artefact of our notation. To minimize the gate depth, we implement the time-evolution $U = \prod_n U$ using a Suzuki-Trotter decomposition up to the first order

$$U_n = e^{-i\Delta\tau H_{ZZ}(t_n)} e^{-i\Delta\tau H_Z(t_n)} e^{-i\Delta\tau H_X(t_n)} e^{-i\Delta\tau H_{YY}(t_n)}, \tag{6.2}$$

where $H_{\alpha(\beta)}$ corresponds to the term in the Hamiltonian of Eq. (6.1) with Pauli matrices s^α (and s^β). Each exponential corresponds to a rotation gate as sketched in Fig. 6.2. The circuit for each U_n consists, in principle, of five layers. The first unitary of Eq. (6.2) needs to be split in two parts because only a single operation on each qubit is allowed at once. The circuit is repeated for N_t Trotter steps until the measurement of the bath qubits.

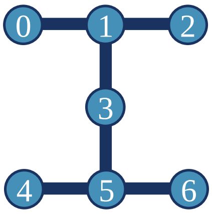

FIGURE 6.3: The experiments are performed on the ibm-oslo chip with the depicted qubit connectivity [173]. We use qubits 0, 1, 3, and 5, where qubits 0 and 5 simulate the bath and 1 and 3 the system, respectively.

6.2 Simulation on the IBM quantum chip

To apply the circuit on a quantum device, it has to be translated into the native gate set. The Qiskit software package offers an automatic compilation process [172]. For the IBM chips, the native gates are the controlled-x (CX or $CNOT$) gate, the identity gate (ID), the single-qubit z-rotation gate ($RZ = \exp(-i\theta Z/2)$), and the square-root NOT gate ($SX = \sqrt{X}$) and phase gate ($S = RZ(\pi/2)$). The $CNOT$ gate is the only two-qubit gate. Two qubit operations of Eq. (6.2) consist of two $CNOT$ operations. The $CNOT$-gates are particularly error prone with errors of the order of 10^{-2}. While we have performed a more detailed error analysis [P171], a simple calculation shows that only very few Trotter steps are possible. Each Trotter step, Eq. (6.2) and Fig. 6.2, consists of two layers of two-qubit operations, thus, a total of four $CNOT$-layers. Therefore, already three Trotter steps amount to an error of the order of 10^{-1}.

Three Trotter steps is much less than one hundred steps in our previous numerical simulations. We use Qiskit's noise model to approximate the noise in the real IBM device as a composition of depolarizing, thermal relaxation and readout errors which are based on device parameters obtained through calibration [172]. Using this noise simulator, we find well performing values B_n for the simulated Zeeman field and $n = 1 - 3$. The protocol performs best when the resonance condition is met, as expected from the analytical calculation, see Sec. 5.1.2 of the previous chapter. Therefore, we choose the three values around the resonance point $2B = \Delta$, where Δ is the energy gap of the system.

We test the protocol on the ibm-oslo chip using only four qubits, see Fig. 6.3. For larger devices with more complicated geometries, the protocol has to be adapted. Our results show a cooling effect, even in this noisy environment. The expectation value of the energy drops below the first excited state already after the first cycle. The mid-circuit measurements of the bath qubits also follows this behaviour.

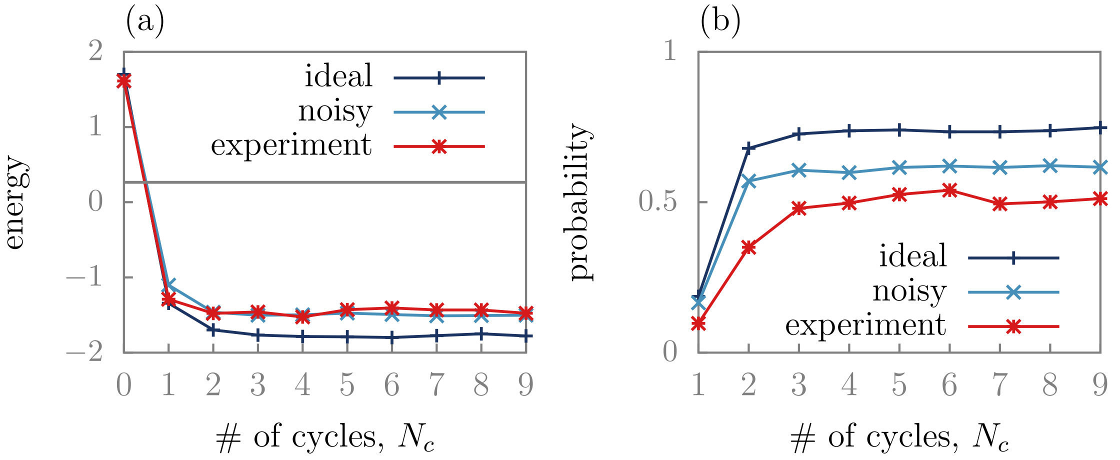

FIGURE 6.4: (a) After the first cycle, the expectation value of the system's energy has dropped below the first excited state (solid black line), and a steady state is reached. The numerical and experimental data has been obtained by Imane El Achchi using qiskit [172]. The experiments were performed on four qubits of the ibm-oslo chip on October 29th, 2022 (7:51 pm) with a median *CNOT* error of $7.62 \cdot 10^{-3}$ and a readout error of $2.29 \cdot 10^{-2}$. The expectation value of the energy is obtained by separate measurements in the x- and z-basis, each with 3000 shots. Parameters: $g = 0.5$, $J = 0.3$, $h_x = 0.2$, $h_z = 1$, $\Delta t = 0.1$, $N_t = 3$ Trotter steps in each cycle with $B_1 = 1.5$, $B_2 = 1.25$ and $B_3 = 1.0$. (b) The probability of finding the bath qubits in the $|00\rangle$ state by the mid-circuit measurements approaches a steady state. Here, the mid-circuit measurement results from the run with $N_c = 9$ cycles are displayed.

This result encourages adapting the implementation to bigger systems and more complex Hamiltonians. We expect that more sophisticated quantum optimal control methods [174, 175] are needed to maximise the cooling effect. Furthermore, error-mitigation techniques could improve the results [176]. In the next section, we expand on how one can use quantum optimal control to enhance the protocol while keeping its flexible and general usage.

6.3 Quantum optimal control

Quantum optimal control offers a powerful toolkit to steer a dynamical (open) system from an initial state to the desired target state [174, 177]. Controlled steering means that the desired accuracy can be achieved while optimal refers to the least effort and resources. Since current quantum simulators are well characterized but lack the accuracy due to noise, the operation of these devices is well suited for quantum optimal control [174]. Quantum optimal control methods have been applied, e.g., to quantum state preparation [175, 178–180] and qubit reset [181]. In a different setup of algorithmic cooling context, optimal control theory has been exploited to cool molecular vibrations [182].

In this section, we want to address the optimization of our cooling protocol from three perspectives. Inspired by the measurement induced quantum steering [183, 184], we discuss the approach of finding the dark state in the context of an open quantum system. Then, we outline how the protocol can be optimized by quantum optimal control methods by treating the Hamiltonian as a "black box". With few assumptions on the Hamiltonian we can keep the flexibility of the protocol.

Using the language of quantum channels, see Sec. 3.4, we can describe the evolution of the system for one protocol cycle as

$$\mathcal{E}(\rho) = \mathcal{E}_{\mathrm{mr}}\left(U\rho U^{\dagger}\right), \tag{6.3}$$

where the quantum channel $\mathcal{E}_{\mathrm{mr}}$ describes the measurement and reset of the bath qubits (see Eq. (3.55)) and U the unitary time evolution. This description has the advantage that once the quantum channel for a single cycle is known, the full evolution just reads

$$\mathcal{E}_{\mathrm{tot}} = \mathcal{E}^{N_c}, \tag{6.4}$$

where the single channel is applied N_c times. One can interpret this as a Floquet problem, not only in the unitary time-evolution due to the discrete gates, but also in terms of the Lindbladian. Then, the goal of this analysis is to find a dark state of the evoultion such that

$$\mathcal{E}^{N_c}(\rho_D) = \mathcal{E}(\rho_D) = \rho_D. \tag{6.5}$$

Thus, the system should evolve to state ρ_D which cannot be escaped once it is reached. For our purposes, ρ_D should describe the ground state or low-energy sector of the Hilbert space. In the end, the channel $\mathcal{E}$ has to be optimized such that the dark state is reached for small repetitions N_c.

Of course, not only the number of cycles, but even more importantly, the cycle itself can be optimized. Using different opimization methods, we can either optimize the combination of quantum gates or more drastically design the pulses applied on the qubits. The gate optimization could be implemented using a gradient-free method, while Krotov's method could tackle the optimization of the pulses itself [185]. Since we know that the protocol works in the adiabatic limit, we expect that the such an optimization protocol is able to find at least one solution, namely the adiabatic limit. Furthermore, given a desired accuracy, the shorter duration of the protocol would be of crucial benefit for the applications on noisy quantum platforms.

Now, optimizing the cooling protocol on a specific Hamiltonian would destroy the main advantage, namely, that it works for arbitrary gapped Hamiltonians. Instead, we can treat the Hamiltonian as a black box. For example, we can allow for random parameters J and h_x in the case of the transverse field Ising model

$$H(J_i, h_i^x) = -\sum J_i s_i^z s_{i+1}^z - \sum_i h_i^x s_i^x, \tag{6.6}$$

where J_i and h_i^x have been further generalized and made site dependent. Then, the cooling protocol can be optimized for a sufficient large number of realization of Eq. (6.6) with random parameters. This optimization procedure aims to produce a cooling protocol that works for all realization of the Hamiltonian, Eq. (6.6). We expect that this procedure can also be generalized to other Hamiltonians.

6.4 Conclusion

We successfully implemented the cooling protocol on the ibm-oslo quantum chip. The implementation is limited by the small number of qubits and Trotter steps, but we observe a cooling effect. We believe that the protocol will have an impact in the preparation of more complex states and bigger system sizes in the future. More work has to be done though to optimize for different chip geometries and for better accuracy. Quantum optimal control can provide a key tuning knob for a faster execution of the protocol. Using quantum optimal control in a general setup, the flexibility of the protocol can be preserved and the performance on noisy quantum devices can be increased.

Chapter 7

Conclusion and Outlook

In this thesis, we have explored the fascinating effects of non-equilibrium dynamics on novel qubits and quantum computing. Such effects are unavoidable, given the inherent open nature of operating a quantum computer, with, for example, noise and measurements playing a key role. On the other hand, this connection can be actively leveraged to explore new non-equilibrium phenomena and phases.

In Chap. 4, we investigated the building block of a quantum computer, a qubit, and showed how a Floquet drive can boost its capabilities. Due to the time-dependent drive, energy is not conserved anymore. Remarkably, the discrete time-translational symmetry brings Floquet systems as close to an equilibrium phase structure as possible, despite the system being highly out of equilibrium. As a result, states showing exciting new topological features can be long-lived.

More concretely, we investigated Majorana box qubits, which have been introduced as a promising building block of future topological quantum computers. We have demonstrated that one could triple the number of logical qubits using an oscillating gate voltage. However, a standard adiabatic state preparation leads to a highly unstable state. We showed that this instability is, in fact, a generic and fundamental problem of topological Floquet states in superconductors. We demonstrated how alternative preparation protocols can avoid this instability creating long-lived Floquet qubits in an interacting system.

Turning away from hardware design, in Chap. 5, we shifted the focus to one of the most promising applications of quantum computers. The simulation of quantum many-body systems requires precise state preparation techniques and the possibility to accurately time-evolve the system. However, precise quantum state preparation is extremely challenging, particularly on current noisy quantum hardware. This challenge is a major issue as ground state preparation is crucial for any near-term practical applications in the areas of quantum chemistry and materials science.

As a potential solution, we investigated how low-energy states of arbitrary gapped Hamiltonians can be prepared by a programmable cooling protocol on a quantum computer [P168]. The protocol is inspired by the adiabatic demagnetization technique, used to cool solid-state systems to extremely low temperatures. Unitary time evolution is combined with measurement and reset of the bath qubits. Key advantages of our protocol are that the performance is independent of the system's initial state and any knowledge about the target state. Furthermore, the engineered dissipation and cyclicity of the protocol make it more noise resilient as errors can be partially self-corrected, identifying it as a promising application for current quantum computers.

Early signs of the protocol's robustness against noise have already been demonstrated on current quantum hardware, as outlined in Chap. 6. To accomplish this, we translated the cooling protocol to a gate-based approach with as few gates as possible, to further reduce the effects of noise. Under my co-supervision, a Master's student implemented the gate-based protocol using Qiskit and performed experiments on the IBM quantum cloud. On the available small system size, we indeed observed a cooling effect. In the future, quantum optimal control and error mitigation techniques are needed to fully exploit the coolability.

Looking ahead, it's natural to think of a generalization of the cooling protocol that combines state preparation and Floquet dynamics. Driven systems generically heat up to infinite temperatures in the presence of interactions [186]. Heating is usually unavoidable in experiments since mechanisms like many-body localization and prethermalization are often unavailable or insufficient on the relevant time scales. As our cooling protocol prepares low-energy equilibrium states independently of the initial state and the nature of the target state, it can potentially be generalized to Floquet systems. For example, one could design a protocol to counteract the heating effects of driven interacting systems by exploiting the inherent tolerance of cooling protocols against noise and, thus, enhancing the lifetime of Floquet phases on near-term quantum computers.

Another application for the cooling protocol is the design of an efficient quantum algorithm for Gibbs sampling. Gibbs sampling is a method to calculate thermodynamic quantities by drawing states from a thermal distribution [90, 187]. Due to the memory overhead, near-term devices struggle with most Gibbs sampling methods. Interestingly, the low-energy states of our cooling protocol follow approximately a thermal distribution. Therefore, one could utilize the idea of programmable cooling to prepare thermal states with an effective temperature. By performing a measurement, states can be randomly drawn from the prepared thermal distribution and used for determining thermodynamic quantities or other quantum algorithms like quantum Boltzmann training [188]. It would be exciting to investigate the underlying thermalization process and the efficiency of the sampling.

Bibliography

P131. Matthies, A., Park, J., Berg, E. & Rosch, A. "Stability of Floquet Majorana Box Qubits". *Physical Review Letters* **128,** 127702 (2022).

P168. Matthies, A., Rudner, M., Rosch, A. & Berg, E. "Programmable adiabatic demagnetization for systems with trivial and topological excitations". *arXiv:2210.17256* (2022).

P171. El Achchi, I., Matthies, A., Rosch, A., Rudner, M. & Berg, E. *Programmable cooling on noisy quantum computers: Implementation and error analysis.* (unpublished).

1. Schrödinger, E. & Penrose, R. *What is Life?* ISBN: 9781139644129 (Cambridge University Press, 1992).
2. Jarzynski, C. "Diverse phenomena, common themes". *Nature Physics* **11,** 105–107 (2015).
3. Eisert, J., Friesdorf, M. & Gogolin, C. "Quantum many-body systems out of equilibrium". *Nature Physics* **11,** 124–130 (2015).
4. Cirac, J. I. & Zoller, P. "Goals and opportunities in quantum simulation". *Nature Physics* **8,** 264–266 (2012).
5. Preskill, J. "Quantum Computing in the NISQ era and beyond". *Quantum* **2,** 79 (2018).
6. Frey, P. & Rachel, S. "Realization of a discrete time crystal on 57 qubits of a quantum computer". *Science Advances* **8,** eabm7652 (2022).
7. Fisher, M. P., Khemani, V., Nahum, A. & Vijay, S. "Random Quantum Circuits". *Annual Review of Condensed Matter Physics* **14,** 335–379. ISSN: 1947-5462 (2023).
8. Daley, A. J. *et al.* "Practical quantum advantage in quantum simulation". *Nature* **607,** 667–676 (2022).
9. Oka, T. & Kitamura, S. "Floquet Engineering of Quantum Materials". *Annual Review of Condensed Matter Physics* **10,** 387–408 (2019).

10. Harper, F., Roy, R., Rudner, M. S. & Sondhi, S. "Topology and Broken Symmetry in Floquet Systems". *Annual Review of Condensed Matter Physics* **11,** 345–368 (2020).
11. Rudner, M. S. & Lindner, N. H. "Band structure engineering and non-equilibrium dynamics in Floquet topological insulators". *Nature Reviews Physics* **2,** 229–244 (2020).
12. Kapit, E. "The upside of noise: engineered dissipation as a resource in superconducting circuits". *Quantum Science and Technology* **2,** 033002 (2017).
13. Harrington, P. M., Mueller, E. J. & Murch, K. W. "Engineered dissipation for quantum information science". *Nature Reviews Physics* **4,** 660–671 (2022).
14. Satzinger, K. J. *et al.* "Realizing topologically ordered states on a quantum processor". *Science* **374,** 1237–1241 (2021).
15. Semeghini, G. *et al.* "Probing topological spin liquids on a programmable quantum simulator". *Science* **374,** 1242–1247 (2021).
16. Ippoliti, M., Kechedzhi, K., Moessner, R., Sondhi, S. & Khemani, V. "Many-Body Physics in the NISQ Era: Quantum Programming a Discrete Time Crystal". *Physical Review X Quantum* **2,** 030346 (2021).
17. Floquet, G. "Sur les équations différentielles linéaires à coefficients périodiques". *Annales scientifiques de l'École normale supérieure* **12,** 47–88 (1883).
18. DiVincenzo, D. P. "The Physical Implementation of Quantum Computation". *Fortschritte der Physik* **48,** 771–783 (2000).
19. Arute, F. *et al.* "Quantum supremacy using a programmable superconducting processor". *Nature* **574,** 505–510. ISSN: 1476-4687 (2019).
20. Devitt, S. J., Munro, W. J. & Nemoto, K. "Quantum error correction for beginners". *Reports on Progress in Physics* **76,** 076001. ISSN: 1361-6633 (2013).
21. Kitaev, A. "Fault-tolerant quantum computation by anyons". *Annals of Physics* **303,** 2–30 (2003).
22. Pachos, J. K. *Introduction to Topological Quantum Computation*. ISBN: 9780511792908 (Cambridge University Press, 2012).
23. Nielsen, M. A. & Chuang, I. L. *Quantum computation and quantum information - 10. ed.* ISBN: 9781107002173 (Cambridge University Press, 2010).
24. Deutsch, D. "Quantum theory, the Church–Turing principle and the universal quantum computer". *Proceedings of the Royal Society of London. A. Mathematical and Physical Sciences* **400,** 97–117 (1985).

25. Feynman, R. P. in *Feynman and computation* 133–153 (CRC Press, 2018).
26. Shor, P. *Algorithms for quantum computation: discrete logarithms and factoring*. in *Proceedings 35th Annual Symposium on Foundations of Computer Science* (IEEE Comput. Soc. Press, 1994).
27. Lanyon, B. P. *et al.* "Experimental Demonstration of a Compiled Version of Shor's Algorithm with Quantum Entanglement". *Physical Review Letters* **99,** 250505 (2007).
28. Lu, C.-Y., Browne, D. E., Yang, T. & Pan, J.-W. "Demonstration of a Compiled Version of Shor's Quantum Factoring Algorithm Using Photonic Qubits". *Physical Review Letters* **99,** 250504 (2007).
29. Martín-López, E. *et al.* "Experimental realization of Shor's quantum factoring algorithm using qubit recycling". *Nature Photonics* **6,** 773–776 (2012).
30. Lucero, E. *et al.* "Computing prime factors with a Josephson phase qubit quantum processor". *Nature Physics* **8,** 719–723 (2012).
31. De Wolf, R. "The potential impact of quantum computers on society". *Ethics and Information Technology* **19,** 271–276 (2017).
32. Preskill, J. in *Feynman Lectures on Computation* 193–244 (CRC Press, 2023). ISBN: 9781003358817.
33. Cottet, A. *Implementation of a quantum bit in a superconducting cirucit.* PhD thesis (Universite Paris VI, 2002).
34. Devoret, M. H., Wallraff, A. & Martinis, J. M. "Superconducting Qubits: A Short Review". *arXiv:cond-mat/0411174* (2004).
35. Vool, U. & Devoret, M. "Introduction to quantum electromagnetic circuits". *International Journal of Circuit Theory and Applications* **45,** 897–934 (2017).
36. Devoret, M. H. & Schoelkopf, R. J. "Superconducting Circuits for Quantum Information: An Outlook". *Science* **339,** 1169–1174 (2013).
37. Devoret, M. H. & Martinis, J. M. "Implementing Qubits with Superconducting Integrated Circuits". *Quantum Information Processing* **3,** 163–203 (2004).
38. Clarke, J. & Wilhelm, F. K. "Superconducting quantum bits". *Nature* **453,** 1031–1042 (2008).
39. Nakamura, Y., Pashkin, Y. A. & Tsai, J. S. "Coherent control of macroscopic quantum states in a single-Cooper-pair box". *Nature* **398,** 786–788 (1999).

40. Jens Koch and Terri M. Yu and Jay Gambetta and A. A. Houck and D. I. Schuster and J. Majer and Alexandre Blais and M. H. Devoret and S. M. Girvin and R. J. Schoelkopf. "Charge-insensitive qubit design derived from the Cooper pair box". *Physical Review A* **76,** 042319 (2007).
41. Akhmerov, A. *et al. Online course on topology in condensed matter.* Accessed on 03/03/2023. `https://topocondmat.org/`.
42. Alicea, J. "New directions in the pursuit of Majorana fermions in solid state systems". *Reports on Progress in Physics* **75,** 076501 (2012).
43. Leijnse, M. & Flensberg, K. "Introduction to topological superconductivity and Majorana fermions". *Semiconductor Science and Technology* **27,** 124003 (2012).
44. Elliott, S. R. & Franz, M. "Colloquium: Majorana fermions in nuclear, particle, and solid-state physics". *Reviews of Modern Physics* **87,** 137–163 (2015).
45. Mbeng, G. B., Russomanno, A. & Santoro, G. E. "The quantum Ising chain for beginners". *arxiv:2009.09208* (2020).
46. Plugge, S., Rasmussen, A., Egger, R. & Flensberg, K. "Majorana box qubits". *New Journal of Physics* **19,** 012001 (2017).
47. Kitaev, A. Y. "Unpaired Majorana fermions in quantum wires". *Phys. Usp.* **44,** 131–136 (2001).
48. Taroni, A. "90 years of the Ising model". *Nature Physics* **11,** 997–997 (2015).
49. Ivanov, D. A. "Non-Abelian Statistics of Half-Quantum Vortices in p-Wave Superconductors". *Physical Review Letters* **86,** 268–271 (2001).
50. Read, N. & Green, D. "Paired states of fermions in two dimensions with breaking of parity and time-reversal symmetries and the fractional quantum Hall effect". *Physical Review B* **61,** 10267–10297 (2000).
51. Fu, L. & Kane, C. L. "Superconducting Proximity Effect and Majorana Fermions at the Surface of a Topological Insulator". *Physical Review Letters* **100,** 096407 (2008).
52. Alicea, J. "Majorana fermions in a tunable semiconductor device". *Physical Review B* **81,** 125318 (2010).
53. Oreg, Y., Refael, G. & von Oppen, F. "Helical Liquids and Majorana Bound States in Quantum Wires". *Physical Review Letters* **105,** 177002 (2010).
54. Lutchyn, R. M., Sau, J. D. & Das Sarma, S. "Majorana Fermions and a Topological Phase Transition in Semiconductor-Superconductor Heterostructures". *Physical Review Letters* **105,** 077001 (2010).

55. Brouwer, P. W., Duckheim, M., Romito, A. & von Oppen, F. "Topological superconducting phases in disordered quantum wires with strong spin-orbit coupling". *Physical Review B* **84,** 144526 (2011).
56. Manousakis, J., Altland, A., Bagrets, D., Egger, R. & Ando, Y. "Majorana qubits in a topological insulator nanoribbon architecture". *Physical Review B* **95,** 165424 (2017).
57. Lutchyn, R. M. *et al.* "Majorana zero modes in superconductor–semiconductor heterostructures". *Nature Reviews Materials* **3,** 52–68 (2018).
58. Flensberg, K., von Oppen, F. & Stern, A. "Engineered platforms for topological superconductivity and Majorana zero modes". *Nature Reviews Materials* **6,** 944–958 (2021).
59. Karzig, T. *et al.* "Scalable designs for quasiparticle-poisoning-protected topological quantum computation with Majorana zero modes". *Physical Review B* **95,** 235305 (2017).
60. Vijay, S. & Fu, L. "Teleportation-based quantum information processing with Majorana zero modes". *Physical Review B* **94,** 235446 (2016).
61. McArdle, S., Endo, S., Aspuru-Guzik, A., Benjamin, S. C. & Yuan, X. "Quantum computational chemistry". *Reviews of Modern Physics* **92,** 015003 (2020).
62. Bauer, B., Bravyi, S., Motta, M. & Chan, G. K.-L. "Quantum Algorithms for Quantum Chemistry and Quantum Materials Science". *Chemical Reviews* **120,** 12685–12717 (2020).
63. Alexeev, Y. *et al.* "Quantum Computer Systems for Scientific Discovery". *Physical Review X Quantum* **2,** 017001 (2021).
64. McClean, J. R., Romero, J., Babbush, R. & Aspuru-Guzik, A. "The theory of variational hybrid quantum-classical algorithms". *New Journal of Physics* **18,** 023023 (2016).
65. Yuan, X., Endo, S., Zhao, Q., Li, Y. & Benjamin, S. C. "Theory of variational quantum simulation". *Quantum* **3,** 191 (2019).
66. Albash, T. & Lidar, D. A. "Adiabatic quantum computation". *Reviews of Modern Physics* **90,** 015002 (2018).
67. Childs, A. M. *Lecture notes on quantum algorithms.* Lecture Notes accessed on 06/03/2023 online. `http://www.cs.umd.edu/~amchilds/qa/qa.pdf`.
68. Polla, S., Herasymenko, Y. & O'Brien, T. E. "Quantum digital cooling". *Physical Review A* **104,** 012414 (2021).

69. Lloyd, S. "Universal Quantum Simulators". *Science* **273,** 1073–1078 (1996).
70. Reiher, M., Wiebe, N., Svore, K. M., Wecker, D. & Troyer, M. "Elucidating reaction mechanisms on quantum computers". *Proceedings of the National Academy of Sciences* **114,** 7555–7560 (2017).
71. Babbush, R. *et al.* "Low-Depth Quantum Simulation of Materials". *Physical Review X* **8,** 011044 (2018).
72. Bharti, K. *et al.* "Noisy intermediate-scale quantum algorithms". *Reviews of Modern Physics* **94,** 015004 (2022).
73. Helgaker, T. *et al.* "Recent Advances in Wave Function-Based Methods of Molecular-Property Calculations". *Chemical Reviews* **112,** 543–631 (2012).
74. Farhi, E., Goldstone, J. & Gutmann, S. "A Quantum Approximate Optimization Algorithm". *arXiv:1411.4028* (2014).
75. Oliveira, R. & Terhal, B. "The complexity of quantum spin systems on a two-dimensional square lattice". *Quantum Information and Computation* **8,** 900–924 (2008).
76. Lee, S. *et al.* "Evaluating the evidence for exponential quantum advantage in ground-state quantum chemistry". *Nature Communications* **14,** 1952. ISSN: 2041-1723 (2023).
77. Peruzzo, A. *et al.* "A variational eigenvalue solver on a photonic quantum processor". *Nature Communications* **5,** 4213 (2014).
78. Wecker, D., Hastings, M. B. & Troyer, M. "Progress towards practical quantum variational algorithms". *Physical Review A* **92,** 042303 (2015).
79. Cerezo, M. *et al.* "Variational quantum algorithms". *Nature Reviews Physics* **3,** 625–644 (2021).
80. Tilly, J. *et al.* "The Variational Quantum Eigensolver: A review of methods and best practices". *Physics Reports* **986,** 1–128 (2022).
81. Fedorov, D. A., Peng, B., Govind, N. & Alexeev, Y. "VQE method: a short survey and recent developments". *Materials Theory* **6,** 2 (2022).
82. Farhi, E., Goldstone, J., Gutmann, S. & Sipser, M. "Quantum Computation by Adiabatic Evolution". *arXiv:quant-ph/0001106* (2000).
83. Childs, A. M., Farhi, E. & Preskill, J. "Robustness of adiabatic quantum computation". *Physical Review A* **65,** 012322 (2001).
84. Aspuru-Guzik, A., Dutoi, A. D., Love, P. J. & Head-Gordon, M. "Simulated Quantum Computation of Molecular Energies". *Science* **309,** 1704–1707 (2005).

85. Boykin, P. O., Mor, T., Roychowdhury, V., Vatan, F. & Vrijen, R. "Algorithmic cooling and scalable NMR quantum computers". *Proceedings of the National Academy of Sciences* **99,** 3388–3393 (2002).

86. Kaplan, D. B., Klco, N. & Roggero, A. "Ground States via Spectral Combing on a Quantum Computer". *arXiv:1709.08250* (2017).

87. Wang, H. "Quantum algorithm for preparing the ground state of a system via resonance transition". *Scientific Reports* **7,** 16342 (2017).

88. Feng, J.-J., Wu, B. & Wilczek, F. "Quantum Computing by Coherent Cooling". *Physical Review A* **105,** 052601 (2022).

89. Zaletel, M. P., Kaufman, A., Stamper-Kurn, D. M. & Yao, N. Y. "Preparation of Low Entropy Correlated Many-Body States via Conformal Cooling Quenches". *Physical Review Letters* **126,** 103401 (2021).

90. Metcalf, M., Moussa, J. E., de Jong, W. A. & Sarovar, M. "Engineered thermalization and cooling of quantum many-body systems". *Physical Review Research* **2,** 023214 (2020).

91. Tranter, A., Love, P. J., Mintert, F. & Coveney, P. V. "A Comparison of the Bravyi–Kitaev and Jordan–Wigner Transformations for the Quantum Simulation of Quantum Chemistry". *Journal of Chemical Theory and Computation* **14,** 5617–5630 (2018).

92. Aharonov, D. *et al.* "Adiabatic Quantum Computation is Equivalent to Standard Quantum Computation". *SIAM Journal on Computing* **37,** 166–194 (2007).

93. Jansen, S., Ruskai, M.-B. & Seiler, R. "Bounds for the adiabatic approximation with applications to quantum computation". *Journal of Mathematical Physics* **48,** 102111 (2007).

94. Elgart, A. & Hagedorn, G. A. "A note on the switching adiabatic theorem". *Journal of Mathematical Physics* **53,** 102202 (2012).

95. Latorre, J. I. & Orús, R. "Adiabatic quantum computation and quantum phase transitions". *Physical Review A* **69,** 062302 (2004).

96. Lieb, E. H. & Robinson, D. W. "The finite group velocity of quantum spin systems". *Communications in Mathematical Physics* **28,** 251–257 (1972).

97. Cheneau, M. *et al.* "Light-cone-like spreading of correlations in a quantum many-body system". *Nature* **481,** 484–487 (2012).

98. Bravyi, S., Hastings, M. B. & Verstraete, F. "Lieb-Robinson Bounds and the Generation of Correlations and Topological Quantum Order". *Physical Review Letters* **97,** 050401 (2006).

99. Levin, M. A. & Wen, X.-G. "String-net condensation: A physical mechanism for topological phases". *Physical Review B* **71,** 045110 (2005).
100. Bolt, A., Duclos-Cianci, G., Poulin, D. & Stace, T. "Foliated Quantum Error-Correcting Codes". *Physical Review Letters* **117,** 070501 (2016).
101. Shi, B. "Seeing topological entanglement through the information convex". *Physical Review Research* **1,** 033048 (2019).
102. Verresen, R., Tantivasadakarn, N. & Vishwanath, A. "Efficiently preparing Schrödinger's cat, fractons and non-Abelian topological order in quantum devices". *arXiv:2112.03061* (2021).
103. Tantivasadakarn, N., Thorngren, R., Vishwanath, A. & Verresen, R. "Long-range entanglement from measuring symmetry-protected topological phases". *arXiv:2112.01519* (2021).
104. Tantivasadakarn, N., Vishwanath, A. & Verresen, R. "Hierarchy of Topological Order From Finite-Depth Unitaries, Measurement, and Feedforward". *PRX Quantum* **4,** 020339. ISSN: 2691-3399 (2023).
105. Lu, T.-C., Lessa, L. A., Kim, I. H. & Hsieh, T. H. "Measurement as a shortcut to long-range entangled quantum matter". *arXiv:2206.13527* (2022).
106. Rudner, M. S. & Lindner, N. H. "The Floquet Engineer's Handbook". *arXiv:2003.08252* (2020).
107. Cayssol, J., Dóra, B., Simon, F. & Moessner, R. "Floquet topological insulators". *physica status solidi (RRL) - Rapid Research Letters* **7,** 101–108 (2013).
108. Bukov, M., D'Alessio, L. & Polkovnikov, A. "Universal high-frequency behavior of periodically driven systems: from dynamical stabilization to Floquet engineering". *Advances in Physics* **64,** 139–226 (2015).
109. Moessner, R. & Sondhi, S. L. "Equilibration and order in quantum Floquet matter". *Nature Physics* **13,** 424–428 (2017).
110. Eckardt, A. "Colloquium: Atomic quantum gases in periodically driven optical lattices". *Reviews of Modern Physics* **89,** 011004 (2017).
111. Cooper, N., Dalibard, J. & Spielman, I. "Topological bands for ultracold atoms". *Reviews of Modern Physics* **91,** 015005 (2019).
112. Hatano, N. & Suzuki, M. in *Quantum Annealing and Other Optimization Methods* 37–68 (Springer Berlin Heidelberg, 2005). ISBN: 9783540315155.
113. Lazarides, A., Das, A. & Moessner, R. "Periodic Thermodynamics of Isolated Quantum Systems". *Physical Review Letters* **112,** 150401 (2014).

114. Lazarides, A., Das, A. & Moessner, R. "Fate of Many-Body Localization Under Periodic Driving". *Physical Review Letters* **115,** 030402 (2015).

115. Abanin, D. A., Roeck, W. D. & Huveneers, F. "Theory of many-body localization in periodically driven systems". *Annals of Physics* **372,** 1–11 (2016).

116. Ponte, P., Papić, Z., Huveneers, F. & Abanin, D. A. "Many-Body Localization in Periodically Driven Systems". *Physical Review Letters* **114,** 140401 (2015).

117. Jiang, L. *et al.* "Majorana Fermions in Equilibrium and in Driven Cold-Atom Quantum Wires". *Physical Review Letters* **106,** 220402 (2011).

118. Bauer, B. *et al.* "Topologically protected braiding in a single wire using Floquet Majorana modes". *Physical Review B* **100,** 041102(R) (2019).

119. Bilitewski, T. & Cooper, N. R. "Scattering theory for Floquet-Bloch states". *Physical Review A* **91,** 033601 (2015).

120. Oka, T. & Aoki, H. "Photovoltaic Hall effect in graphene". *Physical Review B* **79,** 081406 (2009).

121. Kitagawa, T., Berg, E., Rudner, M. & Demler, E. "Topological characterization of periodically driven quantum systems". *Physical Review B* **82,** 235114 (2010).

122. Lindner, N. H., Refael, G. & Galitski, V. "Floquet topological insulator in semiconductor quantum wells". *Nature Physics* **7,** 490–495 (2011).

123. Else, D. V. & Nayak, C. "Classification of topological phases in periodically driven interacting systems". *Physical Review B* **93,** 201103(R) (2016).

124. Else, D. V., Bauer, B. & Nayak, C. "Floquet Time Crystals". *Physical Review Letters* **117,** 090402 (2016).

125. Quelle, A, Weitenberg, C, Sengstock, K & Smith, C. M. "Driving protocol for a Floquet topological phase without static counterpart". *New Journal of Physics* **19,** 113010 (2017).

126. Maczewsky, L. J., Zeuner, J. M., Nolte, S. & Szameit, A. "Observation of photonic anomalous Floquet topological insulators". *Nature Communications* **8,** 13756 (2017).

127. Cheng, Q. *et al.* "Observation of Anomalous Pi Modes in Photonic Floquet Engineering". *Physical Review Letters* **122,** 173901 (2019).

128. Wintersperger, K. *et al.* "Realization of an anomalous Floquet topological system with ultracold atoms". *Nature Physics* **16,** 1058–1063 (2020).

129. Liu, D. E., Levchenko, A. & Baranger, H. U. "Floquet Majorana Fermions for Topological Qubits in Superconducting Devices and Cold-Atom Systems". *Physical Review Letters* **111,** 047002 (2013).
130. Kundu, A. & Seradjeh, B. "Transport Signatures of Floquet Majorana Fermions in Driven Topological Superconductors". *Physical Review Letters* **111,** 136402 (2013).
132. Callen, H. B. & Welton, T. A. "Irreversibility and Generalized Noise". *Physical Review* **83,** 34–40 (1951).
133. Kubo, R. "The fluctuation-dissipation theorem". *Reports on Progress in Physics* **29,** 255–284 (1966).
134. Hänggi, P. & Ingold, G.-L. "Fundamental aspects of quantum Brownian motion". *Chaos: An Interdisciplinary Journal of Nonlinear Science* **15,** 026105 (2005).
135. Seifert, U. & Speck, T. "Fluctuation-dissipation theorem in nonequilibrium steady states". *EPL (Europhysics Letters)* **89,** 10007 (2010).
136. Preskill, J. *Quantum Information, Chapter 3*. Lecture Notes accessed on 03/03/2023 online. `http://theory.caltech.edu/~preskill/ph219/chap3_15.pdf`.
137. Childress, L. & Lukin, M. D. *Modern Atomic and Optical Physics II*. Lecture Notes accessed 03/03/2023 online. `https://lukin.physics.harvard.edu/files/lukin/files/physics_285b_lecture_notes.pdf`.
138. Aharonov, Y. & Vaidman, L. "Measurement of the Schrödinger wave of a single particle". *Physics Letters A* **178,** 38–42 (1993).
139. Aharonov, Y., Anandan, J. & Vaidman, L. "The meaning of protective measurements". *Foundations of Physics* **26,** 117–126 (1996).
140. Bub, J. in *John von Neumann and the Foundations of Quantum Physics* (eds Rédei, M. & Stöltzner, M.) 63–74 (Springer Netherlands, Dordrecht, 2001). ISBN: 978-94-017-2012-0.
141. Clerk, A. A., Devoret, M. H., Girvin, S. M., Marquardt, F. & Schoelkopf, R. J. "Introduction to quantum noise, measurement, and amplification". *Reviews of Modern Physics* **82,** 1155–1208 (2010).
142. Svensson, B. E. Y. "Pedagogical Review of Quantum Measurement Theory with an Emphasis on Weak Measurements". *Quanta* **2,** 18 (2013).

143. Kofman, A. G., Ashhab, S. & Nori, F. "Nonperturbative theory of weak pre- and post-selected measurements". *Physics Reports* **520,** 43–133 (2012).
144. Schlosshauer, M. "Protective measurement of a qubit by a qubit probe". *Physical Review A* **101,** 042113 (2020).
145. Ting, J. J.-L. "Noise effects for the depolarizing channel". *Physics Letters A* **259,** 349–354 (1999).
146. Dür, W., Hein, M., Cirac, J. I. & Briegel, H.-J. "Standard forms of noisy quantum operations via depolarization". *Physical Review A* **72,** 052326 (2005).
147. Daffer, S., Wódkiewicz, K., Cresser, J. D. & McIver, J. K. "Depolarizing channel as a completely positive map with memory". *Physical Review A* **70,** 010304 (2004).
148. Pastawski, F., Kay, A., Schuch, N. & Cirac, I. "How Long Can a Quantum Memory Withstand Depolarizing Noise?" *Physical Review Letters* **103,** 080501 (2009).
149. Urbanek, M. *et al.* "Mitigating Depolarizing Noise on Quantum Computers with Noise-Estimation Circuits". *Physical Review Letters* **127,** 270502 (2021).
150. Dür, W & Briegel, H. J. "Entanglement purification and quantum error correction". *Reports on Progress in Physics* **70,** 1381–1424 (2007).
151. Li, Y., Kundu, A., Zhong, F. & Seradjeh, B. "Tunable Floquet Majorana fermions in driven coupled quantum dots". *Physical Review B* **90,** 121401(R) (2014).
152. Liu, D. T., Shabani, J. & Mitra, A. "Floquet Majorana zero and π modes in planar Josephson junctions". *Physical Review B* **99,** 094303 (2019).
153. Peng, C., Haim, A., Karzig, T., Peng, Y. & Refael, G. "Floquet Majorana bound states in voltage-biased planar Josephson junctions". *Physical Review Research* **3,** 023108 (2021).
154. Peng, Y. & Refael, G. "Time-quasiperiodic topological superconductors with Majorana multiplexing". *Physical Review B* **98,** 220509 (2018).
155. Bomantara, R. W. & Gong, J. "Measurement-only quantum computation with Floquet Majorana corner modes". *Physical Review B* **101,** 085401 (2020).
156. Seetharam, K. I., Bardyn, C.-E., Lindner, N. H., Rudner, M. S. & Refael, G. "Controlled Population of Floquet-Bloch States via Coupling to Bose and Fermi Baths". *Physical Review X* **5,** 041050 (2015).
157. Genske, M. & Rosch, A. "Floquet-Boltzmann equation for periodically driven Fermi systems". *Physical Review A* **92,** 062108 (2015).

158. Polkovnikov, A. "Universal adiabatic dynamics in the vicinity of a quantum critical point". *Physical Review B* **72,** 161201 (2005).
159. Zurek, W. H., Dorner, U. & Zoller, P. "Dynamics of a Quantum Phase Transition". *Physical Review Letters* **95,** 105701 (2005).
160. Damski, B. "The Simplest Quantum Model Supporting the Kibble-Zurek Mechanism of Topological Defect Production: Landau-Zener Transitions from a New Perspective". *Physical Review Letters* **95,** 035701 (2005).
161. Dziarmaga, J. "Dynamics of a Quantum Phase Transition: Exact Solution of the Quantum Ising Model". *Physical Review Letters* **95,** 245701 (2005).
162. Bomantara, R. W. & Gong, J. "Simulation of Non-Abelian Braiding in Majorana Time Crystals". *Physical Review Letters* **120,** 230405 (2018).
163. Cao, Y. *et al.* "Quantum Chemistry in the Age of Quantum Computing". *Chemical Reviews* **119,** 10856–10915 (2019).
164. Biamonte, J. *et al.* "Quantum machine learning". *Nature* **549,** 195–202 (2017).
165. Montanaro, A. "Quantum algorithms: an overview". *npj Quantum Information* **2,** 15023. ISSN: 2056-6387 (2016).
166. Debye, P. "Einige Bemerkungen zur Magnetisierung bei tiefer Temperatur". *Annalen der Physik* **386,** 1154–1160 (1926).
167. Giauque, W. F. "A Thermodynamic Treatment of Certain Magnetic Effects. A Proposed Method of Producing Temperatures Considerably Below 1°Absolute". *Journal of the American Chemical Society* **49,** 1864–1870 (1927).
169. Cao, H. "Refrigeration Below 1 Kelvin". *Journal of Low Temperature Physics* **204,** 175–205 (2021).
170. Jones, A. T. *et al.* "Progress in Cooling Nanoelectronic Devices to Ultra-Low Temperatures". *Journal of Low Temperature Physics* **201,** 772–802 (2020).
172. Qiskit contributors. *Qiskit: An Open-source Framework for Quantum Computing*. 2023.
173. IBM Quantum. *https://quantum-computing.ibm.com/*.
174. Koch, C. P. "Controlling open quantum systems: tools, achievements, and limitations". *Journal of Physics: Condensed Matter* **28,** 213001 (2016).
175. Doria, P., Calarco, T. & Montangero, S. "Optimal Control Technique for Many-Body Quantum Dynamics". *Physical Review Letters* **106,** 190501 (2011).
176. Cai, Z. *et al.* "Quantum error mitigation". *Reviews of Modern Physics* **95,** 045005. ISSN: 1539-0756 (2023).

177. Glaser, S. J. *et al.* "Training Schrödinger's cat: quantum optimal control". *The European Physical Journal D* **69,** 279 (2015).
178. Grond, J., Schmiedmayer, J. & Hohenester, U. "Optimizing number squeezing when splitting a mesoscopic condensate". *Physical Review A* **79,** 021603 (2009).
179. Wang, X., Bayat, A., Bose, S. & Schirmer, S. G. "Global control methods for Greenberger-Horne-Zeilinger-state generation on a one-dimensional Ising chain". *Physical Review A* **82,** 012330 (2010).
180. Rojan, K. *et al.* "Arbitrary-quantum-state preparation of a harmonic oscillator via optimal control". *Physical Review A* **90,** 023824 (2014).
181. Reich, D. M. & Koch, C. P. "Cooling molecular vibrations with shaped laser pulses: optimal control theory exploiting the timescale separation between coherent excitation and spontaneous emission". *New Journal of Physics* **15,** 125028 (2013).
182. Basilewitsch, D. *et al.* "Reservoir engineering using quantum optimal control for qubit reset". *New Journal of Physics* **21,** 093054 (2019).
183. Roy, S., Chalker, J. T., Gornyi, I. V. & Gefen, Y. "Measurement-induced steering of quantum systems". *Physical Review Research* **2,** 033347 (2020).
184. Kumar, P., Snizhko, K., Gefen, Y. & Rosenow, B. "Optimized steering: Quantum state engineering and exceptional points". *Physical Review A* **105,** l010203 (2022).
185. Goerz, M. *et al.* "Krotov: A Python implementation of Krotov's method for quantum optimal control". *SciPost Physics* **7,** 080 (2019).
186. Lazarides, A., Das, A. & Moessner, R. "Equilibrium states of generic quantum systems subject to periodic driving". *Physical Review E* **90,** 012110 (2014).
187. Poulin, D. & Wocjan, P. "Sampling from the Thermal Quantum Gibbs State and Evaluating Partition Functions with a Quantum Computer". *Physical Review Letters* **103,** 220502 (2009).
188. Wang, Y., Li, G. & Wang, X. "Variational Quantum Gibbs State Preparation with a Truncated Taylor Series". *Physical Review Applied* **16,** 054035. ISSN: 2331-7019 (2021).

Acknowledgements

First and foremost, I would like to thank my supervisor Achim Rosch for his advice and outstanding support. Thank you for the inspiring physics discussions, always having an open ear for me, and opening up so many opportunities.

I would also like to thank Erez Berg, a wonderful host, and short-term supervisor, during my six-month stay at the Weizmann Institute. Thank you for the fun physics and helpful advice! Many thanks to Mark Rudner for the excellent collaboration and insightful discussion on the project that started during my Weizmann stay.

I want to thank Simon Trebst for his support and advice as a member of my thesis advisory committee and for reading and grading the thesis. I would also like to thank Erwann Bocquillon who is the third examiner and head of the thesis committee.

Special thanks also to Karin Everschor-Sitte, who was a great mentor. I appreciate that you shared so many valuable experiences and that I could always reach out to you.

I want to thank the many readers of the manuscript draft – Alla Bezvershenko, Annika Landskron, Aprem Joy, Bastian Matthies, Christoph Berke, Ciarán Hickey, Gilad Kishony, Hanna Matthies, Michael Buchhold, Monika Matthies, Nina del Ser, Petr Zapletal, Rüdiger Pupke, Silvana Burger, and Vanessa Schäfer.

Many thanks to all the Rosch group members! Working in such a kind and supportive atmosphere truly makes a difference. Special thanks to Jinhong Park for your help with the Floquet project, Nina del Ser and Alla Bezvershenko for many helpful physics and non-physics discussions, and Imane El Achchi for her work and my fun bringing the cooling project into action on a real quantum computer!

For administrative support and for creating such a lovely atmosphere, I would like to thank Rita Kottmeier, Dina Schäfer, Mariela Boevska, and Andreas Sindermann. The numerical simulations were performed on the CHEOPS cluster at RRZK Cologne.

I really enjoyed working at the institute. Thank you for all the cakes, sharing recipes, playing badminton, swimming, the Women's Coffee Corner, endless walks, and more!

Finally, I want to thank my friends and my family for their endless support – confetti saves lives.

Erklärung

Hiermit versichere ich an Eides statt, dass ich die vorliegende Dissertation selbstständig und ohne die Benutzung anderer als der angegebenen Hilfsmittel und Literatur angefertigt habe. Alle Stellen, die wörtlich oder sinngemäß aus veröffentlichten und nicht veröffentlichten Werken dem Wortlaut oder dem Sinn nach entnommen wurden, sind als solche kenntlich gemacht. Ich versichere an Eides statt, dass diese Dissertation noch keiner anderen Fakultät oder Universität zur Prüfung vorgelegen hat; dass sie - abgesehen von unten angegebenen Teilpublikationen und eingebundenen Artikeln und Manuskripten - noch nicht veröffentlicht worden ist sowie, dass ich eine Veröffentlichung der Dissertation vor Abschluss der Promotion nicht ohne Genehmigung des Promotionsausschusses vornehmen werde. Die Bestimmungen dieser Ordnung sind mir bekannt. Darüber hinaus erkläre ich hiermit, dass ich die Ordnung zur Sicherung guter wissenschaftlicher Praxis und zum Umgang mit wissenschaftlichem Fehlverhalten der Universität zu Köln gelesen und sie bei der Durchführung der Dissertation zugrundeliegenden Arbeiten und der schriftlich verfassten Dissertation beachtet habe und verpflichte mich hiermit, die dort genannten Vorgaben bei allen wissenschaftlichen Tätigkeiten zu beachten und umzusetzen. Ich versichere, dass die eingereichte elektronische Fassung der eingereichten Druckfassung vollständig entspricht.

Teilpublikationen:

(bereits veröffentlicht)

[P131] Matthies, A., Park, J., Berg, E. & Rosch, A. “Stability of Floquet Majorana Box Qubits”. Physical Review Letters 128, 127702 (2022).

(eingereicht)

[P168] Matthies, A., Rudner, M., Rosch, A. & Berg, E. “Programmable adiabatic demagnetization for systems with trivial and topological excitations”. arXiv:2210.17256 (2022).

(in Vorbereitung)

[P171] El Achchi, I., Matthies, A., Rosch, A., Rudner, M. & Berg, E. “Programmable cooling on noisy quantum computers: Implementation and error analysis”. (unpublished)

Signed: ______________________________________

Date: ______________________________________